Computer Modeling of Ceramic Boride Composites

Dr. Valeriy V. Kartuzov

SCIENCE AND TECHNOLOGY CENTER IN UKRAINE
METALISTIV 7A, KYIV, UKRAINE

INSTITUTE FOR PROBLEMS OF MATERIALS SCIENCE
3 KRZHYZHANOVSKY STR., KYIV, 03680 UKRAINE

EOARD #STCU P-510/STCU 11-8003

Report Date: November 2014

Final Report from 1 November 2011 to 31 October 2014

REPORT DOCUMENTATION PAGE

Form Approved OMB No. 0704-0188

1. REPORT DATE *(DD-MM-YYYY)*	2. REPORT TYPE	3. DATES COVERED *(From – To)*
01 November 2014	Final Report	1 November 2011 – 31 October 2014

4. TITLE AND SUBTITLE

Computer Modeling of Ceramic Boride Composites

5a. CONTRACT NUMBER

STCU P-510

5b. GRANT NUMBER

STCU 11-8003

5c. PROGRAM ELEMENT NUMBER

61102F

6. AUTHOR(S)

Dr. Valeriy V. Kartuzov

5d. PROJECT NUMBER

5d. TASK NUMBER

5e. WORK UNIT NUMBER

7. PERFORMING ORGANIZATION NAME(S) AND ADDRESS(ES)
SCIENCE AND TECHNOLOGY CENTER IN UKRAINE
METALISTIV 7A, KYIV, UKRAINE

INSTITUTE FOR PROBLEMS OF MATERIALS SCIENCE
3 KRZHYZHANOVSKY STR., KYIV, 03680 UKRAINE

8. PERFORMING ORGANIZATION REPORT NUMBER

N/A

9. SPONSORING/MONITORING AGENCY NAME(S) AND ADDRESS(ES)

EOARD
Unit 4515
APO AE 09421-4515

10. SPONSOR/MONITOR'S ACRONYM(S)

AFRL/AFOSR/IOE (EOARD)

11. SPONSOR/MONITOR'S REPORT NUMBER(S)

AFRL-AFOSR-UK-TR-2015-0016

12. DISTRIBUTION/AVAILABILITY STATEMENT

Distribution A: Approved for public release; distribution is unlimited.

13. SUPPLEMENTARY NOTES

14. ABSTRACT
This effort was to investigate regularities and mechanisms of kinetics growth of boride-boride composites of eutectic co-crystallization by means of computer modeling. In terms of project's scope of work a lot of new important results were obtained. Calculations showed that coefficients of thermal expansion (CTE) for LaB_6 and systems $LaB_6 - MeB_2$ (Me – Zr, Ti) have an jump in temperature interval from 750 K to 1000 K. At elevation of temperature the energy of contact surface in these systems decreases however the system preserves its mechanical properties up to melting temperatures. Ideal work of adhesion of the interface $[001]$-LaB_6//$[001]$-$Ti_xZr_{1-x}B_2$, (110)-LaB_6//(110)-$Ti_xZr_{1-x}B_2$ increases if titanium concentration elevates. Change of a direction of fibers growth at directed solidification of eutectics LaB_6–$Ti_xZr_{1-x}B_2$ is associated with a big loss in energy at formation of semi-coherent interface as titanium concentration increases. A conception of internal energy sources allocated on interfaces and in phase volume of composites and is the bond energy among composite's components in a solid state: surface energy of interfaces, spot defects, internal stresses governed by components CTE, etc. is proposed. A new model of interface evolution at heating where a surface boundary between phases turns into a boundary with a thickness (i.e. volumetric) and consists of two solid parts with a liquid between is presented. Computer software to obtain multi-fractal characteristics of 2D images obtained in electron microscope is developed. A package of computer programs for 2D imitative modeling of formation of eutectic structures is developed on the base of cellular automates. Moreover the analytical review of both a retrospective and current Russian and Ukrainian papers in the field of new materials for aviation is carried out. The results obtained under this project are published in 21 papers, one monograph is also submitted to print; 17 papers are presented at conferences.

15. SUBJECT TERMS

EOARD, Materials, mictrostructural characterization, high temperature

16. SECURITY CLASSIFICATION OF:			17. LIMITATION OF ABSTRACT	18, NUMBER OF PAGES	19a. NAME OF RESPONSIBLE PERSON
a. REPORT	**b. ABSTRACT**	**c. THIS PAGE**			Matthew Snyder
UNCLAS	UNCLAS	UNCLAS	SAR	187	**19b. TELEPHONE NUMBER** *(Include area code)* +44 (0)1895 616420

Standard Form 298 (Rev. 8/98)
Prescribed by ANSI Std. Z39-18

Project Title: **COMPUTER MODELING OF CERAMIC BORIDE COMPOSITES**

Final Report

Reporting Period: 01/11/2011 - 01/11/2014

Principal Investigator: Kartuzov Valeriy Vasilievich (PhD)

Institution: Frantsevich Institute
for Problems of Materials Science
of National Academy
of Sciences, Ukraine

EOARD Project Number: 118003

STCU Project Number: P510

ABSTRACT

This effort was to investigate regularities and mechanisms of kinetics growth of boride-boride composites of eutectic co-crystallization by means of computer modeling. In terms of project's scope of work a lot of new important results were obtained. Calculations showed that coefficients of thermal expansion (CTE) for LaB_6 and systems $LaB_6 - MeB_2$ (Me – Zr, Ti) have an jump in temperature interval from 750 K to 1000 K. At elevation of temperature the energy of contact surface in these systems decreases however the system preserves its mechanical properties up to melting temperatures. Ideal work of adhesion of the interface [001]-LaB_6//[001]-$Ti_xZr_{1-x}B_2$, (110)-LaB_6//(110)-$Ti_xZr_{1-x}B_2$ increases if titanium concentration elevates. Change of a direction of fibers growth at directed solidification of eutectics LaB_6–$Ti_xZr_{1-x}B_2$ is associated with a big loss in energy at formation of semi-coherent interface as titanium concentration increases. A conception of internal energy sources allocated on interfaces and in phase volume of composites and is the bond energy among composite's components in a solid state: surface energy of interfaces, spot defects, internal stresses governed by components CTE, etc. is proposed. A new model of interface evolution at heating where a surface boundary between phases turns into a boundary with a thickness (i.e. volumetric) and consists of two solid parts with a liquid between is presented. Computer software to obtain multi-fractal characteristics of 2D images obtained in electron microscope is developed. A package of computer programs for 2D imitative modeling of formation of eutectic structures is developed on the base of cellular automates. Moreover the analytical review of both a retrospective and current Russian and Ukrainian papers in the field of new materials for aviation is carried out. The results obtained under this project are published in 21 papers, one monograph is also submitted to print; 17 papers are presented at conferences.

INTRODUCTION

This effort was to investigate regularities and mechanisms of kinetics growth of boride-boride composites of eutectic co-crystallization by means of computer modeling. The approach used is based on development of mathematical models which reliably describe this process through the whole material structure scales (macro, meso and micro) and conduction of numerical experiment targeted on optimization of structure and service properties of the above said composites. In terms of project's scope of work in a triad "Model (B) - Computer program (C) - Result of numerical experiment (A)" many new significant results were obtained. The most striking and interesting are the following:

A. (Results)

➢ Calculations on the base of the method of apriori pseudopotential showed that coefficients of thermal expansion (CTE) for LaB_6 and systems $LaB_6 - MeB_2$ (Me – Zr, Ti) have an jump in temperature interval from 750 *K* to 1000 *K*. At elevation of temperature the energy of contact surface in these systems decreases, however the system preserves its mechanical properties up to melting temperatures (eutectic temperatures). The presence of local maximum of strength is shown for the composite in the eutectic point.

➢ Ideal work of adhesion of the interface $[001]$-LaB_6//$[001]$-$Ti_xZr_{1-x}B_2$, (110)-LaB_6//(110)-$Ti_xZr_{1-x}B_2$ increases if titanium concentration elevates. Change of a direction of fibers growth at directed solidification of eutectics LaB_6–$Ti_xZr_{1-x}B_2$ is associated with a big loss in energy at formation of semi-coherent interface as titanium concentration increases.

➢ Modeling of interface phenomena in Cu-Si predicts the existence of a new type of equilibrium states (solid phase-liquid-solid phase) at temperature above the eutectic one; these states describe a complete disintegration with a liquid interface. This shows the role of interface energy as possible mechanism for contact melting

phenomena and formation of diffusion zone. The obtained results also explain a phenomenon of separation phases in liquid eutectic.

B. (Models)

➢ A conception of internal energy sources allocated on interfaces and in phase volume of composites, which reflect the energy of binding between composite's components in a solid state: surface energy of interfaces, point defects, internal stresses due to difference of CTE of components, etc. is proposed. Density of internal energy sources (it depends on composite structure in a solid state) may cause self-heating of composite and fall of energy required for melting of the whole composite, i.e. reduction of total melting temperature of composite as it occurs in eutectic composites. This temperature fall can be significant and it depends on a ratio between concentrations of composite components as well as structure of interphase boundaries.

➢ A new model is presented of interface evolution at heating where a surface boundary between phases turns into a boundary with a thickness (i.e. volumetric) and consists of two solid parts with a liquid between. The model is developed in assumption that diffusion does not influence temperature distribution, which is defined by a solution of separate problem, but temperature affects diffusion through the dependence of diffusion coefficient on temperature.

C. (Programs)

➢ Computer software to obtain multi-fractal characteristics of 2D images obtained in electron microscope is developed.

➢ A package of computer programs for 2D imitative modeling of formation of eutectic structures is developed on the base of cellular automates method.

Moreover the analytical review of both a retrospective and current Russian and Ukrainian papers in the field of new materials for aviation is carried out.

The results obtained under this project are published in 21 papers, one monograph is also submitted to print; 17 papers are presented at international conferences; two scientists involved (S. Ivanov and A.Khachatrian) defended their PhD; students partially involved in this project defended 4 Master's diploma works.

I. MACROSCALE

1. Continuum model of formation of eutectic compositions by directional solidification method (macro level).

A continuum model is proposed of eutectic ceramic composites formed from two-component melt during its crystallization (fig.1) under conditions of controlled heat removal, characterized by the temperature gradient and the velocity of the crystallization front [1 - 9].
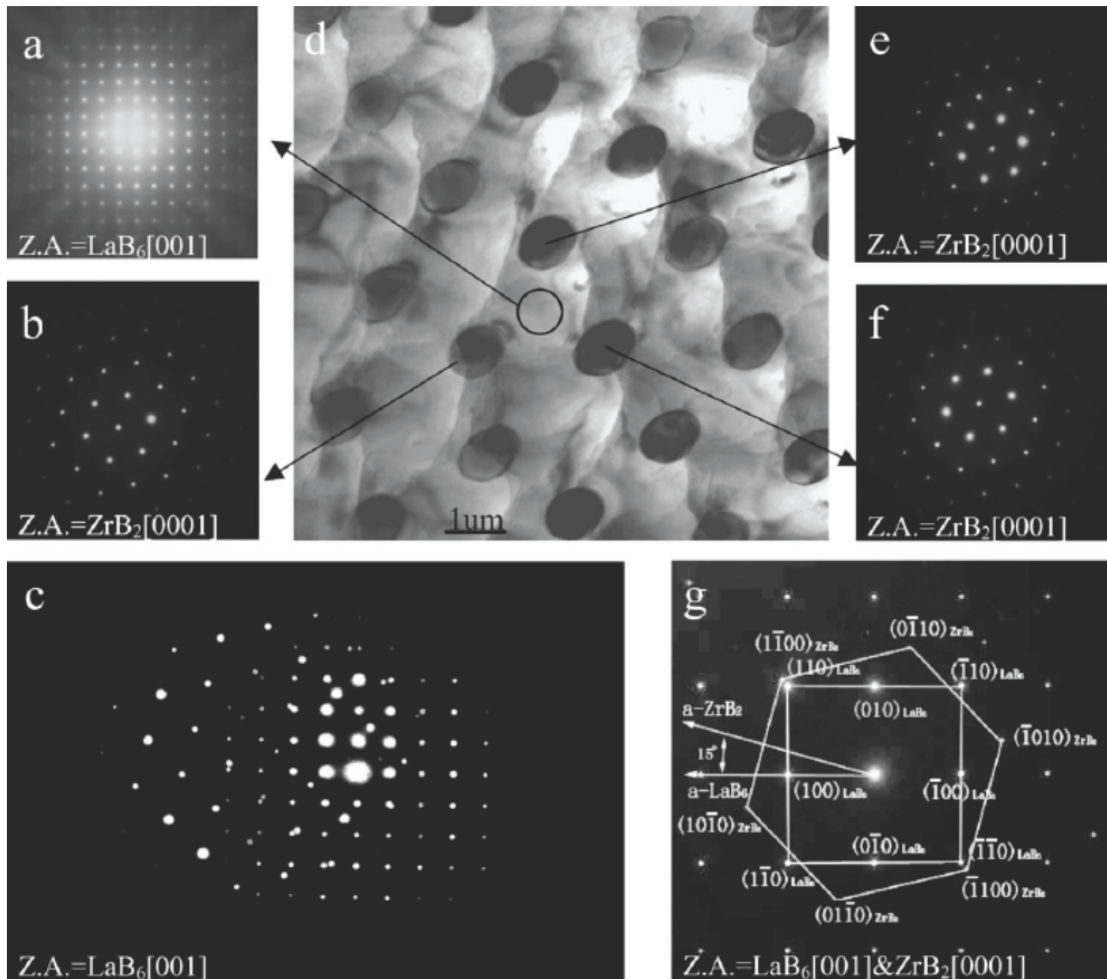
Fig. 1. TEM data from the transverse section of a LaB_6-ZrB_2 DSE (g) is the SAD pattern, which illustrates that [0001] ZrB_2 is approximately parallel to [0001] LaB_6 and (110) LaB_6 parallels ($\bar{1}100$) ZrB_2. Kikuchi lines evident in (c) show that there is actually a small misorientation between two phases. Electron diffraction patterns from individual fibers (b, e, f) indicate that all of the ZrB_2 fibres are locally oriented in the same direction within 0.02 degrees.

Figure 2 provides examples of investigated schemes of regular two-component eutectic composites, where *A*, *B* — mutually insoluble in solid state components of the composite; *A* — matrix (e.g., LaB$_6$), *B* — fibers with diameter *d* or plates with thickness *d* (eg, TiB2, ZrB2, HfB2, ...). It is assumed that composite component B has eutectic concentration *c*, see Figure 2.
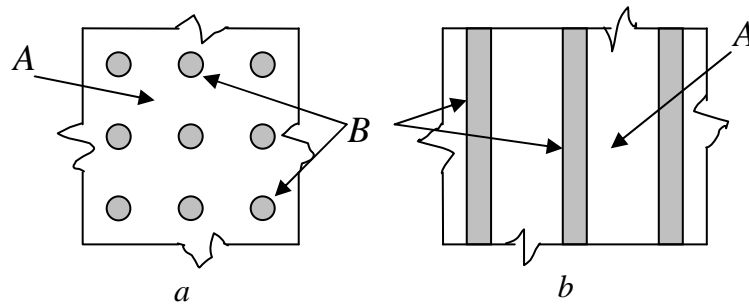

Fig. 2. Scheme of eutectic compositions with regular structure: (*a*) – fibrous; (*b*) – lamellar.

Formulation of the initial-boundary problem of directional solidification with explicit isolation of the interphase interface.

Fig. 3 presents a diagram of temperature distribution *T(x,t)* in the melt $(0 \leq x \leq S(t))$ and regular composite (in solid phase, $S(t) \leq x \leq L$) under non-stationary mode of its formation. Accepted notation: *v = const* — velocity of pulling of the composite in direction of *x* axis, *t* — time, T_c — temperature of crystallization and structure formation of the composite.

It is assumed that the insulation of the lateral surface is provided as a part of equipment design and lateral (in the direction perpendicular to the axis *x*) heat removal is absent. Its presence is undesirable because it facilitates formation of heterogeneity of composite in the transverse direction (along the front of crystallization). Therefore, heat flow takes place in the direction of the axis *x*, and depends on the temperature distribution along this axis (see Fig. 3)

The problem of modeling the composite formation is formulated as the following modified Stefan problem:

Find temperature distribution $T(x,t)$:

$$T = T(x,t) \equiv \begin{cases} T_1(x,t), & 0 \le x \le S(t) \\ T_2(x,t), & S(t) < x \le L \end{cases}, \quad t \ge 0 \tag{1}$$

and law of motion of front of crystallization and structure formation $S(t)$.
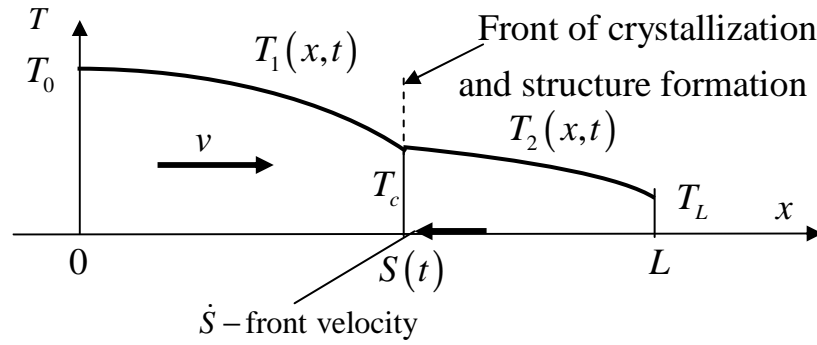
Fig. 3. Scheme of temperature distribution $T(x,t)$, $T_L < T_c$, $t \ge 0$.

Fig. 4 provides scheme of phase diagram of the eutectic composite.
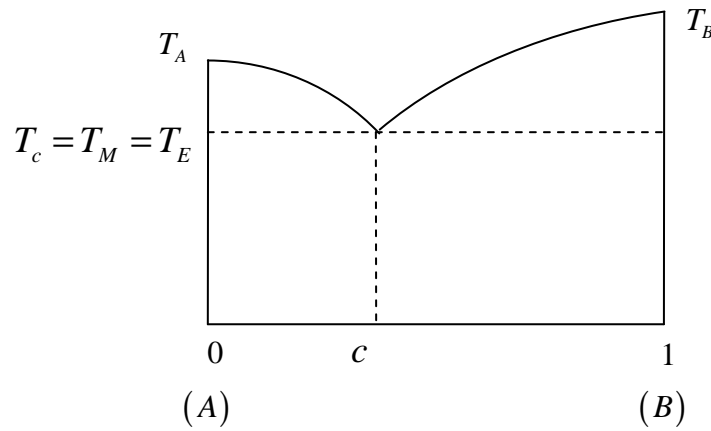
Fig. 4. Schematic phase diagram of the composite. T_M — melting temperature; T_c — temperature of crystallization (solidification); T_E, c — eutectic temperature and concentration respectively.

It is assumed that the densities of the liquid and solid phases coincide: $\rho_l = \rho_s = \rho$. From this and from the continuity of flow ($\rho_l v_l = \rho_s v_s$) follows that $v_l = v_s = v$. In addition, it is assumed that the insulation of side surface of the sample is provided by the process equipment design and lateral (in the direction

perpendicular to the axis x) heat flux is absent. Its presence is undesirable because it creates non-uniformity in composite in the transverse direction (along the front of crystallization). Because of this heat flow takes place in the direction of the axis x and depends on the temperature distribution (1) along this axis (see. Fig. 3), which is determined by the equations:

$$\rho c_l \frac{\partial T_1}{\partial t} = \lambda_l \frac{\partial^2 T_1}{\partial x^2} - \rho c_l v \frac{\partial T_1}{\partial x}, \quad 0 \leq x \leq S(t)$$

$$\rho c_s \frac{\partial T_2}{\partial t} = \lambda_s \frac{\partial^2 T_2}{\partial x^2} - \rho c_s v \frac{\partial T_2}{\partial x} \quad S(t) \leq x \leq L$$
(2)

Equations (2) are complemented by the boundary conditions:

A) At the ends of interval $(0,L)$ constant temperature is maintained:

$$T_1(0;t) = T_0 > T_c, \quad T_2(L;t) = T_L < T_c, \quad t \geq 0.$$
(3)

B) Conditions at the front of crystallization and structure formation $S(t)$:

$$T_1(S(t),t) = T_2(S(t),t) = T_c, \quad t \geq 0,$$
(4)

$$\lambda_l \frac{\partial T_1}{\partial x}\bigg|_{x=S-0} - \lambda_s \frac{\partial T_2}{\partial x}\bigg|_{x=S+0} + (c_S - c_l)\rho v T_c = \sigma \dot{S}(t), \quad \dot{S}(t) < 0,$$
(5)

$$\sigma = \sigma_b + \sigma_c,$$
(6)

where σ - specific (per unit volume) energy of crystallization of composite components and formation of its structure (bonds (contacts) between its components). Specific energy σ has two components: σ_c — effective latent heat of crystallization (melting) of composite per unit of its volume; σ_b — specific energy required for the formation (breakup) of bonds between the components of the composite.

Latent heat of crystallization per unit volume of the composite is estimated by the formula

$$\sigma_c = \rho q_c, \tag{7}$$

where $q_c = (1-c)q_A + cq_B$ — is the same but per unit mass; q_A i q_B — latent heat of crystallization (melting) of unit mass of corresponding components A and B of composite.

For energies of formation (break up) of boundaries of composites (a) and (b), see Figure 1, related to unit volume of the composite we have, respectively, estimates

$$\sigma_{b1} = \frac{4\gamma c}{d}, \ \sigma_{b1} = \frac{2\gamma c}{d}, \tag{8}$$

wher γ — surface energy of the interface between component A and B. Composites (a) and (b), respectively, contain in a unit volume $N = \dfrac{4c}{\pi d^2}$ of parallel fibers with diameter d and $N = \dfrac{c}{d}$ lamellae of thickness d with concentration c.

From relations of linear thermoelasticity we obtain the following assessment of internal stress energy per unit volume of eutectic due to the difference of the coefficients of thermal expansion of the composite components

$$\sigma_{b2} = \frac{(1-c)cE_A E_B E_e}{2\beta^2}(\alpha_A - \alpha_B)^2 \Delta T^2, \tag{9}$$

where $E_e = (1-c)E_A + cE_B$; $\beta = E_e + \left[(1-c)\alpha_B E_A + c\alpha_A E_B\right]\Delta T$; E_A, E_B — moduli of elasticity of composite solid components; α_A, α_B — coefficients of linear thermal expansion of composite components; ΔT — temperature difference that led to the emergence of internal stress in the composite.

Thus, in (6) for component σ_b, which takes into account bond formation between components A and B, we have

$$\sigma_b = \sigma_{b1} + \sigma_{b2}. \tag{10}$$

Conditions (5), (6) differ from conditions at the crystallization front of classic Stefan problem because they take into account not only crystallization but also structure formation of composite, component σ_b, see (10). This component differs by surface energy of boundaries between composite components per unit volume of solid phase σ_{b1} and by energy of internal stresses σ_{b2}.

Crystallization temperature or eutectic temperature at the front of crystallization (see Fig. 4) is given by

$$T_c = \frac{q_B \rho_B c + q_A \rho_A (1-c) - \sigma_b}{c_B \rho_B c + c_A \rho_A (1-c)},$$
(11)

where c_A, c_B — specific (per unit mass) heat capacity of the composite components. Note that this temperature depends on the structure of eutectic and contact interaction between its components.

Equations (2) are complemented also by initial conditions

$$T_1(x,0) = T_1(x) = T_0, \ 0 \le x < L; \ \ T_2(L,0) = T_L$$
$$T_1(S_0) = T_2(S_0) = T_c, \ \ \ \ S(t=0) = S_0 = L - \mu$$,
(12)

where μ — sufficiently small number, because at the initial time moment $\dot{S}(0) = -\infty$, see. Fig. 5.

Technologically important is steady mode of pulling the sample when the sample is moved with a constant velocity v. The conditions of front stay in the selected coordinate system and passing to the stationary thermal operation mode ($\frac{\partial T}{\partial t} = 0$) are as follows:

$$\lim_{t \to t_v} S(t) = S^* = S^*(v,d) = const < L \ \ \ \text{(stationary state of the front)},$$
(13)

$$\lim_{t \to t_v} \dot{S}(t) = -v \ \ \ \text{(condition of the front stay)},$$
(14)

$$\left.\frac{\partial T_1}{\partial t}\right|_{t=t_v}=0, \quad 0\leq x\leq S^*; \quad \left.\frac{\partial T_2}{\partial t}\right|_{t=t_v}=0, \quad S^*\leq x\leq L \quad \text{(condition of stationarity).} \quad (15)$$

Function $S(t)$ is decreasing (left-hand part of equation (5) — negative), and velocity $\dot{S}(t)<0$ — increasing function. The front stops at time moment $t=t_v$ when $\dot{S}(t=t_\beta)=-v$. Because of this equalities (13), (14) take the form

$$S(t=t_v)=S(v,d,t_v)=S^*(v,d), \quad (16)$$

$$\dot{S}(t=t_v)=\dot{S}(v,d,t_v)=-v. \quad (17)$$

Equation (17) is the equation to determine the time moment $t=t_v$ when the front stops and steady state mode begins.

The values S^*, $L-S^*$ should significantly exceed the thickness of the crystallization front $\Delta \square \dfrac{d}{\sqrt{c_0}}$. Then macro formulation of the problem (when front is considered as a surface) makes sense.

Equalities (16), (17), in essence, are prerequisite for building a dependency $d = d(v)$. This relationship exists if there is an interval $\left[t_*\leq t_v \leq t^*\right]$ of suitable times $t=t_v$, that is $t_v \in \left[t_*,t^*\right]$.

Figure 5 shows a schematic solution of the formulated Stefan problem. The value S^* indicates the position of the front of crystallization and structure formation when it stopped, that is when $\dot{S}(t=t_v)=-v$. The condition of rest of the front in the chosen coordinate system: $\dot{S}(t=t_v)+v=0$. The initial interval of functional dependence $S(t)$ can be approximated by the dependence $S(t)=L-\alpha\sqrt{t}$.

If stationary front position $S(t_v) = S^*$ is known from the solution of the Stefan problem, see (16), then temperature distribution

$$T = T(x) \equiv \begin{cases} T_1(x), & 0 \le x \le S^* \\ T_2(x), & S^* < x \le L \end{cases},$$

corresponding to a stationary regime of crystallization and structure formation of eutectic composition is given in a closed form by formulas:

$$T_1 = T_c + \frac{T_0 - T_c}{1 - \exp\left(\frac{v}{a_l} S^*\right)} \left(\exp\left(\frac{v}{a_l} x\right) - \exp\left(\frac{v}{a_l} S^*\right) \right), \quad a_l = \frac{\lambda_l}{\rho c_l}, \quad 0 \le x \le S^*, \quad (18)$$

$$T_2 = T_L + \frac{T_c - T_L}{1 - \exp\left(\frac{v}{a_s}(L - S^*)\right)} \left(\exp\left(\frac{v}{a_s}(x - S^*)\right) - \exp\left(\frac{v}{a_s}(L - S^*)\right) \right),$$

$$a_s = \frac{\lambda_s}{\rho_s c_s}, \quad S^* < x \le L. \tag{19}$$

For temperature gradients at the front $x = S^*(v,d)$ from (18), (19) we have

$$\left.\frac{\partial T_1}{\partial x}\right|_{x=S^*-0} = \frac{T_0 - T_c}{1 - \exp\left(\frac{v}{a_l} S^*\right)} \frac{v}{a_l} \exp\left(\frac{v}{a_l} S^*\right), \quad \left.\frac{\partial T_2}{\partial x}\right|_{x=S^*+0} = \frac{T_c - T_L}{1 - \exp\left(\frac{v}{a_s}(L - S^*)\right)} \frac{v}{a_s}.$$

From this, for the heat flux W spent on this front for crystallization and structure formation of eutectic composite, we obtain

$$W = \lambda_l \frac{T_0 - T_c}{1 - \exp\left(vS^*/a_l\right) a_l} \frac{v}{a_l} \exp\left(\frac{v}{a_l} S^*\right) - \lambda_S \frac{T_c - T_L}{1 - \exp\left(v(L - S^*)/a_s\right) a_s} \frac{v}{a_s} + (c_S - c_l)\rho v T_c, \quad (20)$$
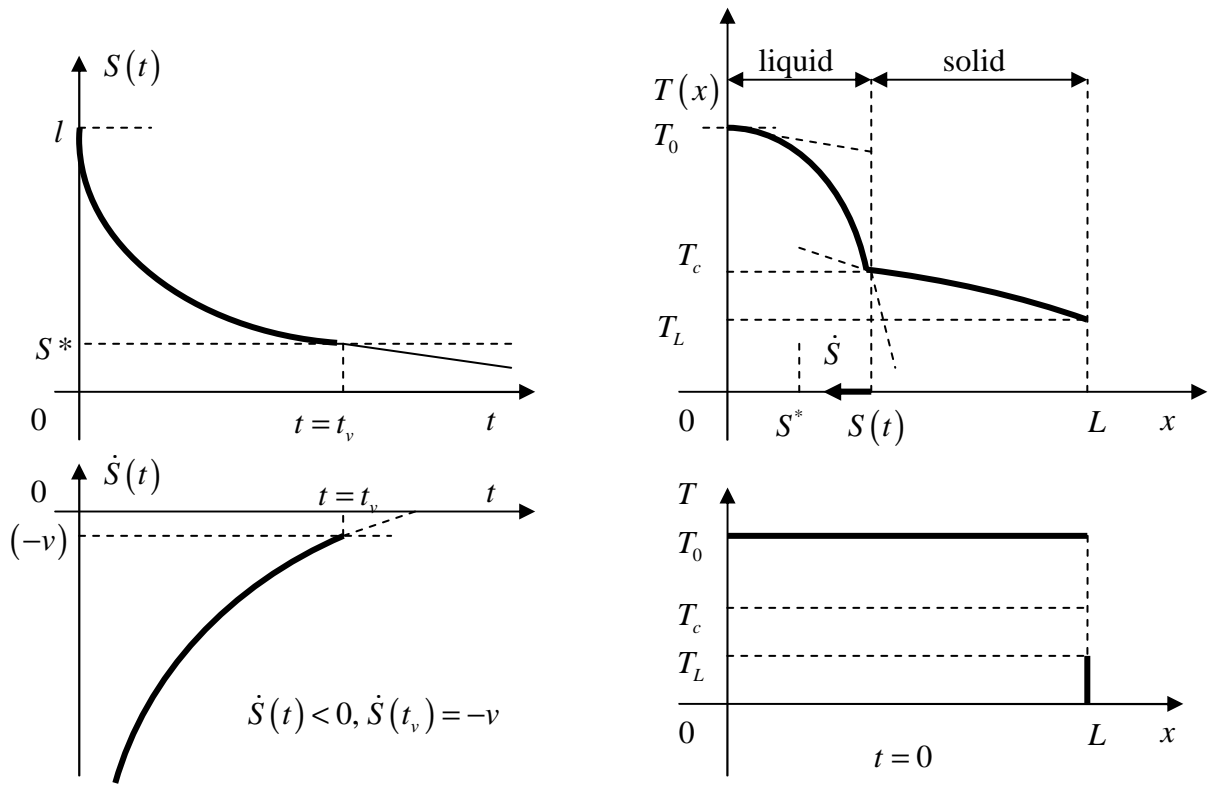
Fig. 5. Schematic solution of modified Stefan problem and initial conditions.

or

$$W = \left[\frac{c_l(T_0 - T_c)}{1 - \exp(vS^*/a_l)} \exp\left(\frac{v}{a_l} S^*\right) - \frac{c_s(T_c - T_L)}{1 - \exp(v(L - S^*)/a_s)} + (c_S - c_l)T_c \right] \rho v. \quad (21)$$

Conditions (5) at the front $x = S^*(v, d)$ take form

$$W = \sigma v = (\sigma_c + \sigma_b) v \quad (22)$$

and determine the implicit functional dependence $d(v)$ of structural parameter d from velocity of directional solidification v. For example, in the case of fiber composite (a), Fig. 2, this dependence is written as

$$\frac{c_l(T_0 - T_c)}{1 - \exp(vS^*/a_l)} \exp\left(\frac{v}{a_l} S^*\right) - \frac{c_s(T_c - T_L)}{1 - \exp(v(L - S^*)/a_s)} + (c_S - c_l)T_c = q + \frac{4\gamma c}{d\rho} + \frac{\sigma_{b2}}{\rho}, \quad (23)$$

where the temperature T_c depends on the fiber diameter d and the size $S^*(v,d)$ of liquid phase depends on the velocity v and the fiber diameter d. For lamellar composite (b), Fig. 2, multiplier factor 2 in the right-hand part of (23) should be replaced with 4.

Calculations

The calculation of parameters of material and processes was carried out for LaB_6-ZrB_2 composite.

Main initial data are given in the Table 1.

Table 1. Properties of materials of the composite.

Material	$E,$ GPa	α (CTE)	$\rho,$ kg/m^3	$T_m,$ °C	$q,$ kJ/ kg	$c_s,$ J/ kg·grad	$c_l,$ J/ kg·grad	$\lambda_s,$ W/ (m·grad)	$\lambda_l,$ W/ (m·grad)
LaB$_6$ [10]	478.73	13.24·10^{-6}	4720.0	2210.0	1798	572	1000*	47.7	20*
ZrB$_2$ [11]	495.81	28.0·10^{-6}	6200.0 (6090)	3225.0	930	429	953	83	58

*) approximate estimate

Thermal properties of LaB_6-ZrB_2 composite as a homogeneous material, such as heat capacity, thermal conductivity and specific crystallization (melting) heat for solid and liquid phases necessary for calculations were found by mixture rule:

$c_s = (1 - c_0)c_{s\text{LaB6}} + c_0 \cdot c_{s\text{ZrB2}};$

$c_l = (1 - c_0)c_{l\text{LaB6}} + c_0 \cdot c_{l\text{ZrB2}};$

$\lambda_s = (1 - c_0)\lambda_{s\text{LaB6}} + c_0 \cdot \lambda_{s\text{ZrB2}};$

$\lambda_l = (1 - c_0)\lambda_{l\text{LaB6}} + c_0 \cdot \lambda_{l\text{ZrB2}};$

$q = (1 - c_0)q_{\text{LaB6}} + c_0 \cdot q_{\text{ZrB2}}.$

Table 2. Calculated properties of LaB_6+ZrB_2 composite

Material	q, kJ/ kg	c_s, J/ kg·grad	c_l, J/ kg·grad	λ_s, W/ (m·grad)	λ_l, W/ (m·grad)
LaB_6+ZrB_2	1616	542	990	53	26

Other initial parameters for calculations:

$c_0 = 0.16$ (vol.), 0.21 (mass); $\gamma = 170.0$ J/m^2; $T_{00} = 20$ °C; $T_\gamma = 0.9\,T_M$ (approximate estimate); $L = 5$ mm; $T_0 = T_M + 100$ °C; $T_L = T_M - 200$ °C; $v = 4.2 \cdot 10^{-5} - 1.3 \cdot 10^{-4}$ m/s.

Fiber diameter

$$d = \frac{4\gamma c_0}{W - \rho q - w};$$

$$W = -\frac{c_s\rho(T_C - T_L)}{1 - \exp(v(L-\delta)/a_s)} + \frac{c_l\rho(T_0 - T_C)}{1 - \exp(v\delta/a_l)}\exp(v\delta/a_l) + (c_s - c_l)\rho T_C,$$

де $a_l = \dfrac{\lambda_l}{\rho c_l}$, $a_s = \dfrac{\lambda_s}{\rho c_s}$.

Table 3. Calculations of fiber diameter by the formula (23) ($T_m = 2210$ °C).

v, m/s	δ, mm	w, J/m^3	d, μm	
$1 \cdot 10^{-5}$	1.25 (L= 5 mm)	$2.54 \cdot 10^7$	$1.1 \cdot 10^{-3}$	
$2 \cdot 10^{-5}$	2.5	$2.54 \cdot 10^7$	$6.7 \cdot 10^{-4}$	
$5 \cdot 10^{-5}$	1.25	$2.54 \cdot 10^7$	$1.28 \cdot 10^{-2}$	
$1 \cdot 10^{-4}$	1.25	$2.54 \cdot 10^7$	$-4.7 \cdot 10^{-2}$	
$1 \cdot 10^{-4}$	3.75	$2.54 \cdot 10^7$	$1.6 \cdot 10^{-3}$	
$5 \cdot 10^{-5}$	3.75	$2.54 \cdot 10^7$	$7.1 \cdot 10^{-4}$	
$5 \cdot 10^{-5}$	2.5	$2.54 \cdot 10^7$	$1.9 \cdot 10^{-3}$	
$3 \cdot 10^{-5}$	2.5	$2.54 \cdot 10^7$	$1.05 \cdot 10^{-3}$	
$3 \cdot 10^{-5}$	5 (L= 10 mm)	$2.54 \cdot 10^7$	$2.4 \cdot 10^{-3}$	
$3 \cdot 10^{-5}$	10 (L= 20 mm)	$2.54 \cdot 10^7$	$6.8 \cdot 10^{-3}$	
$3 \cdot 10^{-5}$	20 (L= 40 mm)	$2.54 \cdot 10^7$	$8.7 \cdot 10^{-2}$	

During calculations of temperature field in the stationary Stefan problem for every fiber diameter the corresponding melting temperature was calculated, and the temperatures at boundaries of liquid and solid phases were found by adding or by subtracting of some overheating and overcooling temperature, for example, 100 and 200 °C.

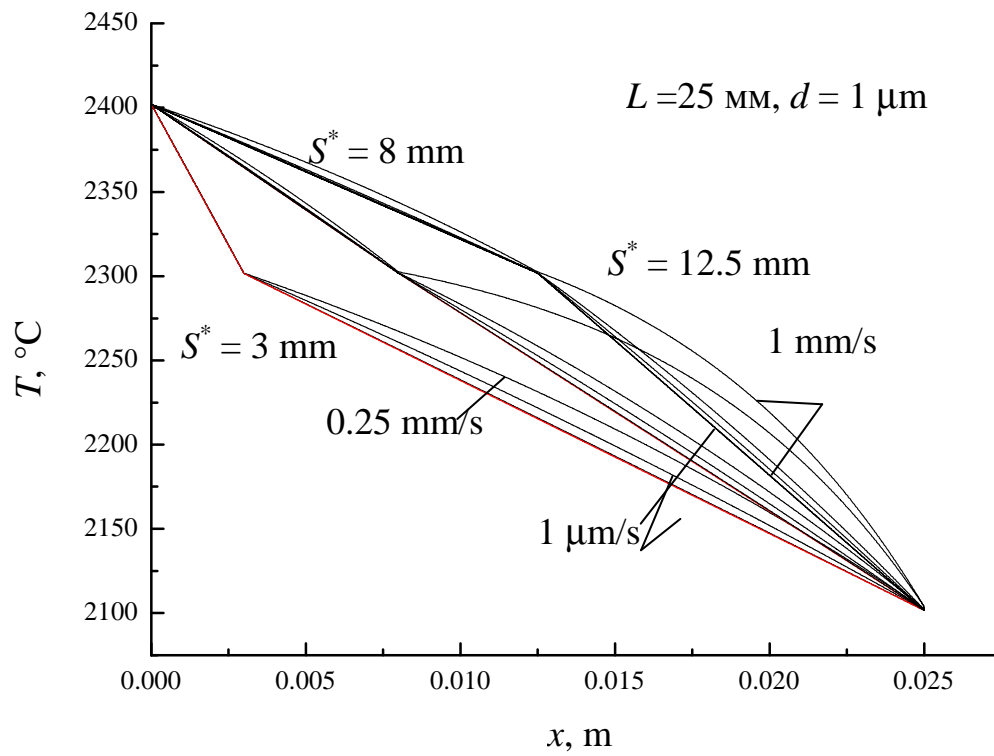Fig. 6. Temperature distribution at $d = 1$ μm, $L = 25$ mm. Pulling velicities 1 μm/s, 0.01 mm/s, 0.1 mm/s, 0,25 mm/s, 1 mm/s.

Fig. 7. Temperature distribution at $d = 1$ μm, $L = 10$ mm. Pulling velicities 1 μm /s, 0.01 mm/s, 0.1 mm/s, 0.25 mm/s, 1 mm/s.

Fig. 8. Temperature distribution at $d = 0.5$ μm, $L = 10$ mm. Pulling velocities 1 μm/s, 0.01 mm/s, 0.1 mm/s, 0.25 mm/s, 1 mm/s.
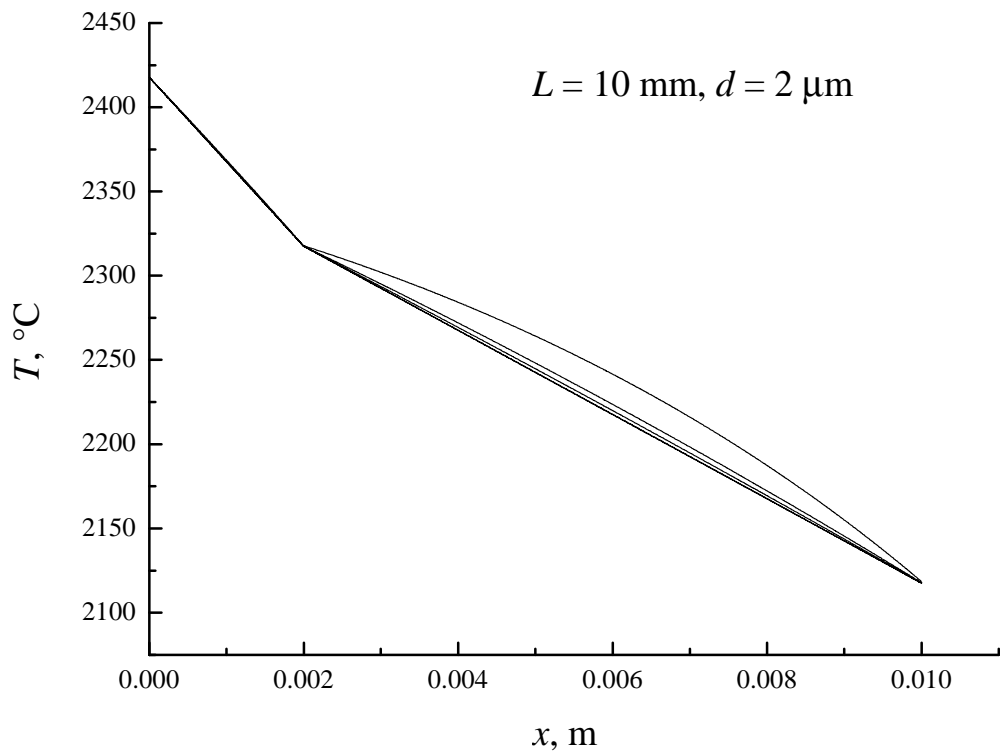
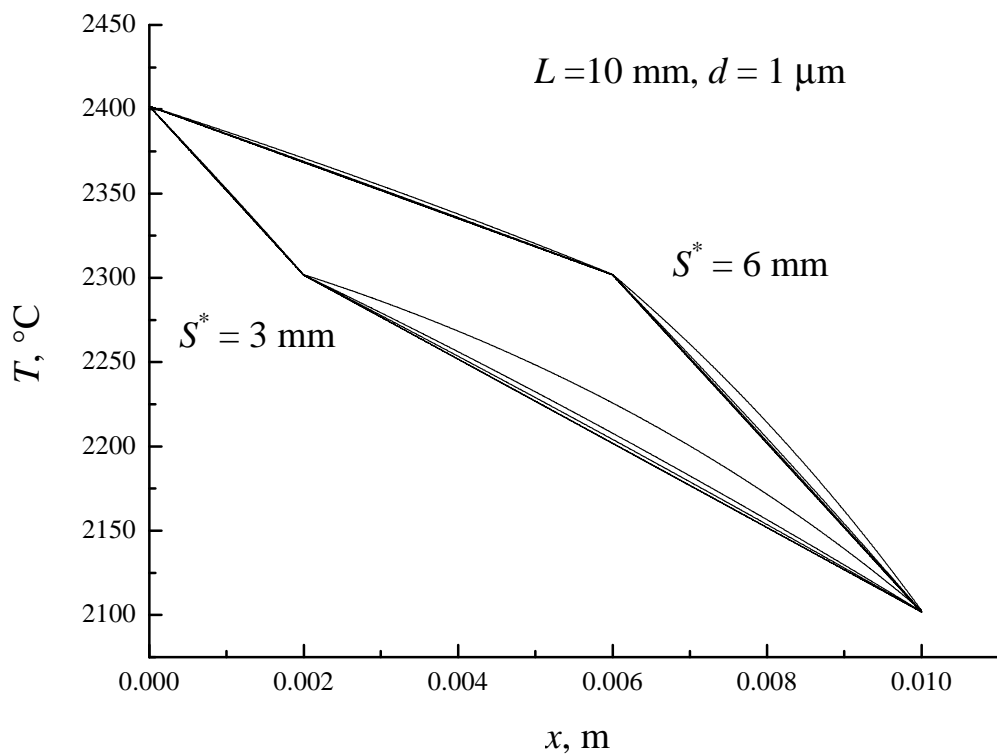Fig. 9. Temperature distribution at $d = 2$ μm, $L = 10$ mm. Pulling velosities 1 μm/s, 0.01 mm/s, 0.1 mm/s, 0.25 mm/s, 1 mm/s.

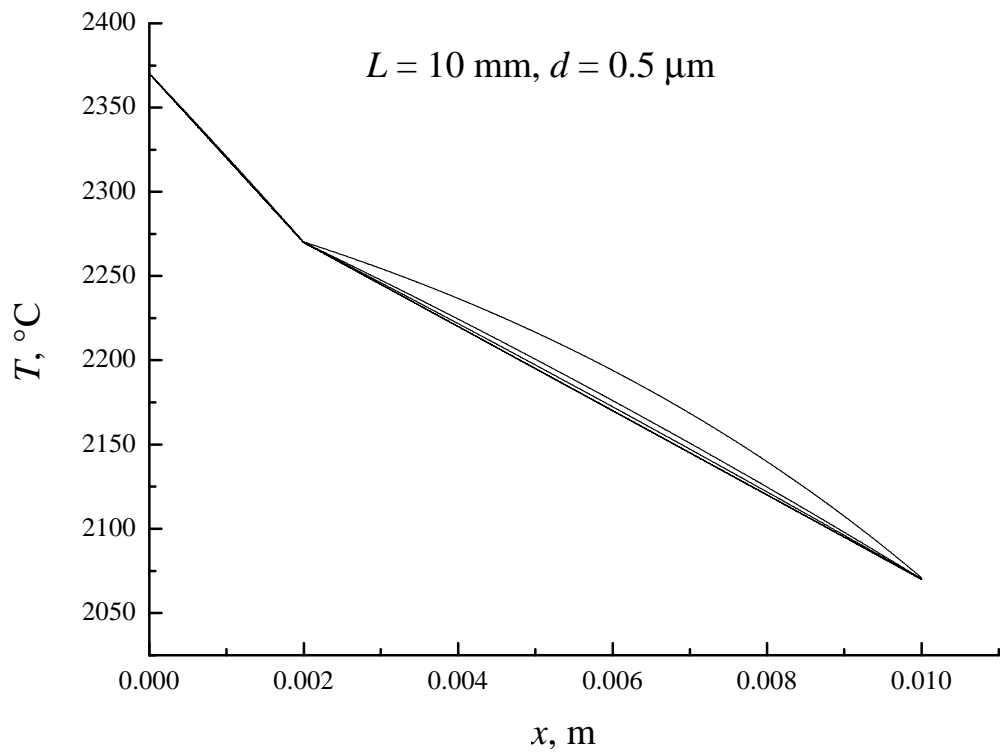## 2. Determination of the melting point of the composite with a model.

This section provides the basic principles of the model of melting point of eutectic solid phase. The basic principle of the model for determining the melting point of eutectic T_m is the concept of internal energy sources: during heating energy of binding between the components of the composite is released (removed), as well as the internal energy of thermal stresses. It is spent for internal heating of the composite (i.e. its self-heating) that causes lowering of the melting point of the composite (compared to the melting temperatures of individual components).

Determining of the temperature T_m of the solid phase is carried out after the formation of the composite structure (see Fig. 10). Therefore T_m depends on the composition, structure and properties of the composite components and their binding energy. Further, melting temperature will be taken equal to solidification temperature, i. e. $T_C = T_M$. In reality, it is an assumption: the boundary between the phases in the phase diagram (see Fig. 10) has a thickness.
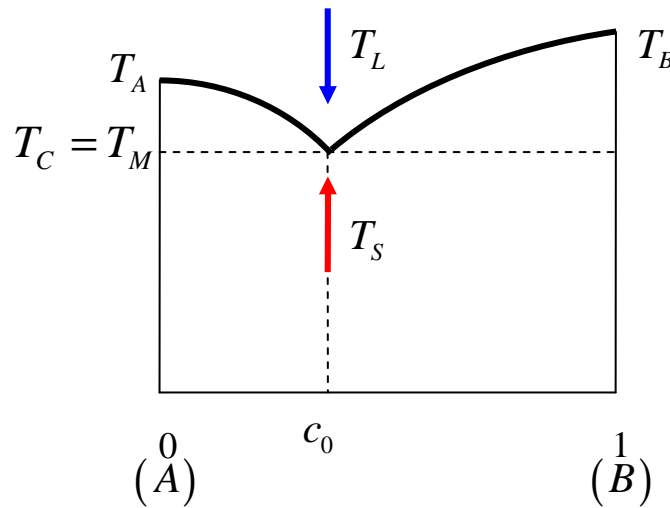
Рис. 10. Schematic phase diagram of two-phase eutectic. T_C - crystallization temperature (solidification), c_0 - eutectic concentration of the phase B, $T_C = T_M$, $T_S \square T_M$, $T_L \square T_C$.

Fig. 11 provides a mechanical interpretation of the concept of internal energy sources.
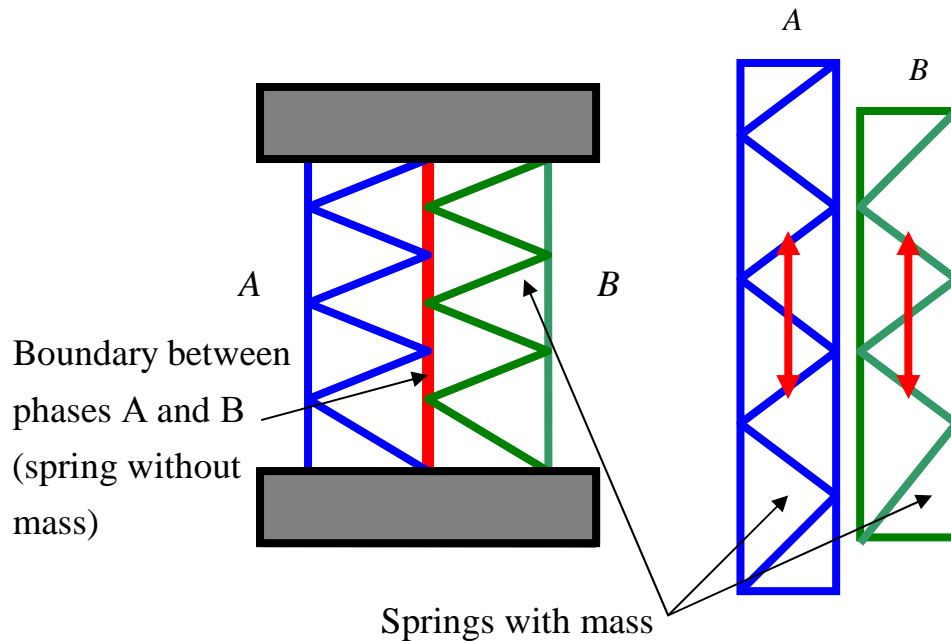
Fig. 11. Mechanical interpretation of the concept of internal energy sources.

The following spatial energy density and internal energy sources are possible: $3D, 2D, D, 0D$ (volume, surface, linear, point), see Fig. 12.
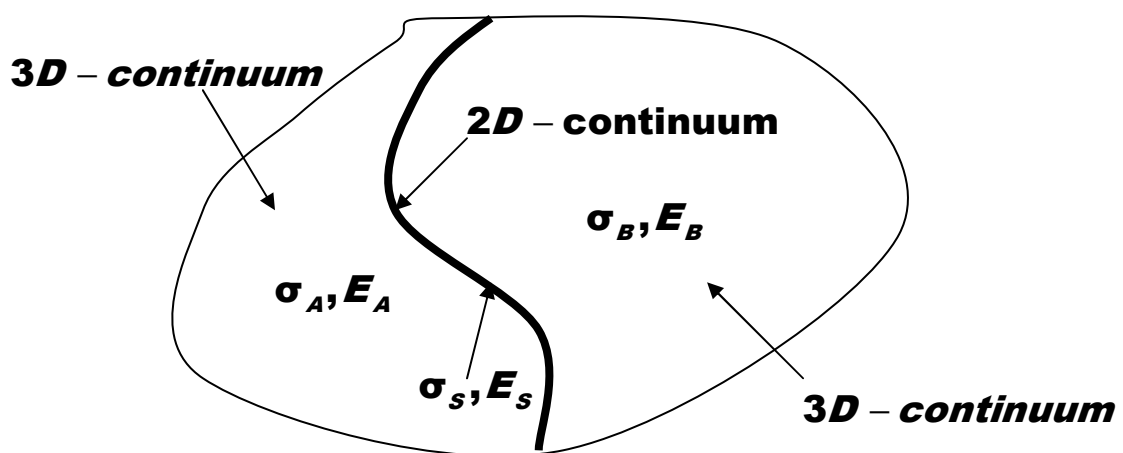
Fig. 12. σ – stress state; E - energy density.

By the time the simplest source is an instantaneous one. It is well known that the instantaneous point source increases the temperature at the point to infinity.

Therefore, in the vicinity of this source there is always a zone of melting, the size of which is determined by its power and changes over time.

If γ - surface energy of flat interface $x=0$ of components A and B, then $P(x,t)=\gamma\delta(x)\delta(t)$ - instantaneous power of the source. Depending on the conditions, the source can be not the whole boundary ($P(x,t)=\gamma\delta(T(x,t)-T_\gamma)\delta(t)$).


$$E=Q$$

$$t_1<t_2<t_3<t_4<.....$$

$$T(x,t)=\frac{Q}{2\sqrt{\pi}ac\rho\sqrt{t}}\exp\left(-\frac{x^2}{4a^2t}\right)$$

$$T(0,0)=\infty$$
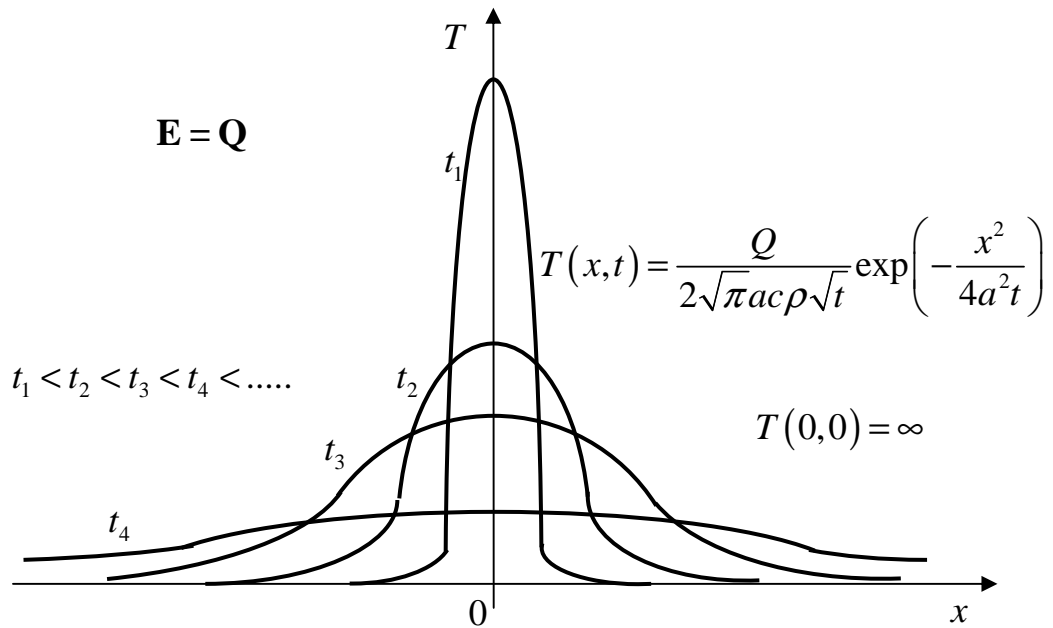
Рис. 13. Schematic temperature distribution $T(x,t)$ from instantaneous point heat source with power $P(x,t)=Q\delta(x)\delta(t)$

In the general case source power depends on the temperature: $P=P(x,t,T)$.

Approximate determination of the melting temperature T_m is made on the example of energy balance in unit volume of a two-phase lamellar eutectic composition:

$$q_B\rho_B c_0 + q_A\rho_A(1-c_0)=\left[c_B\rho_B c_0 + c_A\rho_A(1-c_0)\right](T_M-T_0)+2\gamma N+w, \qquad (24)$$

where $N=\dfrac{c_0}{d}$ - number of plates of phase B with thickness d per unit volume; γ- surface energy of the boundary between the phases A and B (it is assumed that it is abruptly released at temperature $T=T_\gamma<T_M$, see Fig. 14); ρ_A,ρ_B - specific density

of, respectively, phases A and B; c_A, c_B - specific heat capacity of phases A and B; q_A, q_B - specific latent heat of fusion of phases A and B; T_0 - initial temperature of the composite; w - energy per unit volume associated with different coefficients of thermal expansion α_A, α_B of components:

$$w = \frac{(1-c_0)c_0 E_A E_B E_e}{2\beta^2} \Delta\alpha^2 \Delta T^2, \qquad E_e = (1-c_0)E_A + c_0 E_B,$$

$$\beta = E_e + \left[(1-c_0)\alpha_B E_A + c_0 \alpha_A E_B\right]\Delta T, \quad \Delta T = T_\gamma - T_0, \quad \Delta\alpha = \alpha_A - \alpha_B \tag{25}$$

if approximately assume that it is released at the temperature $T = T_\gamma < T_M$. In (1.25) E_A, E_B - elastic Young moduli of the composite components. Approximate estimate (25) for w is derived from relations of linear thermoelasticity.
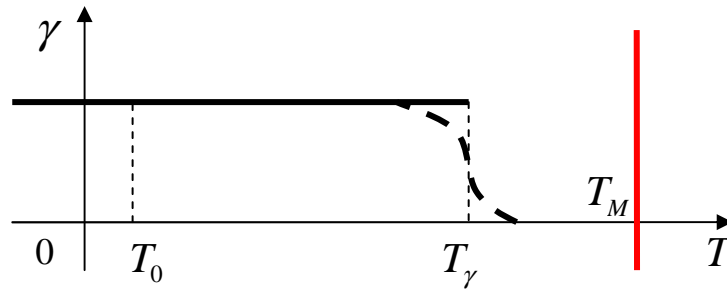
Fig. 14. Schematic dependence of γ from temperature.

From (24) we have a melting temperature of eutectic:

$$T_M = T_C = T_0 + \frac{q_B \rho_B c_0 + q_A \rho_A (1-c_0) - \dfrac{2\gamma c_0}{d} - w}{c_B \rho_B c_0 + c_A \rho_A (1-c_0)}, \tag{26}$$

or (when $\rho_A = \rho_B = \rho$):

$$T_M = T_0 + \frac{q_B c_0 + q_A (1-c_0) - 2\gamma c_0/d - w}{q_B c_0/T_B + q_A (1-c_0)/T_A}, \quad c_A = \frac{q_A}{T_A}, c_B = \frac{q_B}{T_B}, \tag{27}$$

where T_A and T_B - melting temperatures of, respectively, pure components A and B. From formulas (26), (27) it follows that the melting temperature T_m depends on the composition, structure and properties of composite components and their

binding energy. A comparison of formula (27) with the formula of Bystrenko A.V. for the temperature of crystallization $T_C = T_M$ implies the following interesting relationship

$$\Omega c_0 \left(1 - c_0\right) = 2\gamma c_0 / d + w, \qquad (28)$$

where Ω - energy of component mixing in the melt.

Note. It is easy to see that in determining the temperature T_m the eutecticity of the composition is not used and all the principles of the model can be applied to any composition, not only eutectic (i.e. instead of eutectic concentration c_0 any concentration $c \in [0;1]$ can be considered). Therefore, with the proposed model the eutectic melting temperature can be defined as

$$T_M^{eutectic} = \min_{c \in [0;1]} T_M \left(c\right) \equiv T_M \left(c_0\right),$$

where c_0 - eutectic concentration.

In the last formula functional dependencies of $T\left(\square\right)$ from (26), (27) can be used, or refined definition of melting temperature from the solution of the corresponding initial-boundary problems on the cell, which represent a composite.

The presented concept of internal energy sources is the basis for the formulation of initial-value problem for the temperature distribution in the cell, which represents eutectic composition.

This problem will determine the mechanisms of melting temperature formation and the effect on it of the composite structure (including eutectic phase concentration, which will help link such models with models of phase fields, such, for example, as relation (28)).

The simplest initial-boundary value problem for monomaterial that explains the concept of internal energy sources (in this case, source is in the material B and on its boundary $x = 0$, see Fig. 15) and the nature of formation of melting temperature of eutectic:

$$\left(c(T)+q\delta\left(T-T_M^B\right)\right)\rho\frac{\partial T}{\partial t}=\frac{\partial}{\partial x}\left(\lambda(T)\frac{\partial T}{\partial x}\right)+\gamma\delta(t)\delta(x)+w\delta(t),$$

$$x\in[0;\infty),\, t\geq 0$$

(29)

$$c(T)=\begin{cases}c_S & \text{at } T\leq T_M^B, \\ c_L & \text{at } T>T_M^B\end{cases}, \qquad \lambda(T)=\begin{cases}\lambda_S & \text{at } T\leq T_M^B, \\ \lambda_L & \text{at } T>T_M^B\end{cases}$$

$$\rho=\rho_S=\rho_L.$$

Initial condition for (29): $\quad T(x,0)=T_\gamma,\quad 0\leq x\leq\infty$

Boundary conditions for (29): $\quad \dfrac{\partial T}{\partial x}\bigg|_{x=0,t\geq 0}=0,\quad T(\infty,t)=T_\gamma.$

Notations:

$\rho=\rho_S=\rho_L$ - specific density of material (for simplification assumed that densities of liquid and solid phases are equal);

$c(T)$ - specific heat capacity of material;

$\lambda(T)$ - heat conductivity of material;

q - specific latent heat of melting;

$\gamma\delta(t)\delta(x)$ - density of heat source from binding of material (e. g. with another material) at the boundary $x=0$, $\gamma=const$;

$w\delta(t)$ - density of heat sources from internal thermal stresses in material;

T_γ - temperature when binding at the boundary $x=0$ breaks down and internal thermal stresses disappear (see Fig. 14);

$\delta(\square)$ - delta function;

T_M^B - melting temperature of material B (see Fig. 15).

Figure 15 gives schematic graph of solution $T(t,x)$ of the problem (29) for some time moment $t>0$. It shows that in the neighbourhood of the boundary $x=0$ (i. e. in the neighbourhood of the energy source) melting of the material takes place with gradual decrease of temperature.

Fig. 16 presents schematic graph of temperature distribution in the neighbourhood of interface between phases at some time moment $t > 0$ after binding between phases A and B breaks down at the temperature T_γ. This problem consists from two problems of (29) type.

$$T \Box T_\gamma + \frac{\gamma}{\lambda_L \sqrt{\pi t}} \exp\left(-\frac{x^2}{4a_L^2 t}\right)$$
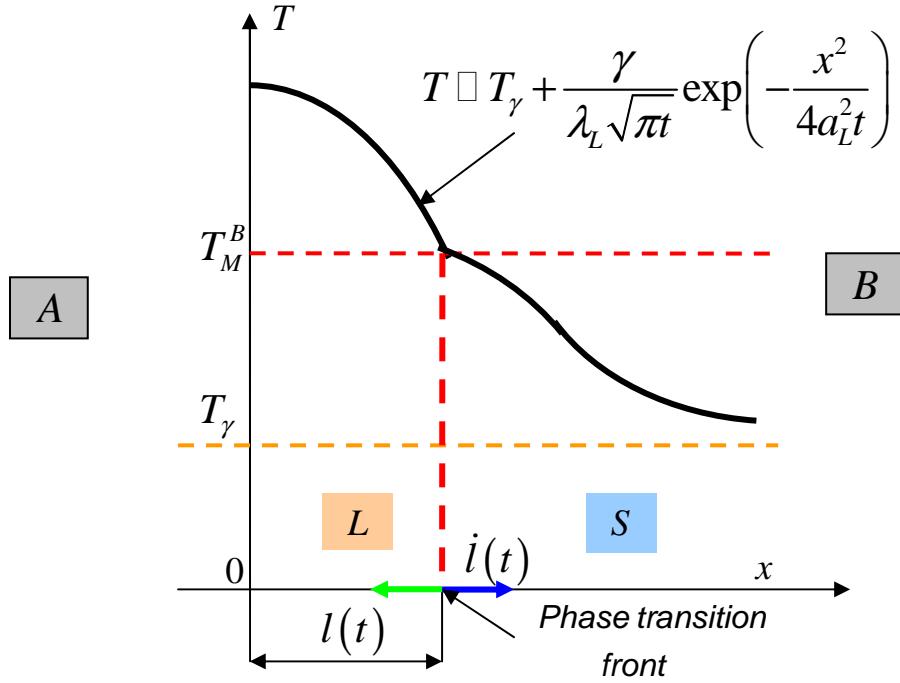
Fig. 15.

Note (to Fig. 16). The source at the interphase boundary has power $Q(x,t) = Q_0 \delta(t) \delta(x)$. Then in the neighbourhood of boundary $x = 0$ we have an approximation:

$$T_A(x,t) \approx \frac{Q_A}{c_A \rho_A \sqrt{\pi a_A^2 t}} \exp\left(-\frac{x^2}{4a_A^2 t}\right), \quad T_B(x,t) \approx \frac{Q_B}{c_B \rho_B \sqrt{\pi a_B^2 t}} \exp\left(-\frac{x^2}{4a_B^2 t}\right),$$

$$a_A^2 = \frac{\lambda_A}{c_A \rho_A}, a_B^2 = \frac{\lambda_B}{c_B \rho_B}, \tag{30}$$

$$Q_0 = Q_A + Q_B \tag{31}$$

Fig. 16. Schematic graph of themperature distribution in the neighbourhood of flat boundary $x=0$ of initial separation of phases A and B, $x_A(0)=x_B(0)=0$;

$$\kappa_A = \frac{\sqrt{c_A \rho_A \lambda_A}}{\sqrt{c_A \rho_A \lambda_A} + \sqrt{c_B \rho_B \lambda_B}}; \quad \kappa_B = \frac{\sqrt{c_B \rho_B \lambda_B}}{\sqrt{c_A \rho_A \lambda_A} + \sqrt{c_B \rho_B \lambda_B}}.$$
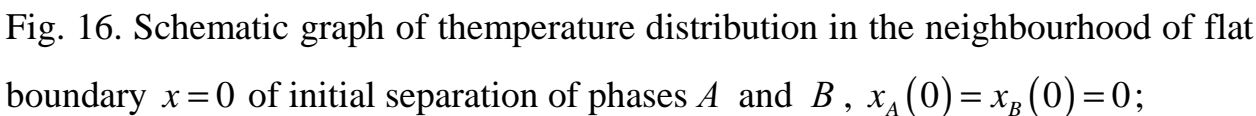
Under condition $T_A(0,t) = T_B(0,t)$, temperature continuity at the boundary $x=0$, we have:

$$\frac{Q_A}{c_A \rho_A \sqrt{\pi a_A^2 t}} = \frac{Q_B}{c_B \rho_B \sqrt{\pi a_B^2 t}}.$$

From this and from (1.31) we obtain:

$$Q_A = \frac{\sqrt{c_A \rho_A \lambda_A}}{\sqrt{c_A \rho_A \lambda_A} + \sqrt{c_B \rho_B \lambda_B}} Q_0 \equiv \kappa_A Q_0; \quad Q_B = \frac{\sqrt{c_B \rho_B \lambda_B}}{\sqrt{c_A \rho_A \lambda_A} + \sqrt{c_B \rho_B \lambda_B}} Q_0 \equiv \kappa_B Q_0.$$

Conclusions

The main outcome ("know-how") of this section is the concept (principle) of internal energy sources, which are located at the boundaries and in the bulk of composite phases and is the energy of binding between the components of the composite in the solid state: surface energy of interphase boundaries, point defects, internal stresses caused by the difference of CTE of the composite components and so on. The density of internal energy sources (it depends on the structure of the composite in solid state) may be such as to cause self-heating of composite and reduce energy required to melt the entire composite when it is heated, i. e. reducing the overall temperature to melt the composite, as is the case in eutectic compositions. This reduction can be significant and it depends on the ratio between concentrations of the composite components.

In the section, we provided first approximate estimates of the effect, and formulated simple initial-boundary value problems that need to have numerical methods for their solution be developed in the near future as well as appropriate software. For a more accurate and thorough investigation of these effects, a formulation on these principles (concept of internal energy sources) of initial-boundary value problems for a representative cell of the composite should be carried out (some of such formulations have been done by the authors of the report). Special attention in this work should be given to such a test setting, for which experimental control will be possible in time for the heating of the sample and temperature distribution in it, and the process of evolution of interphase boundaries during heating (see next section).

Calculations

The estimate of melting temperature of the composite by formula (27):

$$T_M = T_C = T_{00} + \frac{q_B \rho_B c_0 + q_A \rho_A (1-c_0) - \dfrac{2\gamma c_0}{d} - w}{c_B \rho_B c_0 + c_A \rho_A (1-c_0)}$$

where

$$w = \frac{(1-c_0)c_0 E_A E_B E_e}{2\beta^2} \Delta\alpha^2 \Delta T^2, \qquad E_e = (1-c_0)E_A + c_0 E_B,$$

$$\beta = E_e + \left[(1-c_0)\alpha_B E_A + c_0 \alpha_A E_B\right]\Delta T, \quad \Delta T = T_\gamma - T_{00}, \quad \Delta\alpha = \alpha_A - \alpha_B$$

Table 4. Dependence of calculated melting temperature from fiber diameter

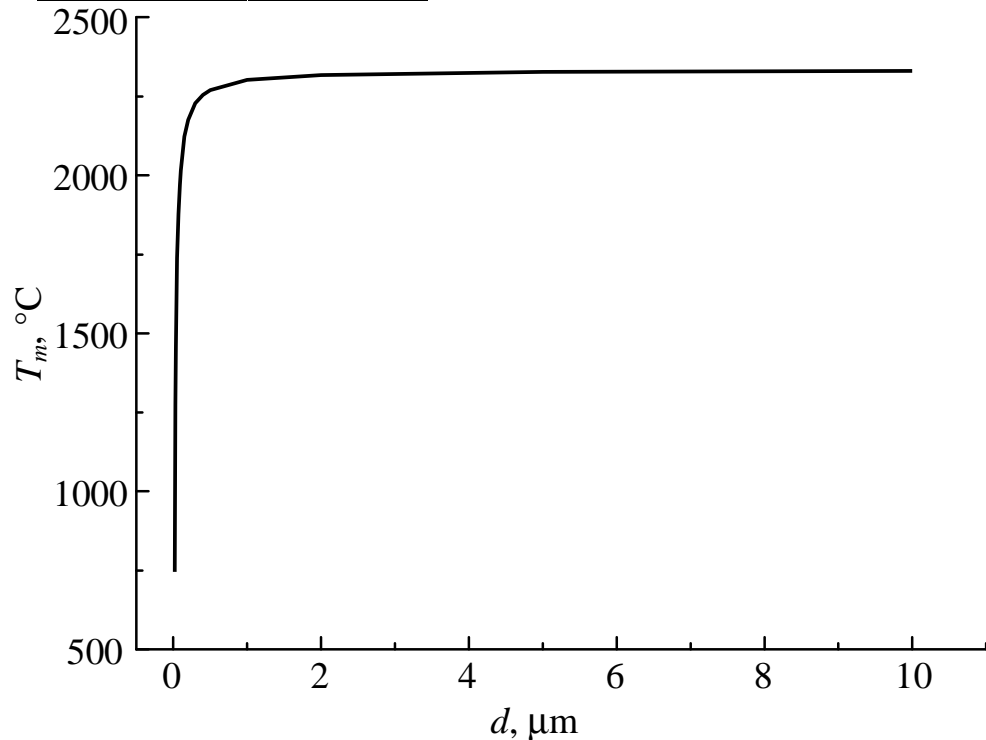| d, μm	T_c, °C	d, μm	T_c, °C
0,015	214	0,2	2175
0,02	745	0,3	2228
0,03	1275	0,4	2254
0,04	1540	0,5	2270
0,05	1699	1	2302
0,06	1805	2	2317
0,08	1937	5	2327
0,1	2016	10	2330
0,15	2122		

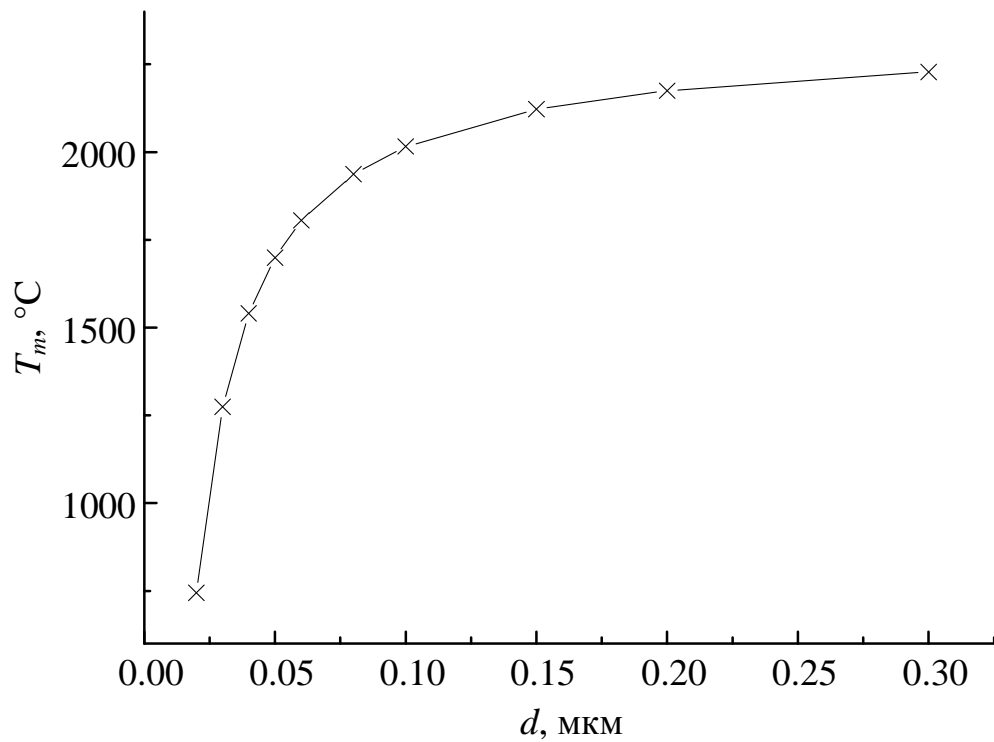Fig. 17. Calculated dependence of melting temperature from fiber diameter for LaB_6-ZrB_2 composite.

Fig. 18. Enlarged fragment of Fig. 17. Dependence of melting temperature from fiber diameter for LaB_6-ZrB_2 composite.

3. Modeling of evolution of interphase boundary during heating.

In [12] the results of an experimental study were analyzed of the evolution of interphase boundaries of simplest binary eutectic compositions in the transition from solid to liquid state when heated to the melting point. The analysis showed that evolution is going from the clear boundaries of the solid phase (i. e. the surface between the phases), to blured boundaries (i. e. to the volume boundaries that have thickness and are formed from a liquid that is a mixture of composite components, see Fig. 19 – 21).

This is an experimental proof of concept of internal energy sources according to which melting begins with the destruction of boundaries between the phases in the solid state. The controlling mechanism of that evolution is the interdiffusion of composite components (possibly termodiffusion:

$$div\left[\rho\left(Dgrad\ c+\frac{D^T}{T}grad\ T\right)\right]=0$$), which can form an eutectic composition.

Next are shown electron micrographs from the above work [12] (Fig. 19 - 21) of diffuse and eutectic melt zones formed during heating of studied composites in solid state. The explanations are provided below the figures. Detailed explanations can be found in that work.
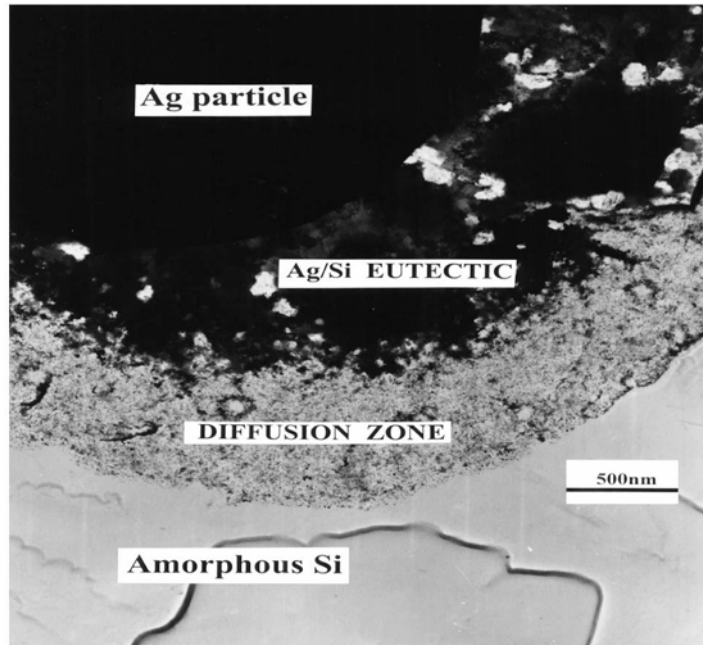

Fig. 19. Electron micrograph of diffuse and liquid eutectic zones formed by the interaction of silver particles and amorphous silicon film during annealing ($T = 850\ °C$) [12].
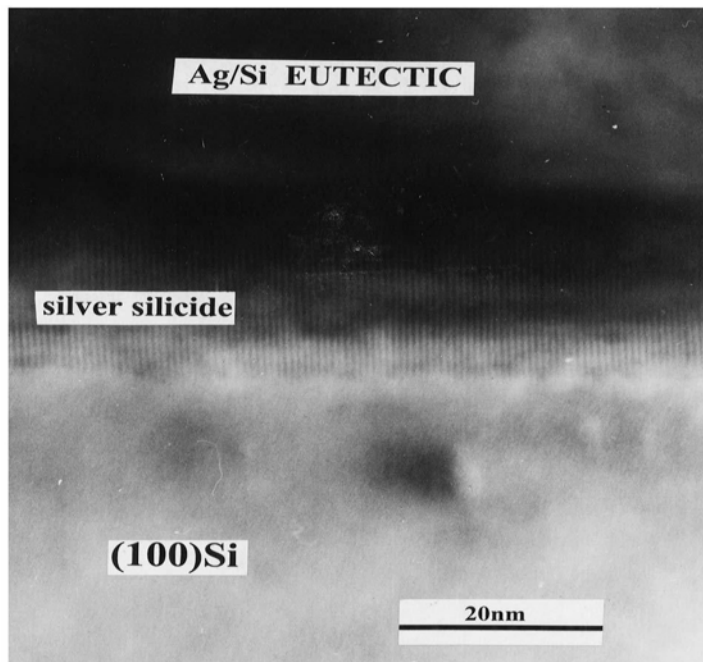

Fig. 20. HREM micrograph of oriented formation of eutectic melt in the system silver particle – crystal (100) of silicon ($T = 850\ °C$) [12].

On the basis of analysis of the results of direct experimental observation of the evolution of the interphase boundaries of simplest eutectic (and non-eutectic) binary compositions during transformation from the solid state into a liquid when heated [12] and the concept of internal energy sources a simplified model is constructed of the transition from surface boundary between solid phases to the volume one which have solid and liquid parts.
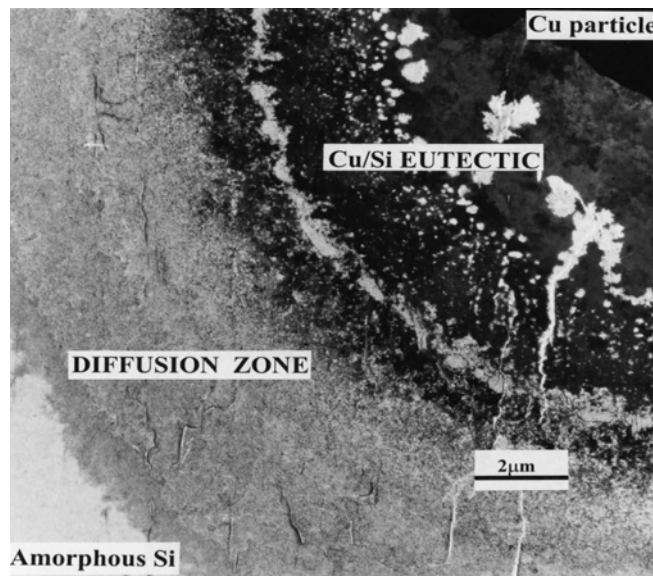
Fig. 21. Electron micrograph of diffuse zone and eutectic alloy formed by the interaction of copper particles with amorphous silicon foil under isothermal conditions ($T = 810$ °C) [12].

Main assumption: diffusion does not affect temperature distribution, but it strongly depends on the temperature.

Therefore, further we suppose that the temperature distribution $T(x,t), t \geq 0$ in the vicinity of the plane interface is known (see Fig. 18). Also known are dependencies $x_A(t)$, $x_B(t)$, $t \geq 0$. These values are determined by the solutions of Stefan type.

Model of phase interdiffusion.

It is assumed that interdiffusion is determined (mainly) by the dependence of the diffusion coefficient on temperature

$$D_i(T) = D_{0i} \exp\left(-\frac{W_i}{R(T - T_\gamma)}\right), \quad i = A, B, \tag{32}$$

where subscript i indicates phase, which diffusion is considered.

Instead of dependence (32) any other dependence can be used. Examples of direct experimental observation of processes of diffusion and evolution of interphase boundaries of simplest eutectic (and non-eutectic) binary compositions during the transition from solid state to liquid when heated can be found in [12].

Approximately, we assume that in the area of the melt $\left(x_A(t) \le x \le x_B(t)\right)$ phases are distributed homogeneously due to high values of diffusion coefficients at high temperature (see Fig. 22, where a scheme of distributions of phase concentrations in the vicinity of the interface is given). This assumption can be weakened by the assumption of their linear distribution (with a constant concentration gradient other than 0). However, it should be noted that this approach to the study of diffusion in the melt is very approximate. Diffusion in this area is a complex process, which is linked to other processes, and requires more in-depth research and modeling.
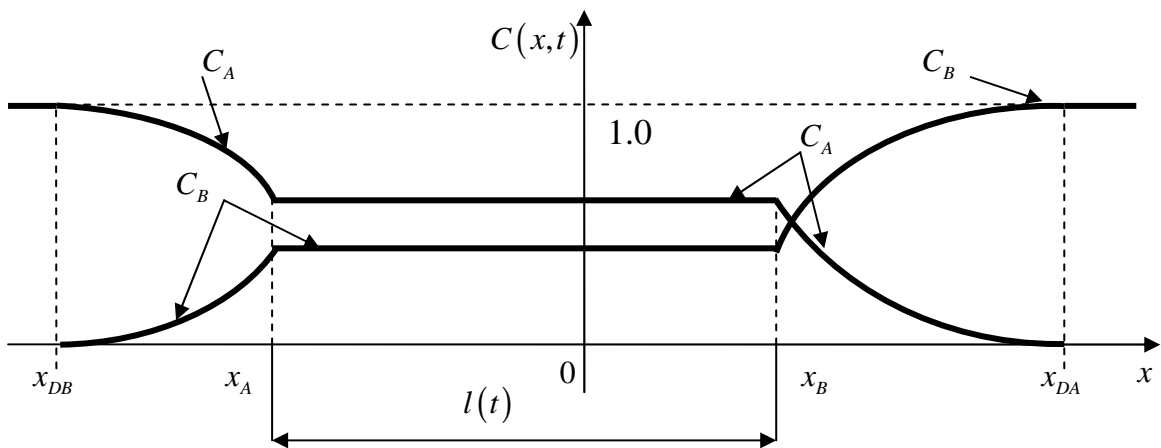

Fig. 22. Schematic distribution of concentration of phases A and B for some time moment $t > 0$. $l(t)$ – length of melt zone.

Further diffusion problem (for shortness) will be formulated for phase A. For phase B the problem is formulated similarly. Thus, in the region $\left(x_A(t) \leq x \leq x_B(t)\right)$ for concentration $C_A(x,t)$ we have

$$C_A(x,t) = C_A(x_A,t) = C_A(0,t) = C_A(x_B,t) = \tilde{C}_A(t), \quad \tilde{C}_A(0) = 1. \tag{33}$$

In the region $\left(x_B(t) \leq x \leq x_{DA}(t)\right)$ concentration $C_A(x,t)$ is found from equation

$$\frac{\partial}{\partial x}\left(D_A(T(x,t))\frac{\partial C_A}{\partial x}\right) = 0, \tag{34}$$

according to which concentration field $C_A(x,t)$ is considered in quasistatic approximation. Right end $x_{DA}(t)$ of region $\left(x_B(t) \leq x \leq x_{DA}(t)\right)$ is defined by temperature T_{DA}, at which diffusion of A component into B component stops, i. e. from equation

$$T(x_{DA},t) = T_{DA}. \tag{35}$$

From (32) for density of diffusion flux $F(t)$ of phase A in the analysed region we have

$$F(t) = -D_A(T(x,t))\frac{\partial C_A}{\partial x}. \tag{36}$$

Integrating the last equality in x, for concentration $C_A(x,t)$, $x_B(t) \leq x \leq x_{DA}(t)$, we have

$$C_A(x,t) = -F(t)\int_{x_B(t)}^{x}\frac{dx}{D_A(T(x,t))} + G(t), \quad t \geq 0, \tag{37}$$

where function $G(t)$ is found from the condition

$$0 = -F(t) \int_{x_B(t)}^{x_{DA}(t)} \frac{dx}{D_A(T(x,t))} + D(t). \qquad (38)$$

Therefore, equality (37) can be rewritten as

$$C_A(x,t) = F(t) \int_{x}^{x_{DA}(t)} \frac{dx}{D_A(T(x,t))}, \quad x_B(t) \le x \le x_{DA}(t), \quad t \ge 0. \qquad (39)$$

Finally, the distribution $C_A(x,t)$ will be known if we determine density of flux $F(t)$ of phase A. This density is determined from the condition of conservation of quantity of phase A:

$$l(t) - x_B(t) = C_A(x_B(t),t)l(t) + \int_{x_B(t)}^{x_{DA}(t)} C_A(x,t)dx,$$

which, taking into account (39), can be written as

$$l(t) - x_B(t) = l(t)F(t) \int_{x}^{x_{DA}(t)} \frac{dx}{D_A(T(x,t))} + F(t) \int_{x_B(t)}^{x_{DA}(t)} dx \int_{x}^{x_{DA}(t)} \frac{dx}{D_A(T(x,t))},$$

whence we obtain for the flux density $F(t)$

$$F(t) = \frac{l(t) - x_B(t)}{l(t) \int_{x}^{x_{DA}(t)} \frac{dy}{D_A(T(y,t))} + \int_{x_B(t)}^{x_{DA}(t)} dx \int_{x}^{x_{DA}(t)} \frac{dy}{D_A(T(y,t))}}. \qquad (40)$$

Thus, from the formulas (39), (40) for the distribution of concentration of phase A we obtain the following explicit formula

$$C_A(x,t) = \frac{[l(t) - x_B(t)] \int_{x}^{x_{DA}(t)} \frac{dy}{D_A(T(y,t))}}{l(t) \int_{x}^{x_{DA}(t)} \frac{dy}{D_A(T(y,t))} + \int_{x_B(t)}^{x_{DA}(t)} dx \int_{x}^{x_{DA}(t)} \frac{dy}{D_A(T(y,t))}}; \quad x_B(t) \le x \le x_{DA}(t), \ t \ge 0 \quad (41)$$

The peculiarity of the solution (41) is its uncertainty at $t = 0$: $C_A(0,0) = \dfrac{0}{0}$, which strongly depends on the functions $x_A(t), x_B(t)$ defined by the solution of the problem of Stefan type, as well as the solution $x_{DA}(t)$ of equation (35), which is determined by the type of dependence (32). This uncertainty can be resolved and examined using the solution of the discussed temperature problem or through computational experiments.
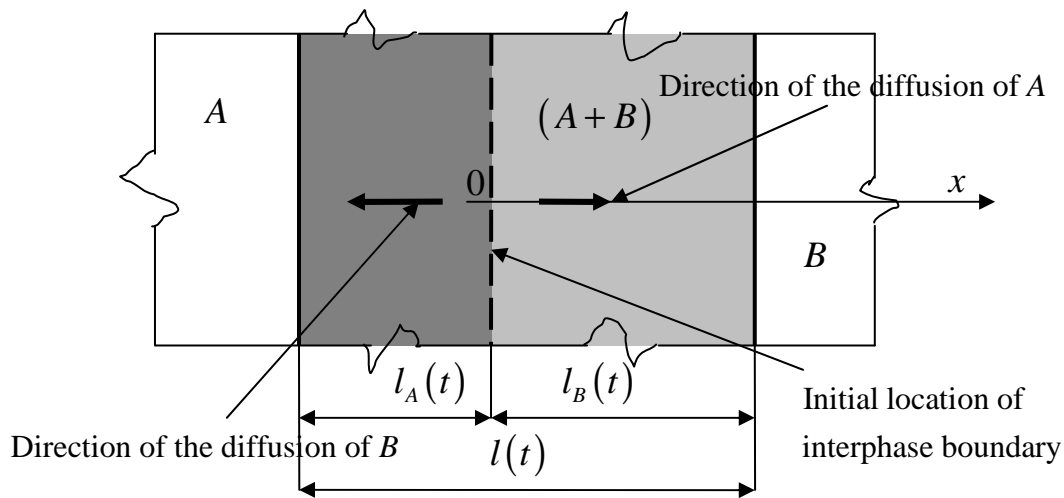
Fig. 23. Simplified scheme of evolution of flat boundary $x = 0$ between solid phases A and B ($T > T_\gamma, T_\gamma < T_M$).

When $x \geq x_{DA}(t)$ A phase is absent, and $C_A(x,t) \equiv 0$ so region $x \geq x_{DA}(t)$ consists only of phase B. In the case when A phase does not diffuse into solid phase B, formula (1.40) determines concentration $C_A(x,t)$ in the melt:

$C_A(x,t) = \dfrac{l_A(t)}{l(t)}$, $x_A(t) \leq x \leq x_B(t)$, $l_A(t) = -x_A(t)$. This case is shown in Fig. 23.

Fig. 23 gives simplified scheme of evolution of planar interphase boundary in the case of coincidence of diffusion and melt zones (or in the case when mismatch can be neglected) and notations used: $l(t)$ – thickness at time moment t of the liquid phase, which is located between solid phases A and B and consists of uniformly dissolved components A and B. The assumption of uniformity is justified in the

case of a higher rate of diffusion in the liquid than in the solid phase. $l_A(t)$, $l_B(t)$ - thicknesses of phases A and B dissolved in the melt at time moment t, respectively.

In this case, we can assume that $C_A = \dfrac{l_A}{l}$ and $C_B = (1 - C_A) = \dfrac{l_B}{l}$ are concentrations in the liquid of phases A and B, respectively.

Thus, main formulas of the model are as follows.

For the distribution of concentrations $C_A(x,t), C_B(x,t)$ of phases A and B under heating we have:

$$C_A(x,t)=\begin{cases} C_A(x_B(t),t),\ 0\leq x\leq x_B(t),\ t\geq 0; \\[4pt] \dfrac{[l(t)-x_B(t)]\displaystyle\int\limits_{x}^{x_{DA}(t)}\dfrac{dy}{D_A(T(y,t))}}{l(t)\displaystyle\int\limits_{x}^{x_{DA}(t)}\dfrac{dy}{D_A(T(y,t))}+\displaystyle\int\limits_{x_B(t)}^{x_{DA}(t)}dx\displaystyle\int\limits_{x}^{x_{DA}(t)}\dfrac{dy}{D_A(T(y,t))}};\ x_B(t)\leq x\leq x_{DA}(t),\ t\geq 0; \\[4pt] 0,\ x>x_{DA}(t),\ t\geq 0, \end{cases} \quad (42)$$

where functions $x_B(t), l(t), T(x,t)$ - are determinedfrom corresponding temperature problem of Stefan type, and implicit function $x_{DA}(t)$ is a solution of equation

$$T(x_{DA},t)=T_{DA}. \tag{43}$$

It is assumed that in (32) dependence of diffusion coefficient $D_A(T)$ from temperature is known.

As was noted earlier, the feature of the solution (42) (43) is its uncertainty at $t = 0$: $C_A(0,0) = \dfrac{0}{0}$, which strongly depends on the functions $x_B(t)$, $l(t)$, $T(x,t)$, $x_{DA}(t)$. This uncertainty can be resolved and investigated with the help of the previously mentioned temperature problem of Stefan type or computational experiments.

Conclusions

This section presents a new model of the evolution of the interphase boundary during heating, according to which surface boundary between the phases is transformed into a boundary that has thickness (is volumetric) and consists of two solid parts between which is liquid. The model was developed on the assumption that diffusion does not affect temperature distribution which is determined through solution of separate problem, but temperature affects diffusion through diffusion coefficient dependence on temperature.

4. Phase-field study of structure formation in binary eutectic

The goal of this work is the theoretical study and computer simulation of the processes of structure formation and the properties of interfaces in binary eutectic systems. As the result of the thermodynamical instability of the uniform composition, these systems tend to form spatial structures in the solid state, the eutectic colonies [13-15]. The significance of the study of the properties of eutectic systems for material science is due to wide industrial applications of these latter. This concerns, in particular, the processes of sintering in powder metallurgy, the utilization of the directional crystallization in manufacturing fiber composites for electronics and photonics, etc. The investigation of the properties of interfaces and the closely related phenomenon of contact melting are therewith the central points for understanding the processes of structure formation in eutectic systems.

Within the framework of the project, the following issues were considered:
(1) formation of eutectic structures from the overcooled melt (glass) obtained by the rapid quenching of the liquid $LaB_6 - ZrB_2$ eutectic;
(2) formation of eutectic colonies in the process of directional crystallization of $LaB_6 - ZrB_2$ ceramics;

(3) study of the fundamental interface properties and the phenomenon of contact melting in binary eutectic taking as an example the Cu-Si system.

As the investigation tool, the phase field theory (PFT) [16-18] with the dissipative microstructural alloy dynamics described by the parabolic equations for phase variables determining the local phase (liquid or solid) system state has been employed. The basic idea of PFT is to consider the inter-phase boundaries as the continuous spatial regions of finite width, the approach, which essentially simplifies the numerical calculations.

PFT equations and the model for binary eutectic

Within the PFT, the dissipative kinetics of a system is described in terms of phase-field variables. The relevant kinetic equations for an isothermal binary system can be obtained from the free energy functional,

$$F = \int \left[f(\varphi,c,T) + \frac{\varepsilon_C^2}{2}(\nabla c)^2 + \frac{\varepsilon_\Phi^2}{2}(\nabla \varphi)^2 \right] dV , \qquad (44)$$

where $f(\varphi,c,T)$ is the free energy density; T, c, and φ denote the temperature, concentration and the phase field variable, respectively. The phase-field variable specifies the local state, $\varphi = 0$ for solid, and $\varphi = 1$ for liquid phase. By applying the basic principles of thermodynamics, one obtains the PFT-equations (with allowance for the convective medium motion with the velocity v_0 along the OX axis), in the form [16-17]

$$\frac{\partial \varphi}{\partial t} = -M_\Phi \left[\frac{\partial f}{\partial \varphi} - \varepsilon_\Phi^2 \nabla^2 \varphi \right] + v_0 \frac{\partial \varphi}{\partial x} \qquad (45)$$

$$\frac{\partial c}{\partial t} = \nabla \cdot \left[M_C c(1-c)\nabla\left(\frac{\partial f}{\partial c} - \varepsilon_C^2 \nabla^2 c \right)\right] + v_0 \frac{\partial c}{\partial x} \qquad (46)$$

Here the quantities M_Φ and M_C are the kinetic coefficients specifying the relaxation rate of the system to the equilibrium; ε_Φ and ε_C are the parameters

responsible for the surface energy of solid-liquid and solid-solid interfaces. The specific features of a system are determined by the particular form of free energy density $f(\varphi,c,T)$. In this work we use for the latter the standard expression for a non-ideal binary system with the miscibility gap [16]

$$
\begin{aligned}
f(\varphi,c,T) &= (1-c)f_A(\varphi,T) + cf_B(\varphi,T) \\
&+ \frac{RT}{v_m}[c\ln c + (1-c)\ln(1-c)] + c(1-c)[\Omega_S[1-p(\varphi)] + \Omega_L p(\varphi)].
\end{aligned}
\tag{47}
$$

The typical minimum in the melting curve on the phase diagram is therefore due to the difference in mixing energies for liquid and solid phases. Here R is the gas constant, v_m is the molar volume, Ω_S and Ω_L are the mixing energies for the solid and liquid state, respectively. The component free energies $f_A(\varphi,T)$ and $f_B(\varphi,T)$ have the form

$$
f_{A,B}(\varphi,T) = W_{A,B}g(\varphi) + L_{A,B}\frac{T_M^{A,B} - T}{T_M^{A,B}}p(\varphi)
\tag{48}
$$

where $T_M^{A,B}$ are the melting temperatures, $W_{A,B}$ are the energy barriers associated with the surface energy of liquid-solid interfaces, $L_{A,B}$ are the component latent heats for the components A and B; the functions $g(\varphi) = \varphi^2(1-\varphi)^2$ and $p(\varphi) = \varphi^3(10 - 15\varphi + 6\varphi^2)$ are the model barrier and interpolating functions constructed in such a way as to describe the liquid-solid interfaces of a finite width. The kinetic coefficients M_Φ and M_C are determined for a binary system as

$$
M_\Phi = (1-c)M_A + cM_B
$$

$$
M_C = \frac{D_S + p(\varphi)(D_L - D_S)}{RT/v_m}
\tag{49}
$$

with D_S and D_L being the solid and liquid diffusivities, respectively.

As was shown in recent experiments with formation of diffusion zone and contact melting in binary eutectic, the equilibrium interface can exhibit

complicated (three-phase) structure and the width of the order of several micron [19, 20]. This means that the interface width (as well as the surface energy) is a real physical quantity (but not the model parameter, as, for instance, in Ref. [18]), which has to be determined from the experiment.

For numerical solution of the equations (45-46) there has been employed in all cases the finite element method implemented in the free program package FEniCS [21].

Simulation of the crystallization of eutectic structures from the overcooled melt

To investigate the crystallization of the eutectic from the melt obtained as the result of rapid quenching, the PFT equations (45-46) have been solved within the isothermal approximation. The initial state of a binary system has been specified as the overcooled liquid state (i.e. as the eutectic glass); the composition was set uniform, with constant concentration and the Gaussion noise of 0.025-0.035 amplitude, with the distribution of the phase variable corresponding to the liquid ($\varphi = 1$) or solid ($\varphi = 0$) state. The temperature was set below the eutectic temperature in the area of the solid state with the eutectic composition; the homogeneous Neumann's boundary conditions were used.

The model PFT parameters were chosen to be as close as possible to the available experimental data for the real binary $\mathrm{LaB_6 - ZrB_2}$ ceramics [15], or to reproduce the known component properties (Table 5). For instance, the latent heats and mixing energy, which determine the equilibrium properties of the system, were adjusted to reproduce the eutectic point on the phase diagram; the kinetic coefficients were estimated from the available experimental data on the velocity of the directional solidification; the values for the gradient coefficients were chosen to reproduce the typical geometrical parameters of eutectic colonies.

Table 5. Parameters for the PFT model used in simulations of eutectic crystallization from the overcooled $LaB_6 - ZrB_2$ melt.

Parameter	Value		Units
Density, ρ	LaB_6	4730	kg/m^3
	ZrB_2	6090	
Simulation cell size, X	$0.5 - 40.0 \cdot 10^{-6}$		m
Melting temperature, T_m	LaB_6	3000	°K
	ZrB_2	3310	
Kinetic coefficient for the inter-phase boundary, $\mu_A = \mu_B$	$1,0 \cdot 10^{-6}$		m /(°K sec)
Liquid and solid diffusivities, D_L, D_S	$1,0 \cdot 10^{-10}, \ 1 \cdot 10^{-13}$		m^2/sec
Surface energy for the liquid-solid interface, $\sigma_A = \sigma_B$	5,0		J/m^2
Molar volume	LaB_6	$43,1 \cdot 10^{-6}$	$m^3/mole$
	ZrB_2	$16,35 \cdot 10^{-6}$	
	Eutectic	$35,3 \cdot 10^{-6}$	
Eutectic temperature for $LaB_6 - ZrB_2$	2740		°K
Latent heats, L	LaB_6	$3200 \cdot 10^6$	J/m^3
	ZrB_2	$7200 \cdot 10^6$	
Mixing energy for solid state, Ω_S	$2800 \cdot 10^6$		J/m^3
Eutectic concentration	0,32		-

In numerical solution of PFT equations the spatial domain was chosen within the range of X=0.5-40.0 micron; the liquid-solid interface width (the model parameter) was set δ/X =0.05. The absolute error of computations for the composition and phase profiles was kept less than 10^{-3}.

All the parameters entering PFT equations, which are necessary for solving the problem, can be expressed via the quantities given in Table 5 by using the known relations [16].
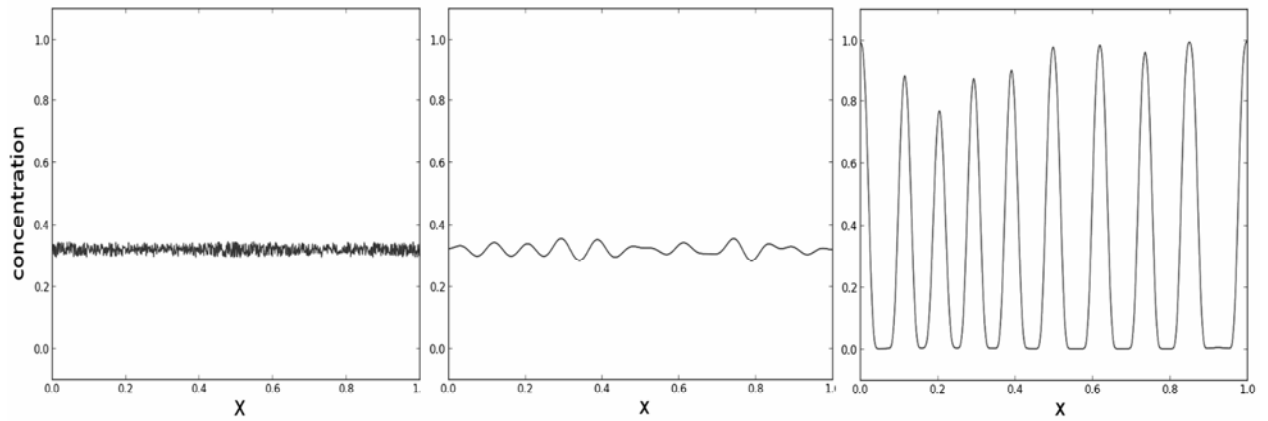
Fig. 24. The results of 1D-simulations of eutectic structure formation from glassy state in $LaB_6 - ZrB_2$ for the temperature $T = 2000^o K$ for the time points $t=0$; 4; 280 sec (from the left to the right).
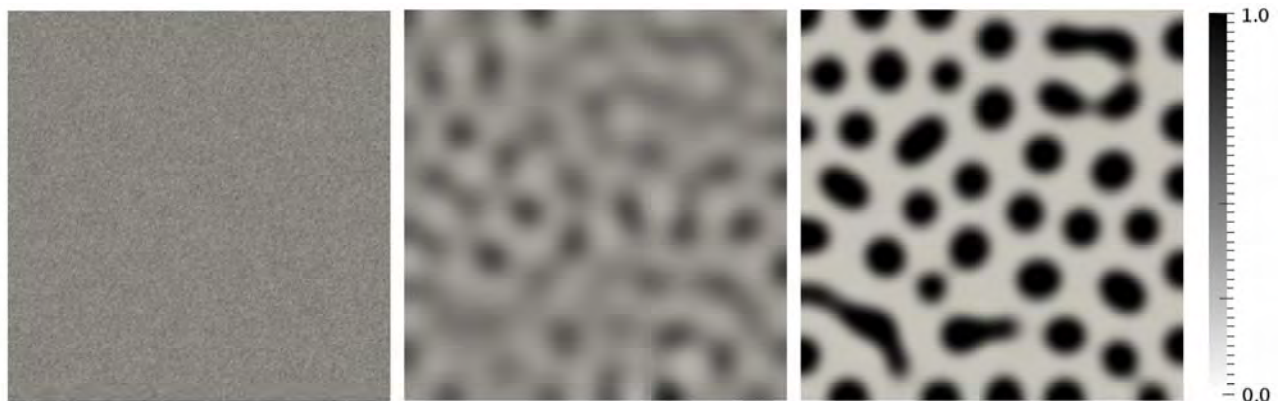

Fig.25. The results of 2D-simulations (composition distribution) of the formation of eutectic structure in $LaB_6 - ZrB_2$ from glass at the temperature $T = 2000^o K$ for the time points $t=0$; 60; 180 sec (from the left to the right).

The results of 1D- and 2D-simulations of the behavior of the system with the eutectic composition after the rapid quenching to the temperature $T = 2000^o K$ are given in Figs. 24 and 25. It should be mentioned that at the initial stage the system crystallizes into the weakly structured solid phase, therefore, the process of the formation of colonies occurs in the solid phase, that is, actually, from glass.

The above simulations reproduce the process of the formation of the spatial structures as a whole. It is worth mentioning that the series of very long runs ($t > 10^5$ sec) have demonstrated the capability of the model to reproduce the complete decomposition of the system into components while approaching the final equilibrium state.

Simulation of the directional crystallization of fiber structures in ceramics

The directional crystallization was studied in the "frozen temperature approximation", i.e. the temperature distribution was supposed to be steady and linear along the direction of sample motion. Such an approximation is justified, since the temperature conductivity coefficient of boride ceramics considerably exceeds the mass transport coefficients. The initial phase distribution was set in the form of the smoothed Heaviside function describing the liquid-solid interface with the front at the eutectic temperature. The initial composition distribution was set equal to the constant eutectic concentration with the Gaussian 0.025-0.035 amplitude noise (Fig.26-27)

The simulations have been performed for parameters given in Table 5. The spatial domain of simulations was within the range X=20.0-40.0 mkm; the temperature gradient was set equal to $4.5 \cdot 10^7$ K/m; the velocity of the directional crystallization was in the range $v_0 = 0.25 - 2.0 \cdot 10^{-5}$ m/sec.

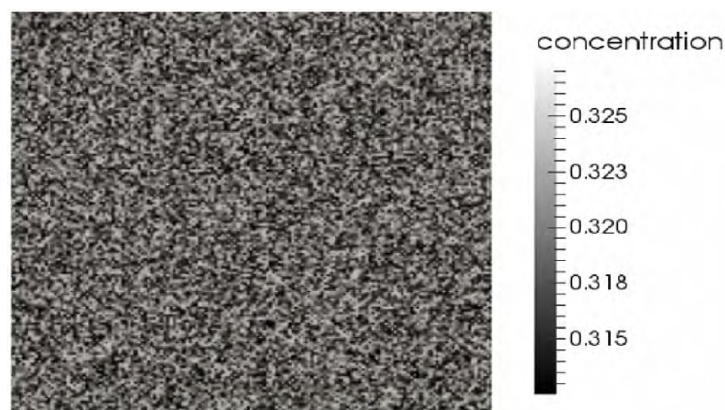Fig.26. Initial distributions for the concentration.

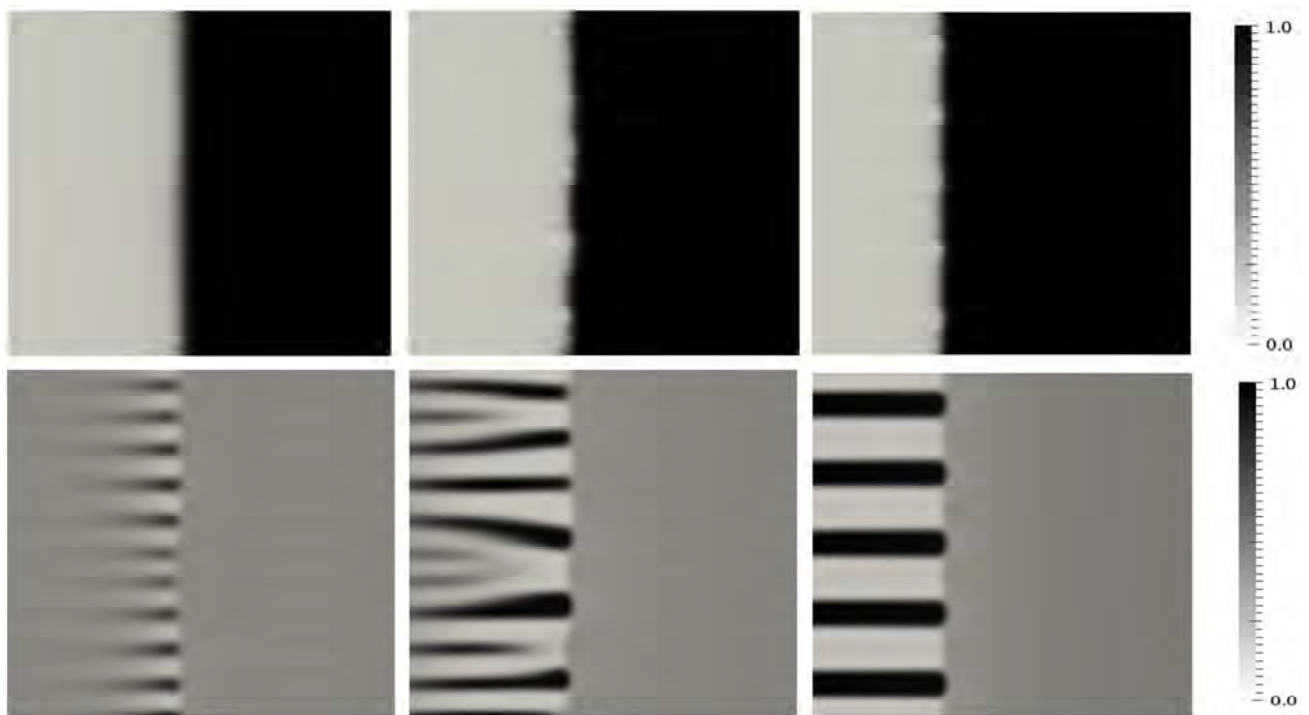Fig.27. Initial distributions for the phase.

Fig.28. The results of 2D-simulations for the phase (top) and concentration (bottom) for the initial stage of the process of the directional crystallization for $t=1$; 2; 12 sec (from the left to the right). The velocity of the melt motion (from the right boundary) is $v = 0.5 \cdot 10^{-3} cm/\sec$.
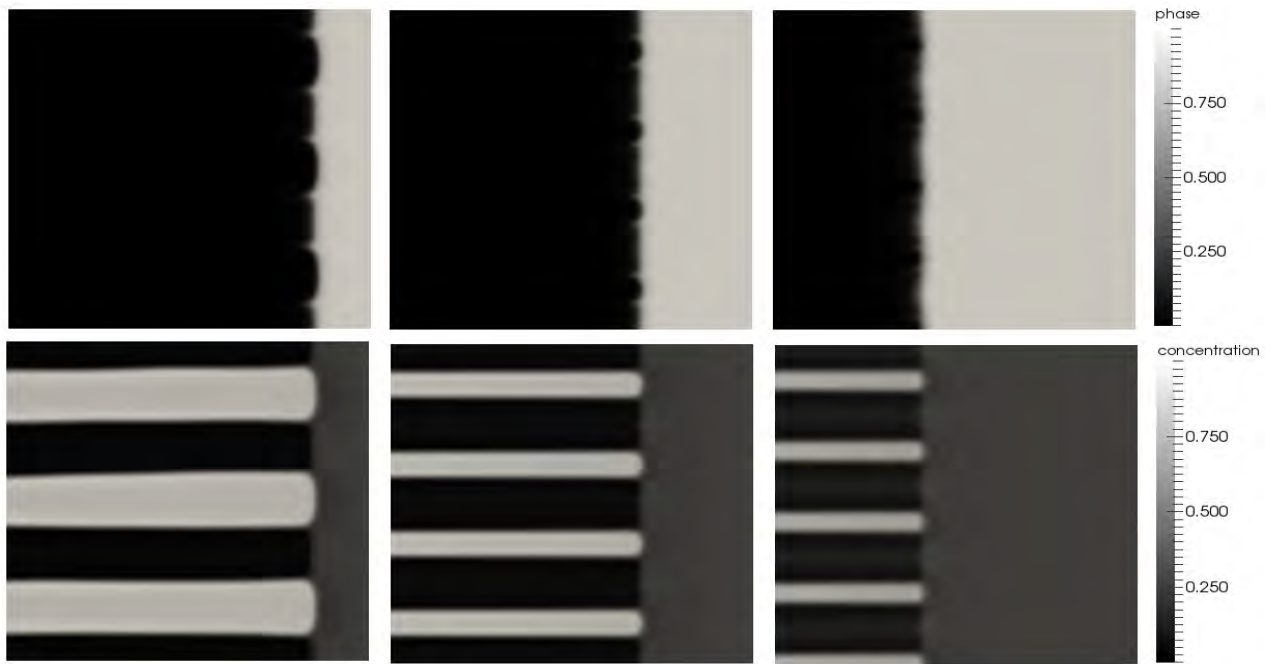
Fig.29. The results of the 2D-simulations of the directional crystallization for the phase (top) and concentration (bottom) for the time point t=20 sec and the melt velocity (from the right boundary) $v = 0.5 \cdot 10^{-5}$; $0.75 \cdot 10^{-5}$; $1.25 \cdot 10^{-5} m/\sec$ (from the left to the right).

The results of 2D-simulation of the directional crystallization in boride-boride ceramics are given in Fig. 28. At the initial stage, there emerges an instability on the crystallization front, which gives rise to the composition segregation and the formation of a cell structure along the front. Then, at the transitional stage, a part of cells gets destroyed and the eutectic structure growth larger. Finally, due to the transition processes, there forms a steady-state fiber structure representing the eutectic colony being the result of the directional crystallization. The results are in agreement with the known experiments [15]. Notice that the simulations clearly demonstrate the stabilizing effect of the directional melt motion on the structure formed. In particular, the fact of the existence of the minimal velocity needed for the directional crystallization is reproduced.
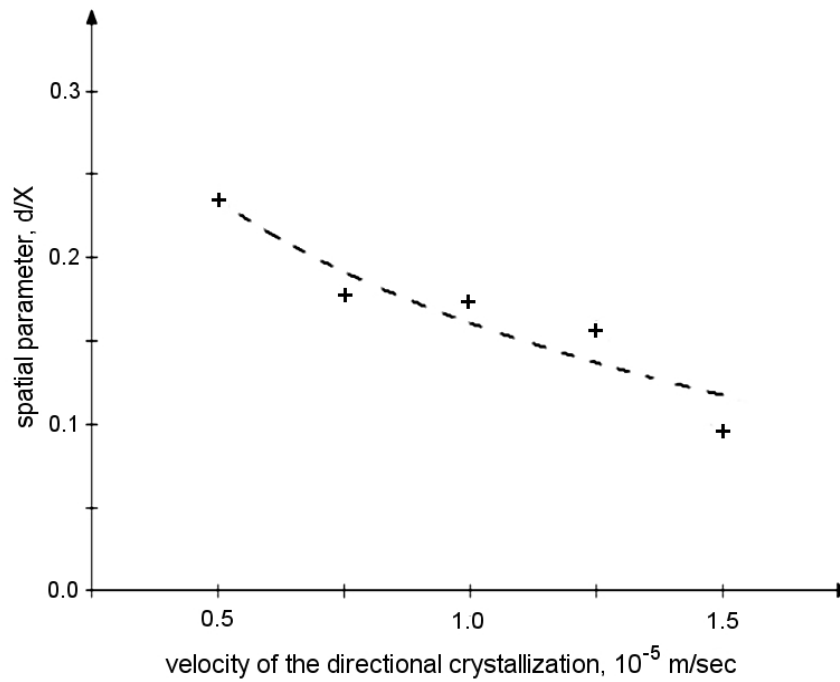
Fig.30. Dependence of the space parameter of the fiber structure on the velocity of the directional crystallization of $LaB_6 - ZrB_2$. The results of PFT-simulations are marked as "+".

The simulation results for different velocities of directional crystallization are given in Fig.29. As follows from the data obtained, the typical space parameter of the fiber structures formed depends on the velocity. Growing velocity of the directional crystallization results in smaller colonies. The relevant dependence is given in Fig. 30. Also, the simulations reproduce the existence of the maximal threshold velocity of the directional crystallization, above which the structures do not form. In these calculations this threshold was estimated as $v = 1.75 \cdot 10^{-5} m/\sec$. Apparently, this is due to the fact that rate of the diffusive processes in this case turns out to be insufficient to provide the component segregation. Let us note that these results correlate qualitatively with the known experiments [15].

Study of the contact melting and the structure of binary eutectic near the eutectic point

The study of the interface phenomena in binary eutectic was aimed basically at the phenomenon of contact melting (CM) and the properties of diffusion zone. The goal was to obtain the interpretation for the results of recent experiments with binary systems consisting of metal Au, Al, Ag, and Cu particles (of $\approx 5 \cdot 10^{-6} m$ size) placed on amorphous or crystalline silicon films [19, 20]. The general conclusions obtained in these works can be formulated as follows: 1) for the temperatures below the eutectic point, under isothermal conditions, the solid-solid interface forms a diffusion zone (DZ) with typical width of $\approx 10^{-5} m$, which may reduce in size for lower temperatures; 2) for the temperatures within the range $10 - 20°C$ above the eutectic point, under isothermal conditions, the formation of the liquid eutectic layer at the interface (i.e., the phenomenon of CM) is observed, which is, however, always preceded by the formation of the DZ.

In simulations there has been used the standard model formulated in Sec. 2. It should be noted that the basic idea underlying all the following consideration is that the DZ can be viewed as the diffuse solid-solid interface associated with the state of the equilibrium with complete decomposition. Furthermore, we neglect the effects of a large number of possible compounds in DZ with different structural and thermodynamical properties, and use the concentration field as the only variable describing the composition.

We give here the results of PFT simulations for Cu-Si system. The following parameters were used ($A \equiv Cu; B \equiv Si$): the domain of solution $X_m = 2.0 \cdot 10^{-5}$ m; time interval $t_{max} = 4000\ sec$; melting temperatures $T_M^A = 1357$ °K and $T_M^B = 1685$ °K; latent heats $L_A = 1.837 \cdot 10^9\ J/m^3$ and $L_B = 4.488 \cdot 10^9\ J/m^3$; molar volume $v_m = 8.57 \cdot 10^{-6}\ m^3/mole$; surface energies for liquid/solid interfaces $\sigma_A = \sigma_B = 0.3\ J/m^2$; diffusivities $D_S = 10^{-13}\ m^2/sec$ and $D_L = 10^{-9}\ m^2/sec$; kinetic

parameters for interfaces $\mu_A = \mu_B = 5 \cdot 10^{-5} \, m/(°Ksec)$; mixing energy for solid phase $\Omega = 3.635 \cdot 10^9 \, J/m^3$.

Most of the above parameters are the experimental data available for Cu-Si system or the typical numbers for the relevant quantities (like solid/liquid diffusivities) used in similar simulations [22-24]. The experimental value for the important quantity Ω is not available in the literature; we fitted it to make the eutectic temperature match its experimental value $T_{eut} = 1075°K$. In order to make computer simulations less time consuming, the kinetic coefficients $\mu_{A,B}$ were set much less than the typical values used in similar PFT simulations [24]. However, it is to emphasize that the simulations performed were aimed at the investigation of the steady (equilibrium or metastable) states, and, as is seen from Eq. (46), the kinetic coefficients affect the rate of the dissipative relaxation of the system rather than the final steady states. The important for the model quantity, the width of the DZ, is determined by the concentration gradient coefficient ε_C. The latter was fitted as well to provide the typical value $d \approx 4 \cdot 10^{-6} \, m$ observed experiments. The associated interfacial energy of DZ evaluated in simulations was on the order of $\Sigma \approx 500 \, J/m^2$.

The above parameters $\sigma_{A,B}$ and $\mu_{A,B}$ are needed to calculate the phase gradient coefficient ε_Φ, the barrier energy $W_{A,B}$, and the kinetic parameters $M_{A,B}$ entering the PFT equations; for this purpose, the standard relations given in Ref. [16] were employed. The model parameter specifying the liquid-solid interface width was set $\delta / X_{max} = 0.01$.

The absolute error for composition and phase profiles obtained in computations was kept less than 10^{-5}.
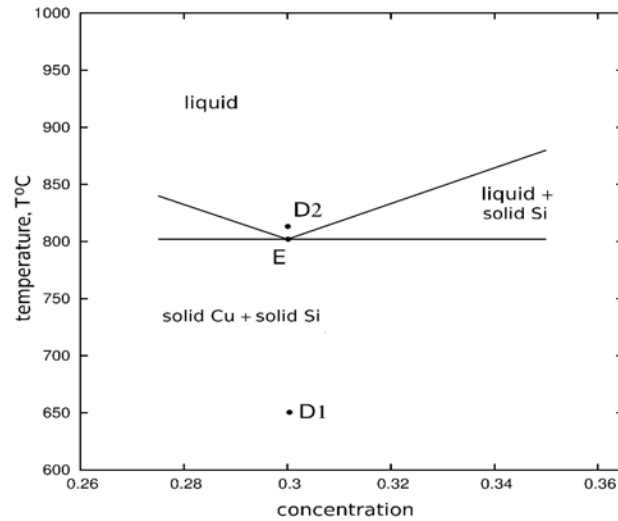
Fig. 31. Experimental phase diagram of Cu-Si in the vicinity of the eutectic point [22]. The eutectic concentration is 0.3.

A part of the experimental phase diagram for Cu-Si near the eutectic point [22] is displayed in Fig. 31 To reproduce the results of experiments with the formation of the DZ [19], we performed PFT simulations in 1D (planar) geometry for the points D1 ($T_{D1} = 923°K\,(650°C)$) and D2 ($T_{D2} = 1083°K\,(810°C)$) for the eutectic concentration c=0.3. For this purpose Eqs. (45-46) were solved with initial conditions describing a contact of two solid components (Fig. 32, line 1).

Fig. 32. Initial concentration profiles (solid lines 1 and 2) and phase distribution (dashed stochastic line) used in PFT simulations.

Fig. 33. Final steady-state profiles for phase (dashed line) and composition (solid lines) obtained in PFT simulations for the temperatu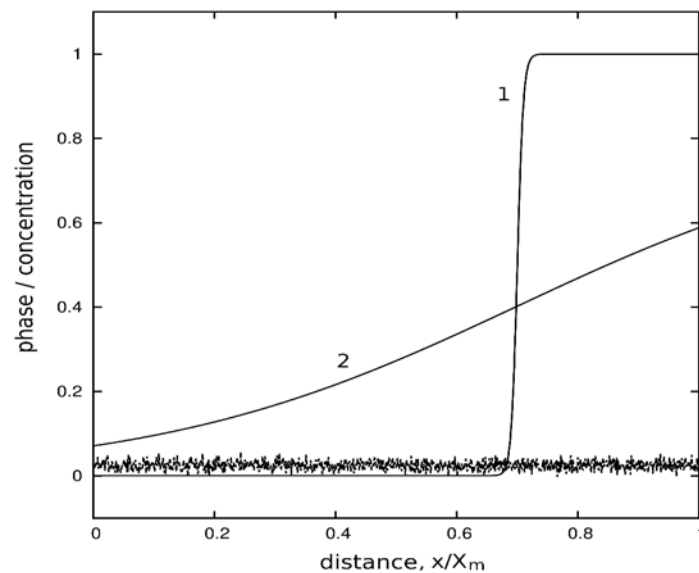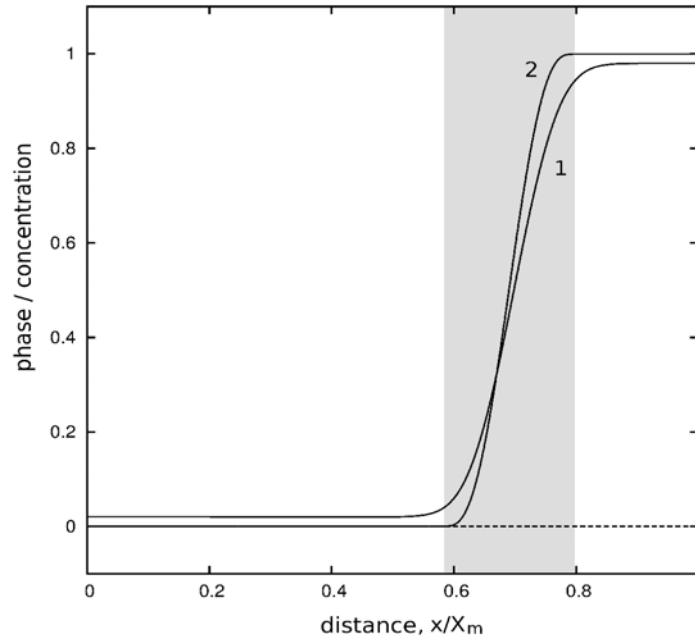res $T_{D1} = 923°K \, (650°C)$ (line 1) and $T_2 = 473°K \, (200°C)$ (line 2) for the time point $t = t_{max}$ (4000 sec).

Notice, that the PFT equations allow overheated metastable solid state ($\varphi = 0$) to exist infinitely long. For this reason, to trigger the kinetic processes, the initial phase distribution was modified to include 0.05-0.15 - amplitude random noise. In principle, the effects of random fluctuations can be taken into account by adding noise source to PFT equations or using the renormalization approach [25-27]. However, we did not consider the fluctuations in simulations, since these latter affect the kinetics rather than the final steady states.

The results of simulations for the temperatures specified in experiments with Cu-Si system [19] are displayed in Figs. 33, 34. For the temperature $T_{D1} = 923°K \, (650°C)$ below the eutectic point (Fig. 33), the simulations show that, as the result of the relaxation, there forms a final steady state corresponding to 'solid A + diffuse interface + solid B' composition profile. It is worth mentioning that using any of the initial composition distributions given in Fig. 32 yields identical final steady-state composition profiles, which is the result of the equilibrium nature

of this state. The area in grey (diffuse interface) in Fig. 32 is interpreted as a DZ. Another important observation obtained in PFT simulations is the reduce in the width of DZ with lowering the temperature.

The simulations performed for the temperature $T_{D2} = 1083°K\ (810°C)$ above the eutectic point (Fig. 34) indicate the formation of a liquid area within the steady DZ, quite consistent with experimental observations [19]. Notice that the steady three-phase (solid A + liquid + solid B) profiles can be viewed as the state of complete decomposition (like those shown in Fig. 33), but with a liquid interface. It is to mention that similar simulations performed for the parameters specific for Ag-Si system yielded quite analogous results.

The fundamental question, which arises in this context, is that of the nature of the steady states observed, i.e., if they are *metastable or equilibrium* ones. To address this question, we performed series of runs with various initial conditions in the vicinity of the expected eutectic point with monitoring the free energy of the system defined by Eq. (44). Depending on the initial phase and concentration distributions, for the same temperature and average concentration (i.e., for the same point on the phase diagram), the system may be "trapped" in a metastable state, or proceed to the thermal equilibrium.

An example of the behavior of free energy during relaxation for the temperature $T_{D2} = 1083°K\ (810°C)$ and eutectic concentration $c = 0.3$ (point D2) for the three-phase (DZ with liquid interface) and two-phase (DZ) states is given in Fig. 35 (with free energy density measured in units of $f_0 = RT_A^M / v_m = 1.317 \cdot 10^9\ J/m^3$).

The free energy density for liquid state evaluated for the same point on the phase diagram is much higher, $f_L / f_0 = 0.0705$. Therefore, one must conclude, that 1) the liquid state at the point D2 is metastable; 2) thermal equilibrium in the system is associated with the steady three-phase 'solid A + liquid + solid B' state, because it has the lowest free energy.
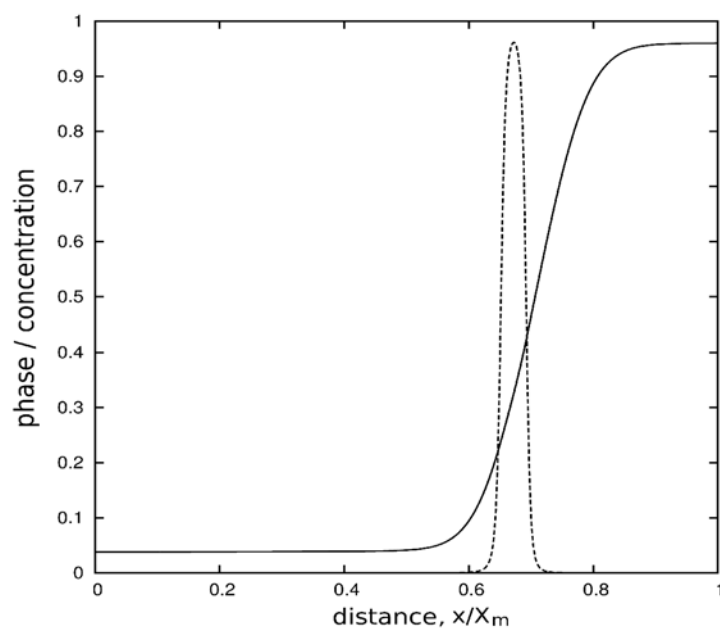
Fig. 34. Final steady-state profiles for phase (dashed line) and composition (solid line) obtained in PFT simulations for the temperature $T_{D2} = 1083°K \left(810°C\right)$ (point D2).
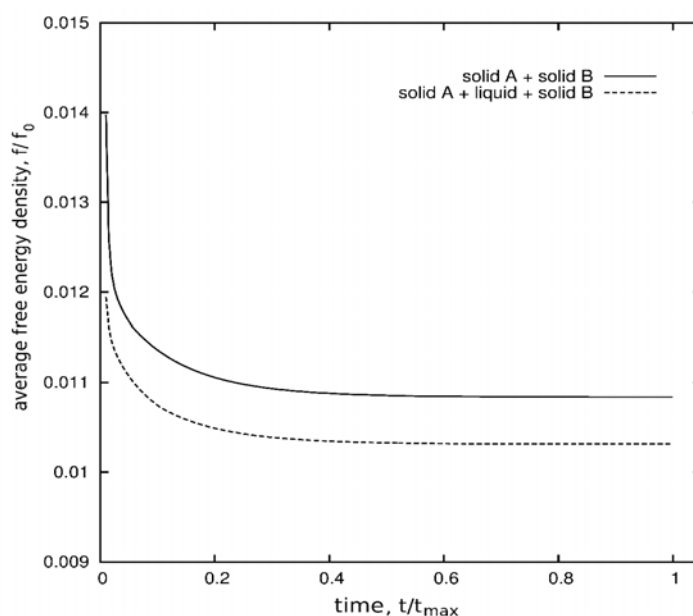
Fig. 35. Average free energy density of the system as a function of time for the temperature $T_{D2} = 1083°K \left(810°C\right)$ and eutectic concentration $c = 0.3$ for the steady states: solid A + solid B (complete decomposition; solid line); solid A + liquid + solid B (complete decomposition with a liquid interface; dashed line).
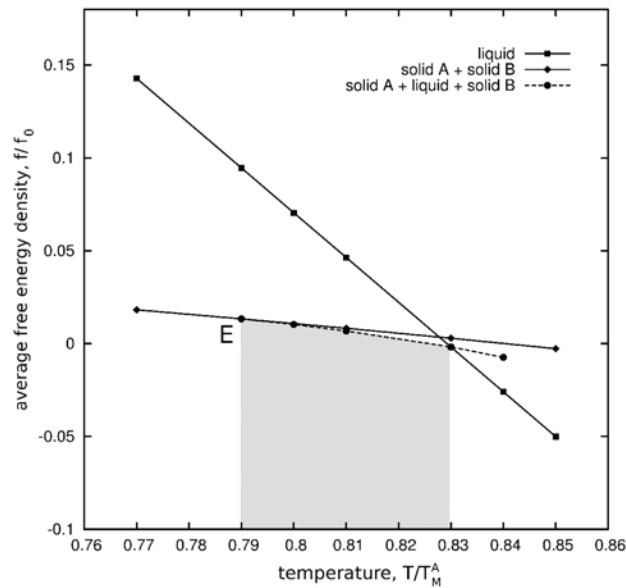
Fig. 36. Average free energy density of the system vs. temperature for different steady states for the eutectic concentration c=0.3. The area in grey points to the temperature interval, where the three-phase state has the lowest free energy.
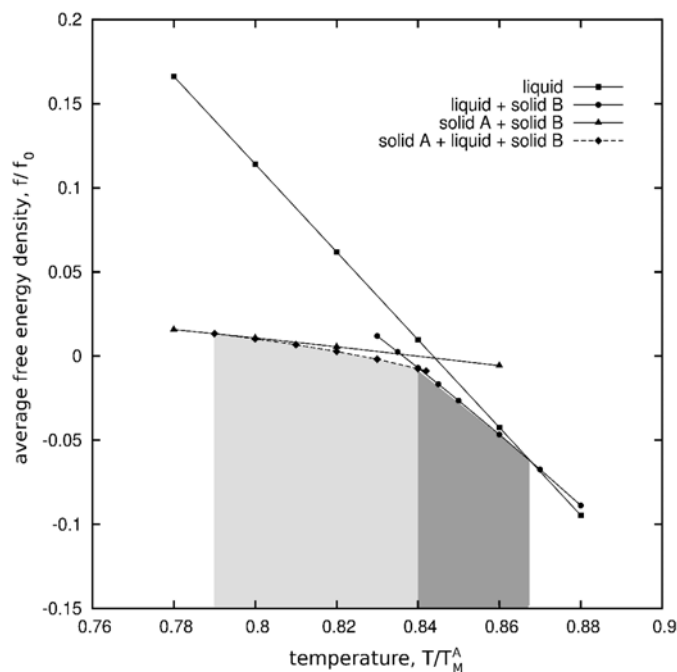
Fig. 37. Average free energy density of the system vs. temperature for different steady states for the concentration c=0.4. The areas in light and dark grey point to

the temperature intervals of thermodynamical stability of three-phase 'solid A + liquid + solid B' and two-phase 'liquid + solid B' states, respectively.
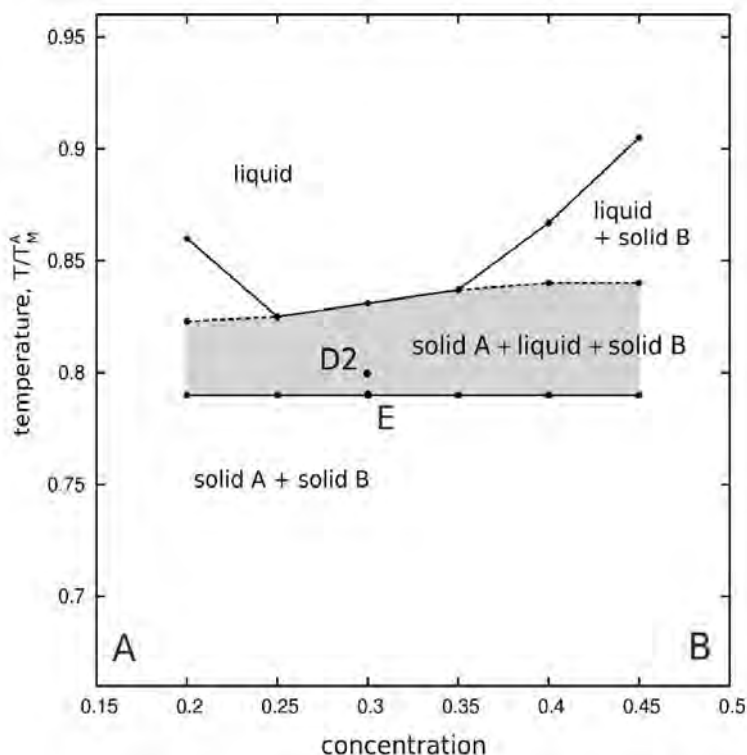
Fig. 38. Phase diagram near the eutectic point obtained from PFT simulations

It is to emphasize, that this theoretical (based on PFT) conclusion, while being consistent with above cited experiments, contradicts the experimental phase diagram (Fig. 31), since the point D2 lies here within the area of liquid phase. To examine this issue in more detail, we performed further simulations aimed at the evaluation of free energy of possible steady states in the vicinity of eutectic point and deriving the associated phase diagram. The results are given in Figs. 36-38.

The most unexpected finding is that, according to the PFT model used, the solidus line $T = T_{eut}$ turns out to have a 'fine structure', i.e., it splits and expands to the relatively narrow (about $\approx 50°C$ width) area above the eutectic temperature, where the above mentioned states describing the complete decomposition with the

liquid interface ('solid A + liquid + solid B') are thermodynamically stable. The point D2 lies therewith within this area, which explains the experimental observations of the DZ with the layer of liquid eutectic [19].

In this context a few words should be said about the standard technique of the common tangent construction for obtaining phase diagrams. The latter ignores the gradient terms in the free energy functional (44) and, therefore, implies the equilibrium in the system to be associated with the uniform concentration and the phase field. As the result, the contribution to the free energy of the interfaces is neglected and the description of the complicated interfaces like given in Fig. 34 with high interfacial energy is impossible. Notice that the profiles given in Fig. 34 are the exact solutions of the PFT equations (45-46) associated with the thermal equilibrium, therefore, they provide the exact relation for the chemical potential $\mu = const$ over all the domain of solution. Within the three-phase interface, this relation holds as well, while the concentration and phase distributions are clearly not uniform. Thus, it is natural to assume that the changes observed in the phase diagram obtained by solving PFT equations are due to the account of interfacial energy.

Thus, we see that the standard PFT model (45-47) formulated above reproduces the general properties of phenomena associated with the formation of DZ and CM near the eutectic point, in particular, in the systems with amorphous Si. As for the experiments with crystalline Si films, they may reveal more complicated properties of the DZ [20]. Apparently, to describe these latter more adequately, the detailed description of component structures occuring in DZ is needed, eventually, by using the multi-phase version of PFT [28, 29]. At the same time, the basis for the consideration is the assumption is that the relatively wide DZ is associated with the equilibrium state of complete decomposition with high interfacial solid-solid energy, and the crucial for the model parameter, the DZ width, still remains of the same order.

The results of simulations suggest that the three-phase states and the associated properties of eutectic phase diagram would be rather common for eutectic systems. Another phenomenon, which can be viewed as the manifestation of the formation of three-phase-states, is the micro-separation of phases observed within the liquid eutectic above the eutectic point [13,14]. The experiments clearly demonstrate the strong deviation from the regular liquid structure in liquid eutectic even on macroscopic scales, especially, after the long-term (during several hours) keeping in isothermal conditions.

Conclusions

By means of computer simulations based on the standard PFT model with the miscibility gap in solid state, the following issues were examined: (1) structure formation in binary $LaB_6 - ZrB_2$ eutectic as crystallized from the overcooled melt; (2) formation of ordered fiber structures in directional crystallization of $LaB_6 - ZrB_2$; (3) interfacial phenomena in binary eutectic: the formation of diffusion zone and contact melting in Cu-Si system.

The simulations as a whole reproduce the basic features of eutectic structures observed in experiments with boride-boride ceramics, - the spatial component segregation and formation of structure from glass, the complete system decomposition in the process of relaxation to the thermodynamical equilibrium, formation of colonies in directional crystallization. Further progress in description of structure formation in boride composites should be expected with refining the experimental parameters needed for formulation of PFT models, and with implementation of more detailed 3D models [28,29], which take into account the differences in the crystal structure of the components.

The simulations of the interfacial phenomena in Cu-Si predict the existence of equilibrium three-phase (solid-liquid-solid) states above the eutectic temperature describing the complete decomposition with a liquid interface. The results of

simulations demonstrate the role of the interfacial energy as the possible mechanism for the phenomena of contact melting and formation of diffusion zone observed in the experiments with binary metal-silicon systems. In addition, the results obtained provide the explanation of the phenomenon of phase separation in liquid eutectic.

II. MICROSCALE

5. Calculation of physical and mechanical characteristics of MeB$_2$ (Me - Ti, Zr, Hf) BORIDES; LaB$_6$ AND composites in the LaB$_6$ - MeB$_2$ systems on the basis of a priori pseudopotential

The promising prospects for the use of materials on the basis of LaB$_6$ - MeB$_2$ in various branches of engineering cause high interest in determining their strength characteristics for which data are virtually absent [30-32] especially for composite materials. Therefore, the issue of calculating the strength characteristics of composites LaB6 - MeB2 (Me - Ti, Zr, Hf) with eutectic composition is high on the agenda.

In the previous project (EOARD N P-273) a model was developed [33], which allowed to construct thermodynamic potentials of quasi-binary eutectic systems LaB$_6$-MeB$_2$, and calculate for them the concentrations of the components and melting point temperature in the eutectic point.

The energy of the electron-ion system was calculated using method of a priori pseudopotential [34] and concept of intermolecular interaction [35]. Intermolecular interactions by nature are close to interatomic interactions and are described by the same kind of potentials as the interatomic. The concept of intermolecular interaction becomes useful when it comes to interaction of the components in the alloy, especially when the components are made up of different atoms (LaB$_6$ or MeB$_2$).

In the method of pseudopotentials the energy of electron-ion system attributed to the unit cell (molecule) is the sum of the energy of electrons and ions included in its structure. Part of this energy, which depends on the type of crystal lattice energy is responsible for the pairwise intermolecular interaction. In calculating the energy of interaction between heterogeneous molecules the virtual crystal model approximation is accepted. For this purpose Helmholtz

thermodynamic potential is built, which depends on the temperature and concentration of the components. From the extreme condition of the thermodynamic potential, were calculated characteristic parameters of the eutectic (the concentration of the component and the melting point temperature) of LaB_6 - MeB_2 system, values of which are in good agreement with experiment [33, 36].

Further progress of this work consists in investigation of physic-mechanical properties of LaB_6 - MeB_2 systems under extreme conditions (high temperature and deformation). Taking into account complexity of the formulated problem, we approach its solution on stage-by-stage basis:

1. Calculation of mechanical characteristics of components constituting the composite. For calculation of these characteristics for investigated LaB_6-MeB_2 systems under uniaxial deformations, we use the rule of mixtures [37-40] as a first approximation.

2. The problem of calculation of thermal expansion coefficients of composites with eutectic composition becomes even more acute when these materials are considered for use under extreme operational conditions. Difference in thermal expansion coefficients of components leads to emergence of internal stresses, neglect of which makes control of mechanical properties less effective. This reduces range of application of such materials. That is why preliminary estimate of such significant material characteristic as thermal expansion coefficient, especially in absence of both experimental and theoretical data for this parameter [41], is expedient.

3. To find dependence of mechanical characteristics (deformation, elasticity modulus, theoretical strength) from temperature, one has to know energy of electron-ion system of materials at different temperatures. In pseudopotential method this means necessity to determine volume change of elementary cell of borides at temperatures different from zero, that is obtain explicit dependence of full energy of the system from lattice parameters in a given interval of temperatures. For this, we use a physical model developed to calculate thermal

expansion coefficient, and obtain the dependence of lattice parameters (volume) from temperature [42].

4. On the basis of a computational experiment, a model of the formation of interphase boundaries in the quasi-binary eutectic systems is proposed. The values of the energy of the interface between the components in the boride and metal-ceramic quasi-binary composites with eutectic composition were calculated. The values of the energy of the interface at different temperatures for LaB_6-TiB_2, LaB_6-ZrB_2 systems [43] were estimated.

5. Calculation of the mechanical characteristics of quasi-binary eutectic composites with account of inter-component interaction at the interface between components [44].

Calculation of theoretical strength and Young's modulus of MeB₂ (Me - Ti, Zr) borides, LaB₆ composites with eutectic composition in LaB₆-MeB₂ systems

To calculate mechanical characteristics of the material on the micro level the value of the total energy per atom (molecule) of the material is used [33].

Energy (at constant volume of the molecule) is a sum of the electrostatic energy and the energy of band structure, which can be represented as a sum of paired intermolecular potentials. The change in energy along the lattice parameter (or its projection) parallel to the axis of deformation is directly proportional to the theoretical strength of the material. Under uniaxial deformation along the z-axis strength is determined through the energy of the electron-ion system (U) per unit area of atomic plane in the unit cell, located perpendicular to the axis of deformation [45]

$$\sigma_z = (\partial U/\partial e_z)/(S \cdot d), \qquad (49)$$

where S – surface of atomic plane in atomic cell, e_z – relative deformation, d – lattice parameter or its projection parallel to deformation axis.

At very small strains stress-strain curve is close to linear law and then:

$$\sigma = E \cdot \Delta d / d_0. \tag{50}$$

In the case of composites for calculation of Young's modulus it is necessary to make some simplifications. Assume that the reinforcing phase (fibers or plates) is distributed homogeneously and its basic structural elements are parallel to each other throughout the matrix. In most cases, elastic modulus of the composite material can be calculated by the rule of mixtures. However, to use this it is necessary to clarify the type of loading. Consider the homogeneous strain state when the reinforcer is located along the direction of the load. Then, for the first stage (region) of deformation, where the matrix and the reinforcer deform elastically, for the theoretical strength of the composite it can be written [46]

$$\sigma_K = \delta_A \sigma_A + \delta_B \sigma_B = E_A \varepsilon_A \delta_A + E_B \varepsilon_B \delta_B \tag{51}$$

where σ_A - stress in the matrix at fiber fracture strain, σ_B – strength limit of fibers under tension; δ_A, δ_B - volume fraction of components (Table 6), $\varepsilon_A, \varepsilon_B$ - deformations.

Table 6. Volume fraction of components in composite

Система	δ_A	δ_B
LaB$_6$ - TiB$_2$	0.893	0.107
LaB$_6$ - ZrB$_2$	0.837	0.163
LaB$_6$ - HfB$_2$	0.873	0.126

The dependence of stress from strain for components obtained by the formula (49) are shown in Figure 39. Less ductile are MeB$_2$, maximum deformation for these diborides is about 0.1, while for LaB$_6$-0.16. TiB$_2$ has greater strength compared with ZrB$_2$ and HfB$_2$ diborides, strength values of which are almost identic.

The strength of the eutectic composite with brittle hardening phase, oriented along the axis of tension (Fig. 40) can be obtained by substituting in (51) $\varepsilon_A = \varepsilon_B = \varepsilon_{\max}$, where ε_{max} - maximum strain of fragile phase in tension. It is believed that the fracture of the composition occurs as a result of simultaneous fracture of equally strong fibers in one section when the maximum deformation ε_{max} is reached. As TiB_2, ZrB_2 and HfB_2 deform almost elastically, then the use of mixture rule for system LaB_6-MeB_2 when calculating mechanical characteristics is an acceptable approximation.

The results of computational experiment to determine elastic moduli of the components and composite for investigated systems by the formulas (49-51) are presented in tabular form.

Table 7. The elastic moduli of the components and composite materials in the system LaB_6-MeB_2 and their experimental value in GPa

Phase	E (calc.)	E (exp.)	
LaB_6	505.27	478.73 [47]	320[*]
TiB_2	608.84	540.53 [47]	545[*]
HfB_2	523.97	479.71 [47]	
ZrB_2	534.67	495.80 [47]	430[*]
LaB_6-TiB_2	516.11	-	
LaB_6-HfB_2	507.63	-	
LaB_6-ZrB_2	508.46	-	430-450[*]

(*Private communication A.B. Lyashchenko)

The obtained values of Young's modulus are close to their experimental values within acceptable limits (maximum relative error of ~ 7%), taking into account that in the calculations we considered only perfect single crystals, while real crystals always have lower values.
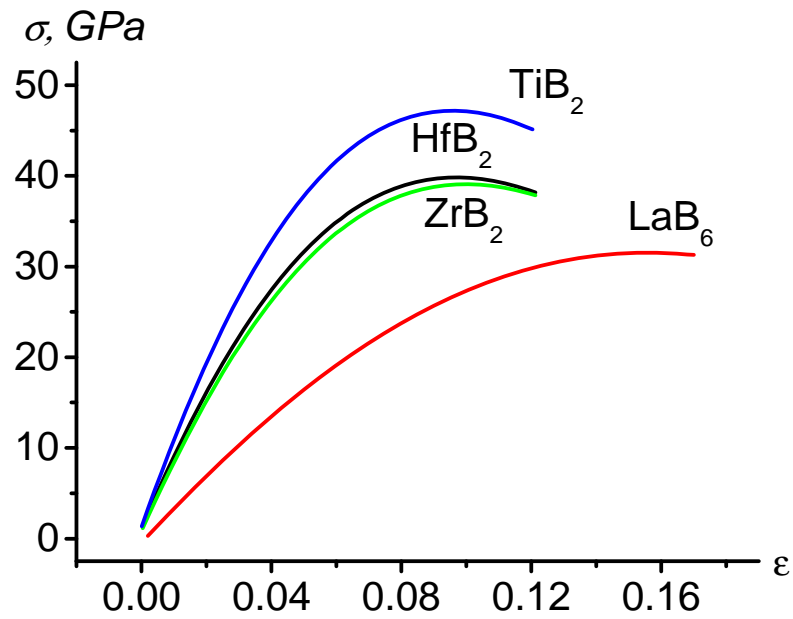
Fig. 39. Dependence of strength from strain for borides at $T = 0$ K
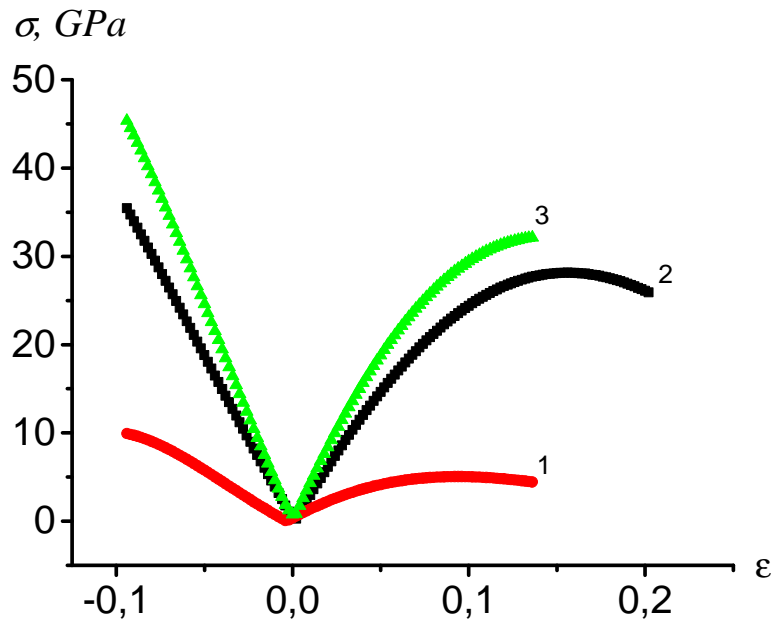

Fig.40. Dependence of theoretical strength (at T = 0 K) 1 - TiB_2 , 2 - LaB_6 and system 3 - $LaB_6 – TiB_2$ with eutectic composition, calculated by mixture rule taking into account their volumetric fraction from deformation.

Young's modulus and theoretical strength (Table 7) of borides of transition metals decreases with increasing atomic number of metals in the group similar to the case of experimental measurements of microhardness.

Note that the equations of "rule of mixtures" is adopted in the theory of artificial composites with fiber reinforcement (Kurz W., Sahm PR Gerichtet erstarrte eutektische werkstoffe - Springer-Verlag, Berlin / Heidelberg.- 1975. -p.- 272). It is assumed that the interaction between the phases is absent. This assumption is valid since in artificial composite sizes of particles of phase components are large, and bonding at interfaces is weak. On the contrary, eutectic phases exert significant influence on each other at the interface. Thus, the rule of mixtures in application to eutectic composites can be viewed as a first approximation. Hence, further, mathematical models are developed that can be used to calculate mechanical properties of quasi-binary composites taking into account interaction between phases at the interface.

Calculation of linear thermal expansion coefficients of MeB_2 (Me – Ti, Zr) borides, LaB_6 and eutectic composites in LaB_6–MeB_2 systems

The scatter of experimental data on the coefficients of thermal expansion for borides of transition metals for the same compounds sometimes can be as high as 70-100% [47]. This is due to he lack of sufficiently pure single crystals. The presence of a small percentage of impurities can greatly alter physical properties of the studied systems. In addition, while for borides (MeB_2, LaB_6) thermal expansion coefficients are experimentally determined, and this variation is established, then for LaB_6 - MeB_2 system published experimental data are not available. Therefore, calculation of thermal expansion coefficients for borides (MeB_2, LaB_6), as well as quasi-binary systems LaB_6-MeB_2 eutectic composition, based on first principles, is a matter of topical interest.

It should be noted that the method of preparing the samples, the phase composition, the presence of impurities and the measurement method have significant influence on the values of the physical characteristics of borides. Theoretical calculations consider ideal single crystals and it usually gives somewhat higher values of the calculated parameters compared with the experiment.

One of possible ways of calculating the coefficient of thermal expansion is a method based on determination of the dependence of crystal total energy on the lattice parameters at different temperatures.

The total energy of the crystalline material can be represented as the sum of the energies of the electron-ion system at $T = 0$, (T - absolute temperature) and the energy of the thermal vibrations of the ions at temperature $T \neq 0$. To calculate the energy of the electron-ion system at $T = 0$ we use the method of a priori pseudopotential [34]. The energy of the thermal vibrations of the investigated materials, which have complex structure, we calculate within the framework of Einstein's model [48], which gives reliable results in contrast to Debye model (that works quite well for simple crystal lattices [49] and leads to unstable computational schemes for complex structures).

The total energy of the electron-ion system at $T = 0$ within the framework of the pseudopotential method in the second-order of perturbation theory, can be written as [33]

$$U = U_0 + U_S, \qquad (52)$$

where U_0 depends on the volume of the unit cell. Energy U_0 includes kinetic, exchange-correlation energy and energy of a free electron gas, as well as corrections to the energy in the first order of perturbation theory with respect to pseudopotential. The second term (second-order correction) represents energy of band structure and electrostatic energy, and can be represented as a sum of pair interatomic potentials

$$U_S = \frac{1}{N} \sum_{i,j}{}' \Phi(R_i - R_j), \tag{53}$$

where $R_i - R_j$ - distance between atoms i and j, N - number of atoms in a representative volume [50]. The method of calculating the energy of the electron-ion system in the framework of the pseudopotential method is given in [33].

According to Einstein's model [48], atoms in the crystal lattice occillate with the same frequency, which is proportional to material stiffness. The average energy of the lattice vibrations is defined by [48]

$$U_T = \sum_q \frac{\hbar \omega_q}{\exp(\hbar \omega_q / kT) - 1}, \tag{54}$$

where summation is done over all types of vibrations, and ω_q - oscillation frequency (according to Einstein model $\omega_q = \omega$ for all q). In the case of the structure with n atoms in a unit cell, there are $3Nn$ oscillations (N - number of cells in the material volume) and the oscillation frequency is determined by the relation

$$\omega = \sqrt{2\alpha^* / M}. \tag{55}$$

Here α^* - force constant, which is determined by the second derivative of the energy of interatomic interaction with respect to space variable

$$\alpha^* = \left(\frac{\partial^2 U}{\partial r^2} \right). \tag{56}$$

Pair interatomic potentials (53) for the investigated materials were constructed in [33].

In calculating the energy of the electron-ion system in the second-order of perturbation theory with respect to the pseudopotential, we use harmonic approximation. However the application of this approximation in the lattice

dynamics is not sufficient for calculation of the coefficient of thermal expansion from the "first principles". At the same time, we know that the calculation of the vibrational part of corresponding thermodynamic functions taking into account anharmonicity is hopelessly complex [51]. This difficulty can be avoided if we make simplifying assumptions about the dependence of the oscillation frequencies on temperature and volume using the "quasi-harmonic" approximation [51]. In this approach, we first calculate force constants at $T = 0$. The energy of thermal vibrations (54), calculated at low temperatures ($T_1 = \Delta T; \quad \Delta T \to 0$) and force constants α_0^* at $T = 0$ is added to the value of the energy U. At the subsequent steps in the calculation of the total energy within the harmonic approximation, we use new power constants, and, therefore, frequencies dependent on volume.

Schematically, the solution of the formulated problem can be presented as follows:

- From the minimum of the energy of the electron-ion system $U(a,c)$ lattice parameters (a_0, c_0) and force constants in the equilibrium state of the crystal are determined.

- Full energy $U^* = U_0 + U_T$ of the system at the temperature $T \neq 0$ is calculated.

- From the equation $U_{min}^*(a_0,c_0,T) = U(a_1,c_1)$ new values of lattice parameters are found.

- From formula (56), at the obtained values of lattice parameters, the new values of the force constants are calculated.

As a result, we obtain the dependence of lattice parameters from temperature.

Coefficient of linear thermal expansion α_i is determined from the relation [30]

$$\alpha_i = \frac{\Delta a_i}{a_i} \cdot \frac{1}{T} \tag{57}$$

(a_i – lattice parameter, Δa_i - change of the lattice parameter at the temperature T).

For LaB_6 with cubic structure lattice parameter is $a_i = a$, and for hexagonal MeB_2 $a_i = (a; c)$.

Fig. 41-43 shows the temperature dependence of relative elongation, and Tables 8 and 9 - corresponding values of the coefficients of thermal expansion for the materials studied.

Values of α_a are almost constant in the whole range of temperatures studied for ZrB_2, and in the case of TiB_2 — monotonously increase up to temperature of 1000 K and then stabilize. Coefficient of thermal expansion of LaB_6 (Table 6) has a jump in the temperature range from 750 K to 1000 K. This interesting result has quite simple physical sense. The basis for the calculation of the physical characteristics of crystals from first principles is the type of crystal potential. This potential is used for construction of unit cell of the crystal under study from corresponding atoms, cell type is determined based on the minimum energy of electron-ion system, as well as the parameters of the crystal lattice. According to the results of calculations, the energy of interaction of boron atoms (complex B_6) in the structure of LaB_6 has a deeper minimum than the energy of interaction between atoms of La and B, or atoms of La-La. Therefore, in the initial stage of raising the temperature to 750 K it is La atoms that are displaced from the equilibrium position. At higher temperatures B_6 volume complex begins to participate in the expansion, which leads to a jump in the coefficient of thermal expansion.

Table 8. Coefficients of thermal expansion α_a (in K^{-1} units) for TiB_2, ZrB_2, LaB_6 and their averaged experimental values [47] (in brackets)

T, K	α_a (TiB_2) (4.5). K^{-1}	α_a (ZrB_2) (5.9). K^{-1}	α_c (LaB_6) (6.4±0.5). K^{-1}
300	5.503	6.144	7.597
500	5.540	6.144	7.597
750	5.590	6.147	7.597
1000	5.70	6.145	7.850
1500	5.655	6.147	7.851
2000	5.701	6.149	7.850
2500	5.699	6.146	7.850
2750	5.762	6.145	7.801

In contrast to the cubic LaB_6, transition metal diborides have chracteristic hexagonal structure, so the task is set of calculation of the coefficient of thermal expansion also in the direction perpendicular to the basal plane (direction c). To calculate the coefficient of thermal expansion in the direction of c, we propose to use the energy of interaction between the basal planes, whose value for the systems studied is calculated in [38]. At high temperatures, the distance between the basal planes increases, which leads to a change in the interaction energy between the planes.

Table 9 Coefficients of thermal expansion α_c for TiB_2 and ZrB_2, in brackets their averaged experimental values are given [47].

T, K	$\alpha_c \cdot 10^6 K^{-1}$ (TiB_2) (8.65-11.20)	$\alpha_c \cdot 10^6 K^{-1}$ (ZrB_2) (6.78-7.65)
300	10.231	7.589
500	10.276	7.589
750	10.472	7.659
1000	10.706	7.750
1500	10.840	7.808
2000	11.072	7.790
2500	10.894	7.684
2750	10.267	7.313
3000	10.012	7.083

Typically, the components of the composition (the matrix and the reinforcer) have different coefficients of thermal expansion. Approximately linear expansion coefficient of the composite is determined by the relation [52]

$$\alpha_k = (\alpha_A E_{A1} \cdot \delta_A + \alpha_B E_B \cdot \delta_B) / \overline{E} , \qquad (58)$$

where E_A and E_B are Young moduli of components, and $\overline{E}$ – average modulus for composition

$$\overline{E} = \delta_A E_A + \delta_B E_B . \qquad (59)$$

Young's moduli are determined through the stress tensor [53].

The coefficient of thermal expansion of the composite in a direction **a** is calculated by the formula [52]

$$\alpha_a = \alpha_A \cdot \delta_A + \alpha_B \cdot \delta_B . \qquad (60)$$

Given that the composites have a fiber structure and fiber diameter is much less than its length, formula (60) was applied [52]. On the other hand thermal coefficient for direction c was also calculated by the (60). The results showed that the coefficients calculated by the formulas (56) and (60) do not differ much from each other.

The calculation results for the composites are presented graphically:

1) relative elongation of the composite with eutectic composition in the direction perpendicular to the solidification front (Figure 41) (direction c of the hexagonal lattice);

2) dependence of the thermal expansion coefficient from temperature (Fig. 42).

Results of computational experiment on the Ab-initio calculation of the coefficient of thermal expansion of boride-boride eutectic composites show [41]:

- Investigated composites have pronounced anisotropy of properties, thermal expansion coefficients α_a and α_c are very different from each other.

- In the temperature range $750\ K \leq T \leq 1100\ K$ thermal expansion coefficients α_a and α_c for the studied composites LaB_6-MeB_2 change abruptly, due to abrupt change in CTE of LaB_6.

- The average values of the thermal expansion coefficients α_a for composites and LaB_6-TiB_2 are almost identical, and α_c for LaB_6-ZrB_2 over the entire range of temperature is higher than that for LaB_6-TiB_2.

- The coefficients of thermal expansion (α_a and α_c) for TiB_2 and ZrB_2, as well as for LaB_6 are calculated with the help of the proposed model using a priori pseudopotential method, and are within the scatter of experimental data.
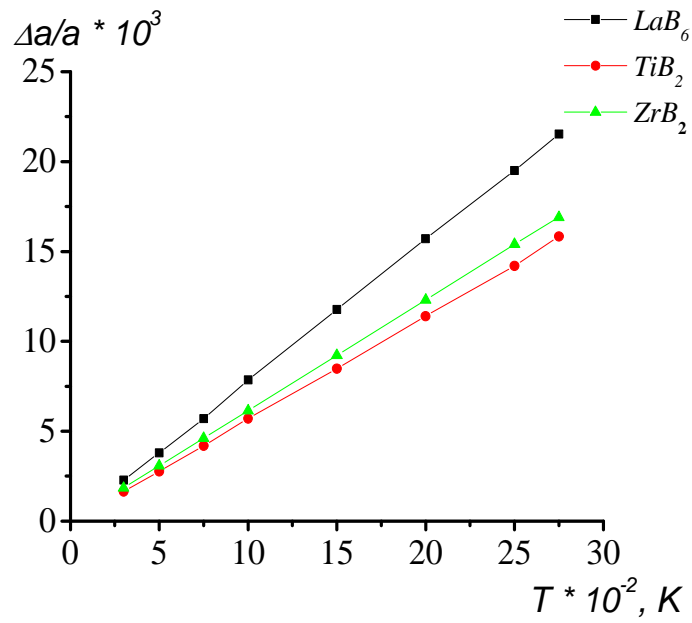
Fig. 41. Temperature dependence of the relative elongation along a (for MeB_2 a – parameter of the basal plane)
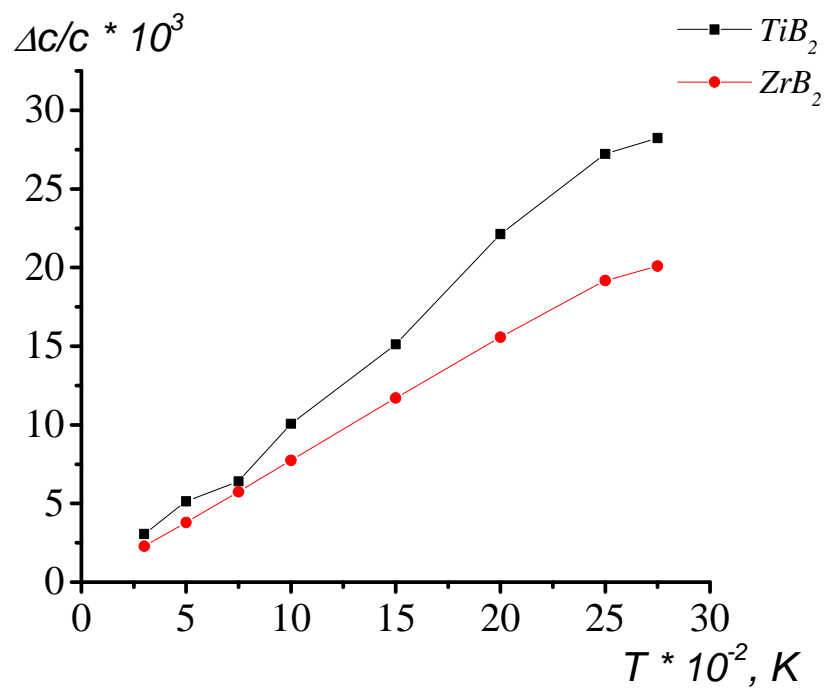

Fig.42. Temperature dependence of the relative elongation in the direction perpendicular to the basal planes for components with a hexagonal lattice.
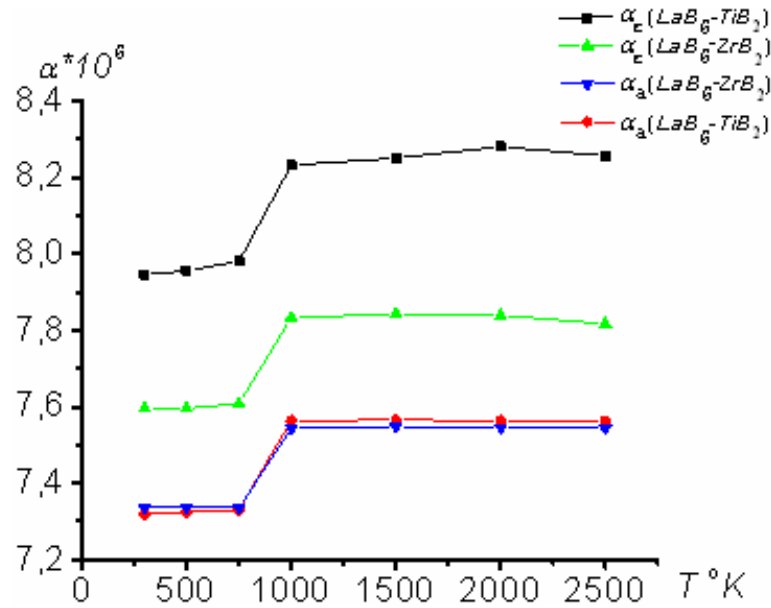
Fig. 43. Dependence of the thermal expansion coefficients α_a and α_c on the temperature of composites with eutectic composition.

Since LaB_6 has a structure of CaB_6 type (simple cube of metal atoms centered by octahedron of boron atoms), its thermal properties in the direction *a* or *c* are identical. The anisotropy of the thermal coefficient of the composite is connected with the second components MeB_2. Diborides of transition metals have a hexagonal structure of AlB_2 type, in which boron atoms form graphite-like grids perpendicular to the axis Z, and the entire structure – is a consequent alternation of hexagonal layers of metal atoms arranged in a hexagonal close-packed lattice sites with a small *c/a* ratio and layers of boron atoms forming a hexagonal two-dimensional grid. According to calculations, lattice parameters of TiB_2 and ZrB_2 are $a = 3.05$ Å; $c = 3.24$ Å and $a = 3.12$ Å; $c = 3.49$ Å [33]. On the basal plane lattice parameters for two diborides are close in value, which can not be said about the parameters in the direction perpendicular to the basal plane. Physical-mechanical properties of materials, including thermal, are based on the interatomic interactions, and the latter depend on the interatomic distances. This fact is reflected in the results of the calculations, which supports the adequacy of the

models chosen. The composition of LaB_6-ZrB_2 and LaB_6-TiB_2 composites contain 70% and 75% of LaB_6, respectively, and, hence, their characteristics calculated by the formulas (58) mainly reflect the thermal properties of this component. Therefore, in the same temperature range from 750 K to 1000 K, the abrupt increase in the coefficient of thermal expansion of these composites is observed.

The values of the coefficients of thermal expansion of LaB_6-ZrB_2 and LaB_6-TiB_2 composites obtained using formulas (58 - 60) are less accurate compared with similar calculations for the components, as in the case of composites at this stage the influence of the contact borders of the two components is not taken into account.

Temperature dependence of the theoretical strength of borides and quasibinary boride eutectic systems

With increasing temperature, the level of mechanical properties that characterize strength of the material decreases and the level of plastic properties — increases. Many of the materials at elevated temperatures undergo physico-chemical transformations (precipitation of hardening phases, coagulation and dissolution of phases, oxidation, especially of grain boundaries, etc.). Depending on the nature of these transitions noticeable deviations in the temperature curves of strength and ductility can be observed, as well as change in the character of fracture.

Physical properties that determine material characteristics at high temperatures are energy of interatomic bonding and melting point temperature of compounds. Therefore, the alloys based on refractory metals weaken less with temperature than the alloys having low melting point and energy of bonding forces.

One of the main requirements for the composites, the end product made from which are used in extreme conditions — in internal combustion engines, gas

pipes, aircraft jet engines — it is their performance at high temperatures. This is what explains the interest to the study of variation in the mechanical properties of composites as a function of operational temperature. Effect of high temperature on the mechanical properties of eutectic boride and ceramic composites and functional materials is presented in the work by S.S. Ordanyan et al. [30]. It investigated the temperature dependence of the bending strength for metal-ceramic and boride systems and showed that in the studied systems of eutectic composition high strength is retained at temperatures up to 0.8 times the eutectic temperature (T_{ev}).

Dependence of the mechanical properties (microhardness, flexural strength) on the temperature in the range from 25 to 1600 °C have been studied in [31, 32, 54] for LaB_6, TiB_2 and LaB_6-TiB_2 system, where it is assumed that the flexural strength in the directionally reinforced LaB_6-TiB_2 composite at high temperatures, mainly depends on the ductility of the LaB_6 matrix and TiB_2, which is a rather obvious fact. This is a consequence of the formula that determines the strength of the system by the rule of mixtures, where the decisive role is played by the maximum strain of diborides.

From the works on computational experiments related to the study of borides, one may point out [55], where with the use of density functional theory, TiB_2 bulk modulus was calculated and the compound was classified as a superhard material (bulk modulus of about 260 GPa). In [56], on the basis of the Hartree-Fock method and density functional theory, anisotropic elastic constants for TiB_2 were calculated. However, these studies did not consider the dependence of mechanical properties on the temperature for transition metal borides, and especially for LaB_6-MeB_2 systems. This is due to the complexity of the calculation of thermal energy of the system. With increasing temperature, the thermal vibrations of the atoms are not subject to the harmonic approximation. Accounting for non-harmonic members is a rather difficult task in the framework of quantum-mechanical calculations, still a question of dependency of the mechanical characteristics on the temperature remains relevant.

In [41], where the calculation of the linear coefficient of thermal expansion (LCTE) of borides from ab initio methods was done, the dependence of LCTE on the temperature was revealed, that is a purely quantum-mechanical effect. The model developed in [41] using quasi-harmonic approximation makes it possible within the framework of quantum-mechanical calculations to study the influence of temperature on the tensile strength of borides and boride-boride eutectic systems.

To identify the dependence of mechanical characteristics on temperature, it is necessary to be able to calculate the energy of the electron-ion system of the materials at different temperatures. Within the framework of the pseudopotential method it means to find the change of volume of the unit cells of borides at temperatures different from zero, i.e., obtain the explicit dependence of the total energy from the lattice parameters or volume at nonzero temperature.

To solve this problem it is necessary:

- From the minimum energy of the electron-ion system $U(\Omega)$ determine the volume of the lattice (Ω) in the equilibrium state of the crystal.

- Calculate the total energy of the system $U^* = U_0 + U_T$ at nonzero temperatures ($T \neq 0$).

- From equation $U^*_{min}(\Omega_0, T) = U(\Omega_1)$ determine the new values of the volume of the crystal lattice.

Finally, we obtain dependence of the volume from the temperature.

The procedure for the calculation of the energy of the electron-ion system in the framework of the pseudopotential method is given in [33, 56 - 58]. The results of computational experiment to determine the dependence of the volume of the unit cells from the temperature are presented in tabular form (Table 10).

Table 1.5. Calculated values of the volume of the unit cells of investigated borides depending on the temperature

T, K	$\Omega\,(TiB_2)$	$\Omega\,(ZrB_2)$	$\Omega\,(LaB_6)$
0	173.238	207.810	483.770
300	174.108	209.054	487.219
500	174.696	209.782	489.541
750	175.432	210.692	492.444
1000	176.168	211.602	495.346
1500	177.640	213.421	501.151
2000	179.113	215.241	506.956
2500	180.585	217.061	512.761
2750	181.347	217.987	515.663

Under uniaxial deformation along the z axis theoretical strength is determined by the energy of the electron-ion system U per unit area of atomic plane in the unit cell perpendicular to the axis of deformation

$$\sigma_z = \frac{1}{c} \cdot \frac{\partial U}{\partial e_z},\tag{61}$$

where e_z - relative deformation, c - lattice parameter or its projection parallel to the axis of deformation. For each value of the volume (corresponding to a given temperature) the energy of the electron-ion system is calculated. Theoretical strength is calculated with formula (61) by standard methods [39]. As a result, the computational experiment found that at temperatures close to 2000 K the value of the absolute deformation for diborides is increased by ~ 20% compared to the same value at zero temperature.

Below are tabulated results of computational experiment on the calculation of the theoretical strength for TiB_2 and LaB_6, and for composite based on them. Values for composite are calculated using the rule of "mixtures", where the

theoretical strength of the system is a sum of the theoretical strengths of components taking into account their volume fractions

$$\sigma_{KZ} = \delta_A \cdot \sigma_A + \delta_B \cdot \sigma_B^{max}.$$

(62)

Here σ_B^{max} – maximum strength of MeB_2, σ_A – strength of LaB_6 at maximum deformation of MeB_2.

In Table 11 strength σ_A (at $T = 0$) corresponds to the strength of LaB_6 at deformation of the crystal up to about 0.1, which represents the ultimate strain for MeB_2 (Me - Ti, Zr, Hf), when strength of diborides reaches maximum values.

As a result of the calculation using the formulas (61, 62) of the theoretical strength of the components and composite at different temperatures, the dependence on the temperature of the theoretical strength under uniaxial tension for LaB_6, TiB_2, as well as LaB_6-TiB2 system was obtained. The results of these calculations are presented in Table 11 and in Fig. 44 - 46.

Table 11. Temperature dependence of the theoretical strength (GPa) of LaB_6, TiB_2, as well as LaB_6-TiB_2 composite.

T, K	σ_A	σ_B^{max}	σ_k
0	30.083	47.180	31.910
300	29.635	46.804	31.471
500	29.328	46.639	31.180
750	28.950	46.271	30.803
1000	28.610	45.899	30.460
1500	27.904	45.230	29.758
2000	27.461	44.549	29.290
2500	26.503	43.672	28.340
2750	26.203	43.250	28.027

Theoretical strength of LaB_6 changes almost smoothly with the temperature except the temperature range 1300 K $< T <$ 2200 K, where there is an abnormal part

of dependence. In the case of TiB2 such interval is absent. The appearance of anomalies in the plot of the theoretical strength from the temperature is characteristic for LaB_6, and it affects such dependence of a composite LaB_6-TiB_2, where LaB_6 content is 75% (mol.) of the composite.

It should be noted that up to the melting temperature borides (TiB_2, ZrB_2, HfB_2) and composites based on them have high strength, and it is confirmed experimentally by S. Ordanyan [30].

If the crystal is subjected to deformation with simultaneous raising of the temperature, then concurrently with deformation a mechanism of thermal expansion will also operate. Quantum mechanical calculations show that the interaction (binding) between the boron atoms is much stronger than that between metal and boron, and even more than the bond of metal to metal [37 - 39], ie, to expand B_6 complex it requires higher temperatures. With thermal expansion and simultaneous stretching in LaB_6 there is a change of the relative distance between the atoms constituting the crystal, which in turn changes the characteristic temperature range where there is an abrupt change of LCTE. At temperatures $T > 1300$ K the expansion of B_6 complex in the plane [200] resists to the uniaxial strain (stretching) of the complex along the perpendicular direction, with the result that there is a bump on the plot "theoretical strength – temperature".

The energy of the electron-ion system (per volume of the unit cell) is a function of the crystal temperature. With increasing temperature, energy increases, and the maximum strength decreases. We introduce the concept of rate of strength change with temperature

$$\sigma_{Z,T} = \frac{\partial \sigma_Z}{\partial T} \ .$$
(63)

The nature of the dependence of $\sigma_{z,T}$ on deformation is same for both LaB_6 and MeB_2 (the difference is only in parameters – deformations and the corresponding strength) (Fig. 47).

On the interval (300 K $< T <$ 1300 K) $\sigma_{Z,T}$ decreases rapidly, while transition to higher temperatures ($T >$ 1300 K) change in deformation does not change $\sigma_{Z,T}$.
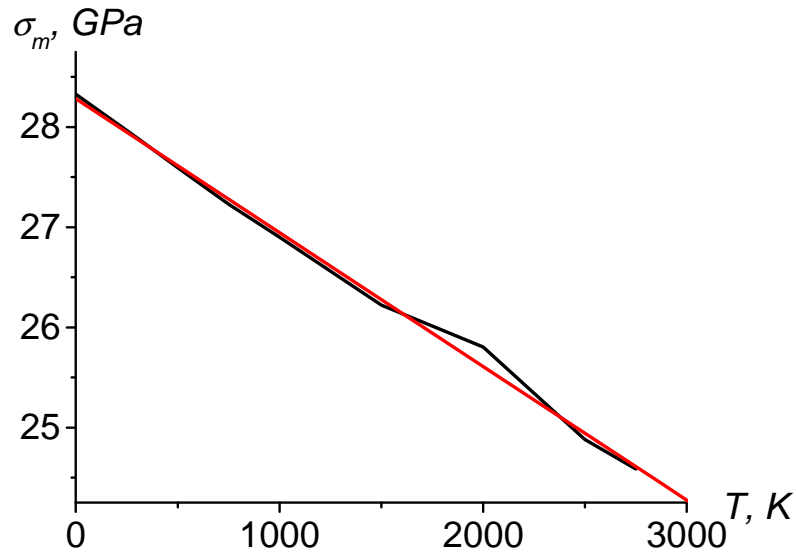

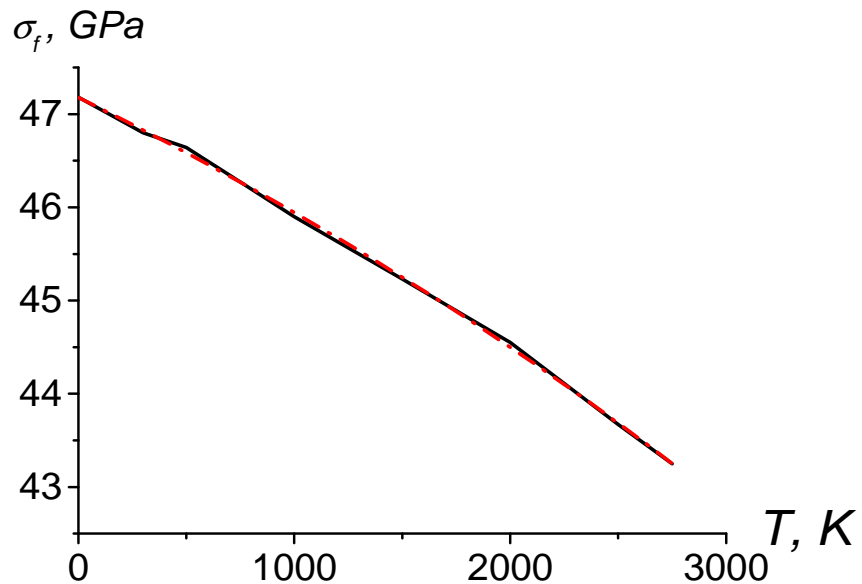Fig. 44. Dependence of theoretical strength of LaB_6 from temperature at uniaxial deformation (tension).

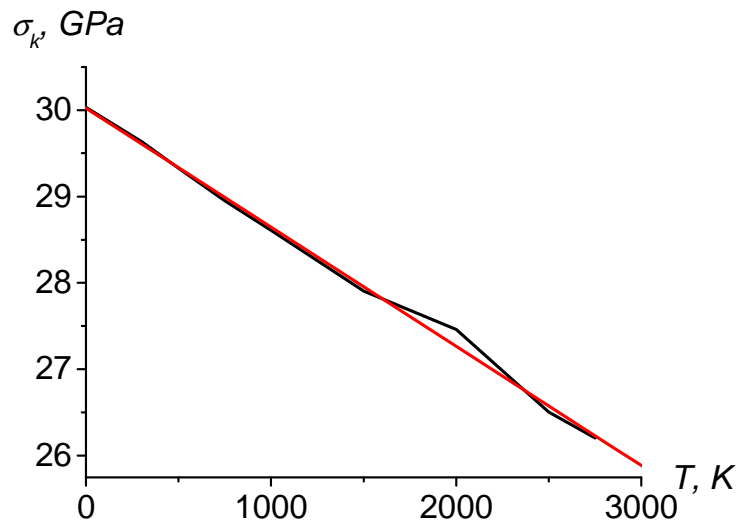Fig.45. Dependence of theoretical strength of TiB_2 from temperature at uniaxial deformation (tension).

Fig. 46. Dependence of theoretical strength of LaB_6 - TiB_2 composite from temperature at uniaxial deformation (tension).
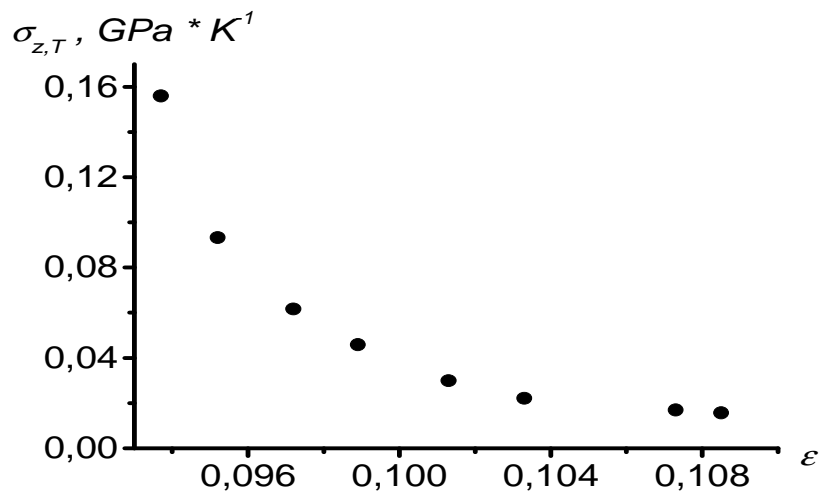
Fig. 47. Dependence of strength change rate with temperature from deformation at uniaxial tension for TiB_2.

Theoretical strength of boride-boride composites and their constituent parts varies exponentially as a function of temperature. In the temperature interval (1300 K $< T <$ 2200 K) for LaB_6 and LaB_6-TiB_2 composite the observed deviation in the dependence "theoretical strength – temperature" is a consequence of changes in the coefficients of thermal expansion of the components in the system.

Intercomponent boundaries and energy of the components interface in quasi-binary eutectic systems

A study of interatomic interactions at the interface of eutectic phases was performed in [59, 60]. It has been established that the energy states of atoms in the boundary layers and volume of eutectic phases differ considerably, and its own interatomic bonds in these layers are also changed. These data confirm that the eutectic does not represent a mechanical mixture of phases, but a system of interacting phases. Regular mutual orientation of eutectic phases is associated with the condition of minimum interfacial energy. The minimum of interfacial energy is achieved when the combination of symmetry, orientation and crystal lattice parameters of the two crystals corresponds to the condition of the largest number of atomic coincidences [61].

Under the surface section we understand a transition zone which separates from each other two phases, or (in the case of grain boundaries), two crystals of the same phase [46].

Eutectic solidified under normal conditions, has a surface area of approximately 1 m^2 per 1 cm^3 of material [46]. Extremely large interfacial area, which arose in the process of crystallization, is a characteristic feature of eutectic compositions and determines their special properties.

To determine the characteristics of the interfaces different theories are used: 1) macroscopic, such as thermodynamics, allowing us to obtain the averaged data of the interface; 2) atomic, where the atoms are considered as spheres with a short-range (central) forces that allow to draw conclusions about the structure of the interface (to build geometric and energy models); 3) electronic, which give quantum-mechanical description of the interaction between the atoms at the interface in the eutectic [46, 62].

A comprehensive description of all of the observed surface phenomena in eutectic composites at the interface is currently not available. Therefore, to provide

a general overview of this issue is difficult. Furthermore, most studies address grain boundaries or external surfaces [46, 62]; phase boundaries, so important for the eutectic materials are just beginning to attract the attention of researchers. As the authors of [62] note, the experimental data for heterogeneous interface are not available. For this reason, the description of the interaction between the atoms of the interface is a complex task, especially between two dissimilar phases.

The interface between the two phases can be non-coherent or coherent locally. The authors of [63, 64] for the solution of this problem present coherent local areas as "cells". For a complete description of the real interface, the notion of "supercell" composed of the crystal lattices of the two phases is introduced.

Based on the results of calculations from first principles [37, 38] for metal-ceramic composites for calculation of the energy of the electron-ion system of components and composite as a whole, a model was created to describe the formation of intercomponent borders in the quasi-binary eutectic systems.

In the system LaB_6-MeB_2 at the border of coupling of two components the binding is achieved with the help of boron atoms belonging to two components. In the case of LaB_6-TiB_2 composite with eutectic composition, there is 0.75 part of LaB_6 molecule and 0.25 part of TiB_2 molecule at the interface. For all of the system as a whole the number of boron atoms, which are common for two components at the border, is 5. Due to common atoms, the boundary is strong enough. The total number of these common atoms depends on the lattice parameters of the components. For TiB_2, ZrB_2 and HfB_2 these parameters are very close, and so, respectively, energies of the contact are nearly identical, which is not the case for VB_2 and CrB_2. Here, because of the small parameter (c), the degree of possible coupling of two components increases as increases the probability of coincidence of atomic planes [002], [004] LaB_6 and [002] MeB_2, and this leads to an increase in energy of the contact. The confirmation of these statements is obtained from the results of calculations.

Based on the fact that the interface is associated with the energy of interaction between the molecules (atoms) of two phases, the surface energy associated with the interface of two phases is excess internal energy of the composite compared to the energy of the components. The energy of the phases (components) and the system based on them are calculated using the pseudopotential method [33, 41].

The energy of components calculated per one molecule, in the framework of the pseudopotential method is obtained by adding the pair intermolecular interactions, which are determined by the formula [50]

$$\Phi(r) = U_{ec} + \frac{\Omega}{\pi^2} \int_0^\infty \Phi(q) \frac{1}{r} \sin(qr) q \, dq \ , \qquad (64)$$

where U_{ec} – electrostatic energy, and $\Phi(q)$ — characteristic function

$$\Phi(\vec{q}) = V^2(q) \chi(q) \varepsilon(q) \ .$$

Here $V(q)$ – pseudopotential of the system (molecule) [33], $\varepsilon(q)$ and $\chi(q)$ – describe screening and correlation of free electrons in the systems under study [50], and Ω - volume per molecule. Calculation of the energy component was carried out under the scheme [33], namely, the total energy of the two non-interacting components A and B is given by

$$U_1 = (C^2 \cdot U_{AA} + C \cdot U_A) + ((1-C)^2 \cdot U_{BB} + C \cdot U_B) \ , \qquad (65)$$

where U_A, U_B include kinetic energy of free electron gas, exchange-correlation effects, energy of electrons in the first-order perturbation theory by the pseudopotential for the corresponding molecules [33]; U_{AA} ; U_{BB} – energy of interaction between A-A and B-B, C – concentration of A component.

Energy of the system (A-B), which takes into account interaction between the components A and B (U_{AB}) can be written as

$$U_2 = C^2 \cdot U_{AA} + C \cdot U_A + (1-C)^2 \cdot U_{BB} + C \cdot U_B + 2 \cdot C \cdot (1-C) \cdot U_{AB}. \qquad (66)$$

Ultimately, the excess energy, which determines the surface factor, is

$$\Delta U = U_1 - U_2 = -2 \cdot C \cdot (1-C) \cdot U_{AB}. \qquad (67)$$

The energy of interaction between the two components (U_{AB}) can be represented as the sum of paired intermolecular potentials $\Phi_{AB}(\vec{R}_{lj})$

$$U_{AB} = \frac{1}{N} \sum_{l,j} \Phi_{AB}(\vec{R}_{lj}), \qquad (68)$$

where $\vec{R}_{lj} = \vec{R}_i(A) - \vec{R}_j(B)$ – distance between the molecules $i - j$ belonging to the components A and B. Since the energy of interaction between two molecules does not depend on the position of other molecules, and is only a function of k_F (Fermi momentum) or Z/Ω [50], it is possible to introduce the concept of "virtual" cell with a volume

$$\Omega = C \cdot \Omega_A + (1-C) \cdot \Omega_B \qquad (69)$$

and with a charge

$$Z = C \cdot Z_A + (1-C) \cdot Z_B, \qquad (70)$$

where $\Omega_i (i = A; B)$ – component volumes, Z_A; Z_B – respectively, number of their outer electrons. Pseudopotential of the virtual crystal will be equal to $V_V = C \cdot V_A + (1-C) \cdot V_B$. We are using the approximation that does not take into account variations $V_A - V_V$; $V_B - V_V$ in the nodes of the unit cell. Under this approach the characteristic function of the virtual crystal will be

$$\Phi_{bs}^V(q) = (V_V(q))^2 \cdot \chi_V(q) \varepsilon_V(q). \qquad (71)$$

Functions $\varepsilon_V(q)$ and $\chi_V(q)$ appearing here describe screening and correlation of electrons for the virtual crystal and are determined through the unit cell volume and the number of free electrons.

Interaction between molecules A and B is described by the function

$$\Phi_{AB}^{V}(R_V) = \frac{(\cdot Z_A + \cdot Z_B)^2}{R_V} + \frac{2\Omega_V}{(2\pi)^3}\int \Phi_{bs}^{V}(q)\cdot\exp(i\vec{q}\vec{R}_V)\,d\overline{q}\,, \qquad (72)$$

where R_V – intermolecula distance in virtual crystal.

In LaB$_6$-MeB$_2$ (Me – Ti, Zr, Hf) systems with eutectic content the content of diborides constitutes a small percent. We assign virtual crystal a cubic lattice. Such unit cell contains a single molecule, which consists of two parts - molecule of component A with a concentration C and molecule of component B with a concentration $(1 - C)$.
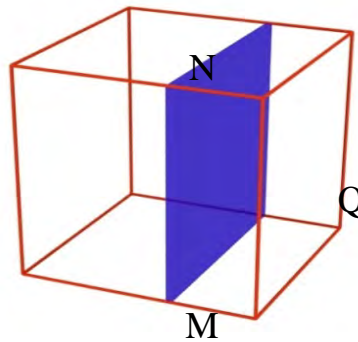

Fig. 48. In the unit cell of the virtual crystal the surface (MNPQ) is the interface between the two components

Figure 48 presents the cube (a unit cell of virtual crystal) and the surface of coupling of two components. The mean value of the contact surface area in a virtual cell can be determined if we represent $\Omega = A^3$ (virtual cell parameter $A = MQ$), and then coupling surface area

$$S = S_{MNPQ} = A^2\,. \qquad (73)$$

The surface energy of coupling of two components per unit area of contact will be

$$\gamma = -\,U_{AB}\,/\,S\,. \qquad (74)$$

Thus, the surface energy of the contact between two insoluble components will be

$$\gamma = -U_{AB}(R)\,/\,\Omega^{2/3}\,. \qquad (75)$$

At the boundary of coupling of two components in the model of "virtual" crystal, the unit cell is presented as averaged. It should be noted that in the quasi-binary eutectic systems two phases or two components (if they are insoluble) have different crystal lattice as well as sizes of atoms or molecules. Accounting for these effects in the calculation of the surface energy of interface between two components in the framework of quantum-mechanical calculations is quite challenging, so in the first approximation a facet of virtual cubic unit cell of the crystal is used as a coupling area (Fig. 48).

Table 12. Calculated volume (Ω), contact surface (S), energy of interaction between molecules (U_{AB}) and contact energy (γ) in the studied eutectic systems

System	Ω, a.u.	S, a.u.	U_{AB}, a.u.	γ, J/m^2
$LaB_6 - TiB_2$	406.107	54.84	0.12165	3.454
$LaB_6 - ZrB_2$	400.980	54.12	0.12420	3.582
$LaB_6 - HfB_2$	410.786	55.26	0.11965	3.388
$LaB_6 - VB_2$	290.155	43.83	0.22886	8.131
$LaB_6 - CrB_2$	338.530	48.57	0.22516	7.219
$B_4C - TiB_2$	576.077	69.24	0.80700	18.149
$B_4C - SiC$	517.210	64.50	0.77800	18.783
$TiB_2 - SiC$	151.326	28.97	1.58000	40.050

As can be seen from the obtained results (Table 12) contact surface energy in LaB_6-MeB_2 systems is small compared with the same energy in B_4C-TiB_2, B_4C-SiC, TiB_2–SiC systems. For LaB_6-MeB_2 (Me - Ti, Zr, Hf) systems contact energy of two components is so weak that can be ignored and the composite considered as a mechanical mixture, for LaB_6-VB_2 and LaB_6-CrB_2 systems contact energy is nearly 2-2.5 times higher. In other cases, such as SiC-B_4C binding at the boundary is realized through common carbon atoms. B_4C- TiB_2 system can have shared

boron atoms; also is possible formation of TiC here, but this is unlikely in the presence of a large number of boron atoms belonging to two components. In TiB$_2$-SiC system the bond between the components is achieved by means of the emergence of TiC clusters locally at the coupling boundary, and in this case the energy of the contact is sufficiently large, and this is confirmed by calculations.

The question arises — is it characteristic only of the eutectic composition, or not? One can definitely answer — no. For these systems (at least) the boundaries of with such structure will take place regardless of the composition. Only for eutectic composition, selected from the condition of extremum of thermodynamic function, contact boundary energy minimizes energy of the system.

Table 13. Calculated values of average volume and of contact surface energy at different temperatures in the case of virtual crystal approximation

	LaB$_6$–TiB$_2$		LaB$_6$–ZrB$_2$	
T, K	Ω, a.u.	γ, J/m^2	Ω, a.u.	γ, J/m^2
0	406.107	3.454	400.980	3.582
300	408.941	3.407	403.770	3.535
500	410.830	3.371	405.613	3.497
750	413.191	3.331	407.891	3.457
1000	415.670	3.290	410.222	3.416
1500	420.273	3.214	414.832	3.336
2000	424.955	3.139	419.440	3.271
2500	429.716	3.056	424.051	3.109
2750	435.011	3.010	428.360	3.106

Using the model proposed in [41] (for calculation of the energy of electron-ion system of the crystal in the second-order of perturbation theory with respect to pseudopotential with the account of expansion of the material at elevated

temperatures), the surface energy of contact was calculated depending on the temperature for the temperature range from zero to the eutectic. For each temperature the energy of interaction of components was obtained as well as the volume per one averaged molecule, and with the help of (81), (88) the energy of the contact surface at different temperatures was calculated. Results of computational experiment for LaB_6-TiB_2 and LaB_6-ZrB_2 systems are presented in Table 13.

With increasing temperature, the contact surface energy decreases, but the system retains its characteristic mechanical properties up to the melting temperature (eutectic temperature).

So, quasibinary eutectic is a system consisting of two almost insoluble components, bonded on at the boundary with the help of a) common atoms or b) compounds formed from atoms of the components.

The energy of the contact surface depends on ratio between the parameters of crystal lattices of components.

The proposed method can be used for calculation of the contact surface energy for any composite, provided components are insoluble.

Accounting for the effects of intercomponent boundaries in LaB_6-MeB_2 (Me - Ti, Zr, Hf) systems in the calculation of the mechanical properties

The idea of a eutectic as a simple mechanical mixture of fine crystals, gave reason to believe that mechanical and some other properties of alloys related by composition to the two-phase region of eutectic systems should change additively with the concentration. According to the well-known scheme proposed by N.S. Kurnakov and S.F. Zhemchzhnyi, a straight line should represent the isotherm "structure-mechanical properties" of these alloys, the eutectic point for such isotherm does not stand out in any way. However, many experimental data

contradict this scheme. The common rule is the nonlinear dependence of the mechanical properties from the composition of the two-phase alloy, and the additivity may occur only under certain conditions.

In [59, 60, 65] a number of studies of interatomic interactions at the interface of eutectic phases was carried out. It was established that the energy states of the atoms in the boundary layers and in the volume of eutectic phases differ considerably, and its own interatomic bonds in these layers are altered. These data confirm that the eutectic does not represent a mechanical mixture of phases, rather single system of interacting phases.

Quasi-binary eutectic composite is a system consisting of two pure components (if there is no solubility of the components) and contact boundary between them, which may be coherent, semicoherent and amorphous depending on the ratio between the parameters of their crystal lattices.

If the general principle of calculating the theoretical strength under uniaxial tension through the energy of the system for the pure components is known, such a task is quite uncertain and complex for composites and it is due to the influence of the boundary of coupling between components.

Method for determination of the total energy of the alloy per molecule within the pseudopotential method framework is based on the summation of paired intermolecular interactions [33].

If C is the concentration of component A, then for the energy of the system from two components one can write

$$U = U_{AA}C^2 + U_{BB}(1-C)^2 + 2C(1-C)U_{AB}. \qquad (76)$$

Here

$$U_{AA}C^2 = \frac{1}{2N}\sum_{i \neq j} \Phi_{AA}(R_{ij}), \qquad (77)$$

$$U_{BB}(1-C)^2 = \frac{1}{2N}\sum_{i \neq j}\Phi_{BB}(R_{ij}), \qquad (78)$$

$$U_{AB} \cdot 2C(1-C) = \frac{1}{2N}\sum_{i \neq j}\Phi_{AB}(R_{ij}), \qquad (79)$$

where Φ_{AA}, Φ_{BB}, Φ_{AB} – potentials of interaction between the components [35].

It is assumed that both crystals are ideal, the first component has only bindings A – A, the second component bindings B – B, and at the interface — only bindings A – B. Relation (89) can be written as

$$U = U_{AA}C^2 + U_{BB}(1-C)^2 + 2C(1-C)U_{AB} = C^2 U_{AA}^* + (1-C)^2 U_{BB}^*, \quad (80)$$

где

$$U_{AA}^* = U_{AA} + U_{AB}\frac{1-C}{C}, \qquad (81)$$

$$U_{BB}^* = +U_{BB} + U_{AB}\frac{C}{1-C}. \qquad (82)$$

Stresses along the z-axis are defined by the relation [39]

$$\sigma_z = \frac{1}{S_i \cdot d} \cdot \frac{\partial U_{ii}(d)}{\cdot \partial e_z}, \qquad (83)$$

where e_z – relative deformation, and U_{ii} is U_{AA} or U_{BB}, d – lattice parameter in the direction of the axis of deformation, S_i – area of an atomic plane in a crystal lattice, perpendicular to the axis of deformation.

To calculate the physico-mechanical properties of the composite it is necessary to find the dependence of the energy of electron-ion system from the lattice parameter of the system. A common lattice parameter is necessary for the quasi-binary eutectic composite, which is absent, because each component crystallizes in its own crystal structure. To solve this problem, we introduce the

concept of "virtual" cell along the coupling boundary. The unit cell volume, which corresponds to the composition of such composite $\Omega = C\Omega_A + (1-C)\Omega_B$ (C – concentration of one of the components of the quasi-binary composite), then the system has a common lattice parameter and, accordingly, the calculation of the theoretical strength for such systems is carried out as usual.

If we present virtual crystal as a mixture of two components, and take into account that each cell corresponds to a single molecule, then it is possible to calculate total energy of the system similar to substitution alloys.

We calculate the theoretical strength under uniaxial tension by standard procedure, assuming that the axis of deformation of the virtual crystal is parallel to the axis of deformation for pure components. After calculating the strength under uniaxial deformation (deformation direction is fixed, it is the same as the direction of the axis of the fiber), we separate the contribution from member U_{AB} (the part that is responsible for the interaction A–B). As a result, we have the following summands:

$$\sigma_A = \frac{1}{d_A \cdot S_A}\frac{\partial U_{AA}(d_A)}{\partial e_z}; \quad \sigma_B = \frac{1}{d_B \cdot S_B}\frac{\partial U_{BB}(d_B)}{\partial e_z}; \quad \sigma_{AB} = \frac{1}{d_V \cdot S_V}\frac{\partial U_{AB}(d_V)}{\partial e_z}. \quad (84)$$

Here σ_A, σ_B – theoretical strength of the components taking into account their crystal lattice, d_A, d_B, d_V — parameters of the unit cell of A and B components and virtual cell in the direction of the axis of deformation, S_A, S_B, S_V – areas of atomic planes in the respective cells perpendicular to the axis of deformation.

Effective interaction between the elements of A–A taking into account the influence of the boundary A – B can be represented as the first term in (80), and the second term, respectively — as an effective interaction between B – B. The corresponding theoretical strengths will be:

$$\sigma_A^* = \left[\frac{1}{d_A \cdot S_A}\frac{\partial U_{AA}(d_A)}{\partial e_z} + \frac{1-C}{C}\frac{1}{d_V \cdot S_V}\frac{\partial U_{AB}(d_V)}{\partial e_z}\right] = \sigma_A + \frac{1-C}{C}\sigma_{AB}, \quad (85)$$

$$\sigma_B^* = \left[\frac{1}{d_B \cdot S_B} \frac{\partial U_{BB}(d_B)}{\partial e_z} + \frac{C}{1-C} \frac{1}{d_V \cdot S_V} \frac{\partial U_{AB}(d_V)}{\partial e_z} \right] = \sigma_B + \frac{C}{1-C} \sigma_{AB} . \tag{86}$$

By the rule of mixtures, excluding the influence of coupling boundaries of two components, the strength of quasi-binary systems will be

$$\sigma_K = \delta_A \sigma_A + \delta_B \sigma_B , \tag{87}$$

and taking into account the influence of the coupling boundaries we have

$$\dot{\sigma}_K = \delta_A \dot{\sigma}_A + \delta_B \dot{\sigma}_B . \tag{88}$$

Where δ_A, δ_B – volume fractions of the components of the eutectic composition in the system.

More research was conducted on a system of LaB_6-ZrB_2, because other components — TiB_2 and HfB_2 — by the structure and properties are very close to ZrB_2. Calculation of maximum strength and deformation was conducted with and without considering the influence of the coupling boundaries between components in the system. Below in tabular and graphical form are given results of computational experiments.

Fig. 49 and 50 show functional dependence of the strength on the deformation for components and composite, $\sigma_i(\delta_{max})_B$ – strength of the matrix at the maximum deformation of diboride, $\sigma_i(\delta^*_{max})_B$ – same strength but with the account of the influence of boundaries. The choice of maximum deformation was made based on the stress-strain diagram for each component.
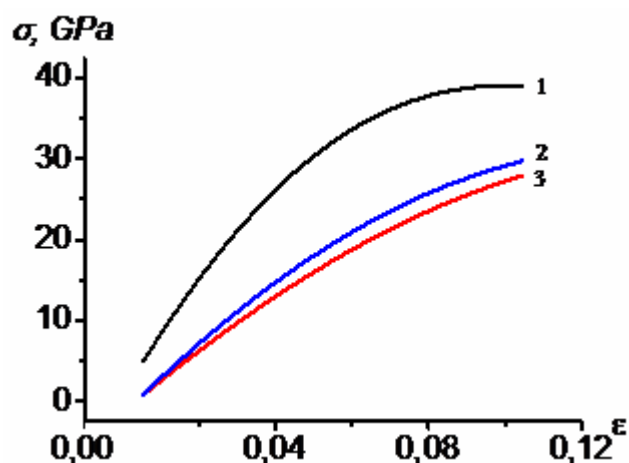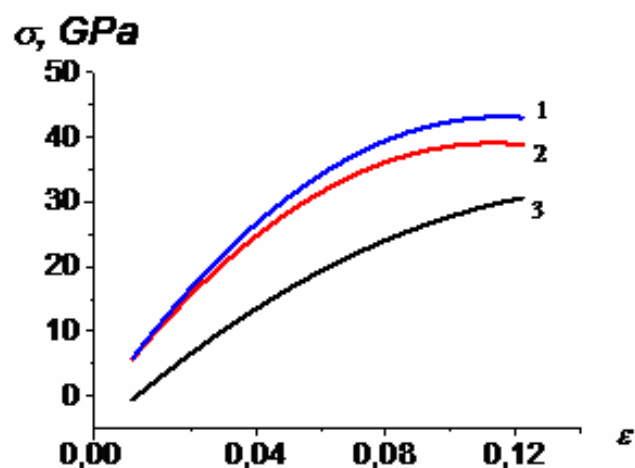
Fig. 49. Dependence of theoretical strength from deformation for 1) ZrB_2, 2) LaB_6–ZrB_2, and 3) LaB_6, calculated by (83), (87)

Fig. 50. Dependence of theoretical strength from deformation for 1) ZrB_2, 2) LaB_6–ZrB_2 and 3) LaB_6, calculated by (85), (86), (88)

By comparing the results on theoretical strength of LaB_6-ZrB_2 composite obtained from computer simulation by applying the rule of "mechanical mixture" (Figure 49), and in the case when influence of the contact boundary of two components (interface) is taken into account (Figure 50), we can conclude:

1. In the first case (the rule of "mechanical mixture") characteristic dependence strength-deformation of the composite and the matrix (LaB_6) are almost identical.

2. In the second case, the shape of dependence of strength on the composite deformation differs from that characteristic both for matrix (LaB_6) and for

reinforcing phase (ZrB_2). Accounting for the effect of the interface in calculations leads to higher values of mechanical properties of the composite, increasing its theoretical strength.

Table 14. Maximum deformation and theoretical strength (GPa) for components and composite without additional term (ε_{max}, σ_{max}) and with it (ε^{*}_{max}, σ^{*}_{max})

	ε_{max}	σ_{max}	$\sigma_i\,(\varepsilon_{max})_B$	ε^{*}_{max}	σ^{*}_{max}
ZrB_2	0.099	39.060		0.116	43.170
LaB_6	0.160	31.589	27.150		
LaB_6–ZrB_2	0.099	29.075		0.116	32.209

Maximum deformation (ε_{max}) is 0.099 for ZrB_2 and 0.16 for LaB_6 without additional term, and taking into account the influence of the coupling boundaries of two components the maximum deformation increases to 0.1161 in the case of ZrB_2 and decreases for LaB_6.

If we assume that maximum strength of the matrix in its pure form is 31.589 GPa, it is clearly seen that strength of the composite with the influence of the contact boundaries is greater than maximum strength of the pure component A.

Using formulas (83) (88) strength and corresponding deformation are calculated as a function of the concentration of components in LaB_6-ZrB_2 system. Table. 15 shows the results of calculations for maximum strength for hypoeutectic, eutectic and hypereutectic composition.

Table 15. Dependence of maximum deformation and strength of composite (GPa) from concentration of components ($C_B = 1 - C$ — concentration of ZrB_2)

C_B	0.2	0.25	0.28	0.3	0.31	0.32	0.35	0.5
ε_{max}	0.1181	0.1171	0.1165	0.1160	0.1155	0.1150	0.1140	0.1110
σ_{max}	31.457	31.560	31.860	32.027	31.999	31.999	32.450	33.703

With increasing of ZrB_2 concentration the maximum deformation of the composite decreases and strength increases. When $C_B = 0.3$ the composite has maximum strength in the region $0 < C_B < 0.33$. A further increase in concentration leads to ZrB_2 gradual increase in the strength of the composite, and maximum value is reached at $C_B = 1$.

Account of the interaction of components in the composites at the coupling boundary leads to an increase of both the maximum deformation of refractory component in the composite and the theoretical strength of the composite.

The obtained local maximum of strength for the composite in the eutectic point is the confirmation of the fact that eutectic is not just a mechanical mixture and that for the eutectic are characteristic not only minimum temperature of formation, but also superiority of mechanical properties.

Conclusion:

- A model is developed to account for changes in the volume of the unit cell at temperatures different from zero based on the method of pseudopotentials (second-order of perturbation theory) the so-called quasi-harmonic approximation.
- - In quasi-harmonic approximation the calculated thermal expansion coefficients for LaB_6 and LaB_6-MeB_2 (Me - Zr, Ti) systems based on it have a jump in the temperature range from 750 K to 1000 K, which is associated with the presence of a deeper minimum of energy of B_6 complex than interaction energy between La and B atoms, or La-La atoms. Therefore, in the initial stage of raising the temperature to 750 K it is La atoms that are displaced from the equilibrium position. At higher temperatures B_6 volume complex begins to participate in the expansion, which leads to a jump in the coefficient of thermal expansion.

- With the help of quasi-harmonic approximation theoretical strength of borides (LaB_6, MeB_2) and LaB_6-TiB_2 system with eutectic composition under uniaxial deformation in the temperature range from 0 to 2750 K were calculated. The characteristic, almost linear dependence of the strength from the temperature changes in the temperature interval (1300 K-2200 K) in the case of LaB_6, an increase in temperature leads to an increase in the theoretical strength. Same dependence is observed for LaB_6-MeB_2 (Me - Ti, Zr, Hf) systems, where in eutectic systems LaB_6 is 0.7 mol. part. The observed deviation in the dependence "theoretical strength – temperature" is a consequence of change in the coefficient of thermal expansion.

- Based on the results of computational experiments, a model of formation of interphase boundaries in the quasi-binary eutectic systems was proposed. Quasibinary eutectic is a system consisting of two almost insoluble components, bonded on the coupling boundary using shared atoms or compounds formed from atoms of the components.

- With the help of introduced concept of "virtual cell" along the coupling boundary of components the surface energy of the interface between the components in the boride and metal-ceramic quasi-binary composites with eutectic composition was calculated. The surface energy of the interface for LaB_6-TiB_2, LaB_6-ZrB_2 systems at different temperatures was calculated. With increasing temperature, the contact surface energy decreases, but the system retains its characteristic mechanical properties up to melting temperature (eutectic temperature).

- The contact surface energy depends on the ratios between the crystal lattice parameters of components.

- A relationship was obtained that takes into account effect of the interface on mechanical properties of the composites. Using these relations, theoretical strength of LaB_6-ZrB_2 and maximum possible deformation were calculated. Under this approach, the dependence of the theoretical strength on

concentration of components was found, and the existence of a local maximum of theoretical strength for the composite in the eutectic point was demonstrated.

- The obtained local maximum of strength for the composite in the eutectic point is the confirmation that eutectic is not just a mechanical mixture and it is characterized by not only the minimal temperature of formation, but also the superiority of mechanical properties.

6. The ideal work of adhesion interface component eutectic

One of the promising methods used in materials science for production of composite materials is the directional solidification of eutectic ceramic. Directionally crystallized under certain process conditions composites based on of LaB_6–$Ti_xZr_{1-x}B_2$ system have a high level of physical and mechanical properties such as strength and fracture toughness. This level of properties is achieved due to specific eutectic microstructure of the composite — diboride fibers uniformly distributed in the matrix of lanthanum hexaboride. Computer simulation of the formation of these eutectic alloys using phenomenological models allows us find optimal modes of crystallization. However, these models include a number of parameters which are very difficult, and sometimes impossible, to establish experimentally. One such parameter is the ideal work of adhesion, which is defined as the work required for reversible separation of the interface into two free surfaces without plastic deformation and diffusion. From a practical point of view, of considerable interest is to clarify the nature of the influence of impurities, in particular titanium on the properties of the interface. It was established experimentally that between the components of LaB_6-$Ti_xZr_{1-x}B_2$ system the following crystallographic orientation relationships are observed: [001]-LaB_6//[001]-$Ti_xZr_{1-x}B_2$, (110)-LaB_6//(110)-$Ti_xZr_{1-x}B_2$. For these orientation relationships the results of calculations are presented of ideal work of adhesion for both coherent and semicoherent interfaces for $x = 0, 0.57, 1$.

The ideal work of adhesion W_{ad} is defined as the energy required to separate interface into two free surfaces. At the same time plastic and diffusion processes are neglected [66]. In accordance with this definition, adhesion energy can be calculated as follows:

$$W_{ad} = (E_A + E_B - E_{AB})/S , \tag{82}$$

where E_{AB} – total energy of supercell containing interface LaB_6 and $Ti_xZr_{1-x}B_2$. E_A and E_B – total energies of isolated phases LaB_6 and $Ti_xZr_{1-x}B_2$ respectively, S – contact area контакта.

The calculations of the total energies was carried out using the software package Quantun-Espresso (version 4.3.2) [67]. This package implements ab initio pseudopotential method in combination with density functional theory. To obtain adequate results with ab initio methods we need carefully select a number of calculation parameters that determine the accuracy of calculations. To such parameters in the ab initio pseudopotential method belong cutoff energy E_{cut} in the expansion of plane waves and the number k of points in the Brillouin zone. To select these parameters calculations of the total energy of LaB_6, ZrB_2 were carried out. Calculations were carried out for experimental parameter data. The results of calculations are presented in Fig. 51, and variants of systems of points k — in Table 16.

Analysis of the results shows that the accuracy of the calculation of the total energy 1 mRy is achieved by using a system of points 16x16x16 (variant 5), $E_{cut} =$ 40 Ry for LaB_6 and Ry = 30 Ry for ZrB_2. These values were used to calculate the equilibrium lattice parameters of LaB_6, ZrB_2 and TiB_2.
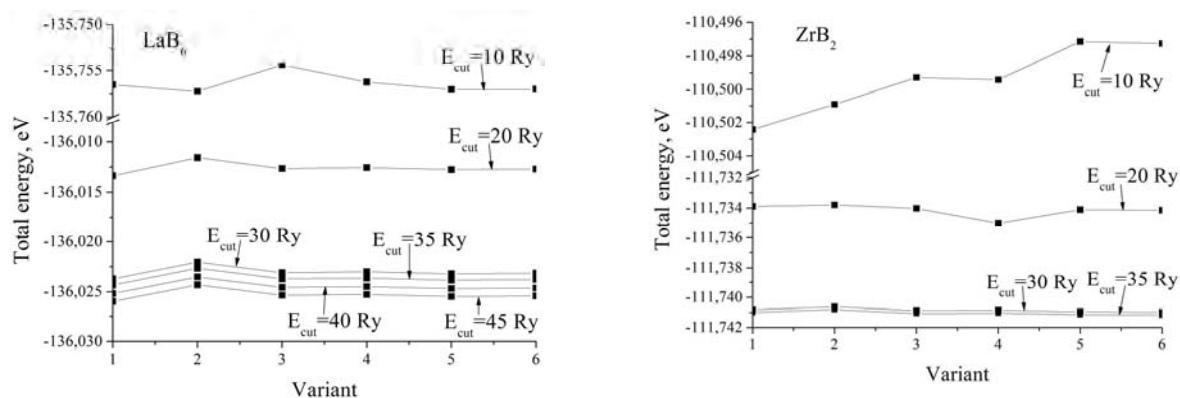
Fig. 51. Total energy of LaB$_6$ and ZrB$_2$ at different temperatures of calculations.

Table 16. Calculation parameters.

Calculation variant	System of points k
1	6x6x6
2	8x8x8
3	10x10x10
4	12x12x12
5	16x16x16
6	20x20x20

LaB$_6$ belongs to a simple cubic structure, however, it has two structural parameters, lattice parameter a and parameter u, which determines the position of boron atoms in the unit cell. For their determination calculations of the total energy for a set of lattice parameters with relaxation of the positions of boron atoms were carried out. The obtained dependence is shown in Figure 52.
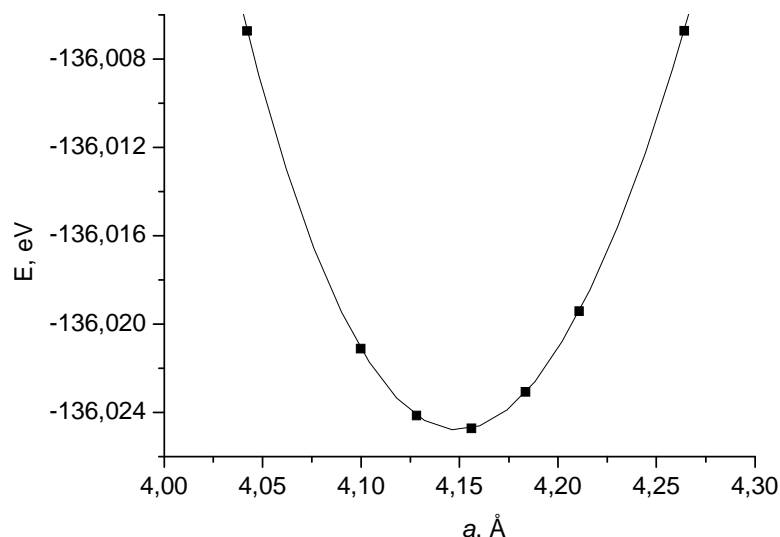
Fig. 52. Dependence of total energy of LaB_6 from lattice parameter.

The equilibrium lattice parameter determined from this dependence is $a_0(LaB_6) = 4.1491$ Å. This lattice parameter corresponds to the value $u = 0.1999$. The experimental values are, respectively, 0.1995 and 4.1491 Å [68].

ZrB$_2$ and TiB$_2$ belong to hexagonal structure and have two lattice parameters a and c. Total energy of ZrB$_2$ was calculated on the mesh from five values of a and five values of c/a. The figure shows surface contours of the total energy in the coordinates volume (V) – ratio c/a. The resulting surface was approximated by two-dimensional Chebyshev polynomials of order 4. The accuracy of the approximation is 2-4 units of sixth decimal place in the total energy. Determination of the minimum of approximating function yielded the following values of the lattice parameters: $a_0(ZrB_2) = 3.1697$ Å, $c_0(ZrB_2) = 3.5418$ Å. The experimental values are respectively 3.170 and 3.532 Å [4]. For TiB$_2$ calculated values of the lattice parameters were $a_0(TiB_2) = 3.0307$ Å, $c_0(TiB_2) = 3.2208$ Å (experimental values are equal to $a = 3.026$ Å, $c = 3.213$ Å [69]).
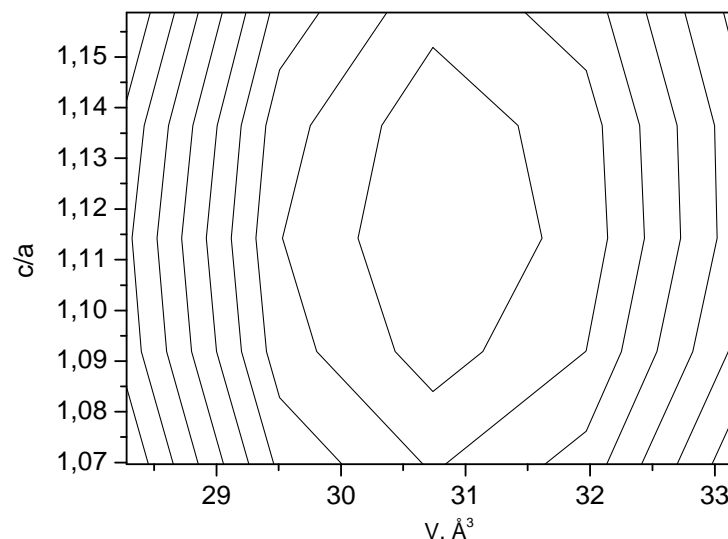
Fig. 53. Contours of the surface of total energy for ZrB_2.

For eutectic of LaB_6-$Ti_xZr_{1-x}B_2$ the following orientation relationships in the formation of the interface between the diboride fibers and lanthanum hexaboride matrix were experimentally observed: [001]-LaB_6 // [001]-ZrB_2, (110)-LaB_6 // (110)-ZrB_2. A detailed analysis of these orientation relationships gives the following results. For lanthanum hexaboride at the interface plane exists a rectangular lattice of lanthanum atoms with parameters $a(LaB_6) = \sqrt{2}a_0(LaB_6) = 5.8677$, $b(LaB_6) = a_0(LaB_6) = 4.1491$ Å. Each node of the plane lattice is associated with boron octahedron with two boron atoms lying in the plane and the other four are located symmetrically on opposite sides of the plane.
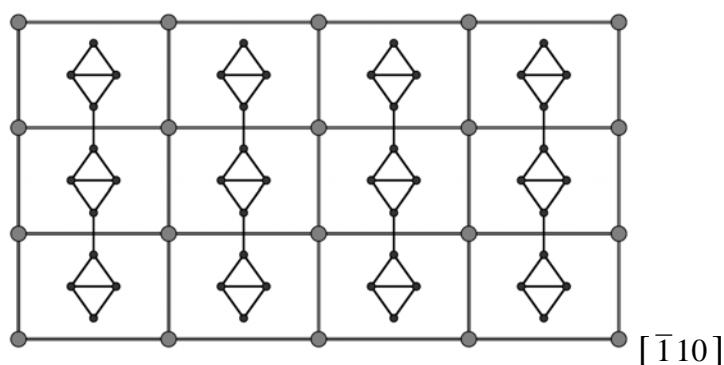
[001]

$[\bar{1}10]$

Fig. 54. Interface plane of LaB_6.

For zirconium diboride/titanium on interface plane also exists a rectangular lattice of atoms zirconium/titanium with parameters $a(ZrB_2) = \sqrt{3}a_0(ZrB_2) = 5.4901$, $b(ZrB_2) = c_0(ZrB_2) = 3.5418$ Å ($a(TiB_2) = \sqrt{3}a_0(TiB_2) = 5.2493$, $b(TiB_2) = c_0(TiB_2) = 3.2208$ Å).
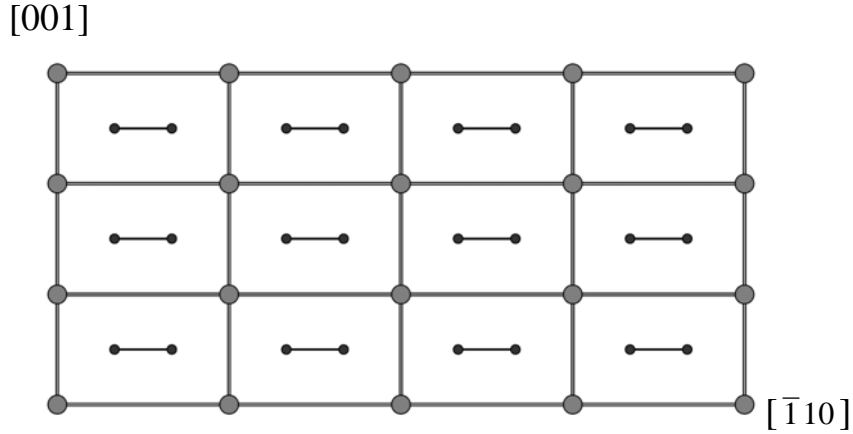
[001]

Fig. 55. Interface plane ZrB_2/TiB_2.

Thus the lattice mismatch at the interface planes of LaB_6 and ZrB_2/TiB_2 turns out to be different in the directions $[\bar{1}10]$ and $[001]$. So, for the $[\bar{1}10]$ direction this discrepancy is $\delta_1(ZrB_2) = 0.066$ ($\delta_1(TiB_2) = 0.111$), and for the $[001]$ direction $\delta_2(ZrB_2) = 0.158$ ($\delta_2(TiB_2) = 0.252$). These values show that it is possible for ZrB_2 in the direction of $[\bar{1}10]$ provide a coherent interface with a relatively small mismatch. The lowest commensurate unit cell along the $[001]$ direction should consist of six unit cells of LaB_6 and seven cells of ZrB_2 and contain misfit dislocations. For TiB_2 mismatch in both directions is significantly greater than for ZrB_2. Nevertheless, both coherent and semicoherent interface for zirconium and titanium diboride were constructed the same way.

To perform calculations of ideal work of adhesion W_{ad} as a first approximation we developed four models of interface M1-M4, coherent along the $[\bar{1}10]$ and $[001]$ directions (Fig. 56). In order to ensure coherency the lattice parameters of ZrB_2 and TiB_2 were changed accordingly. Supercell consisted of three layers of LaB_6 and three layers of ZrB_2/TiB_2, separated by a vacuum gap of ~ 10 Å and contained 70 atoms.
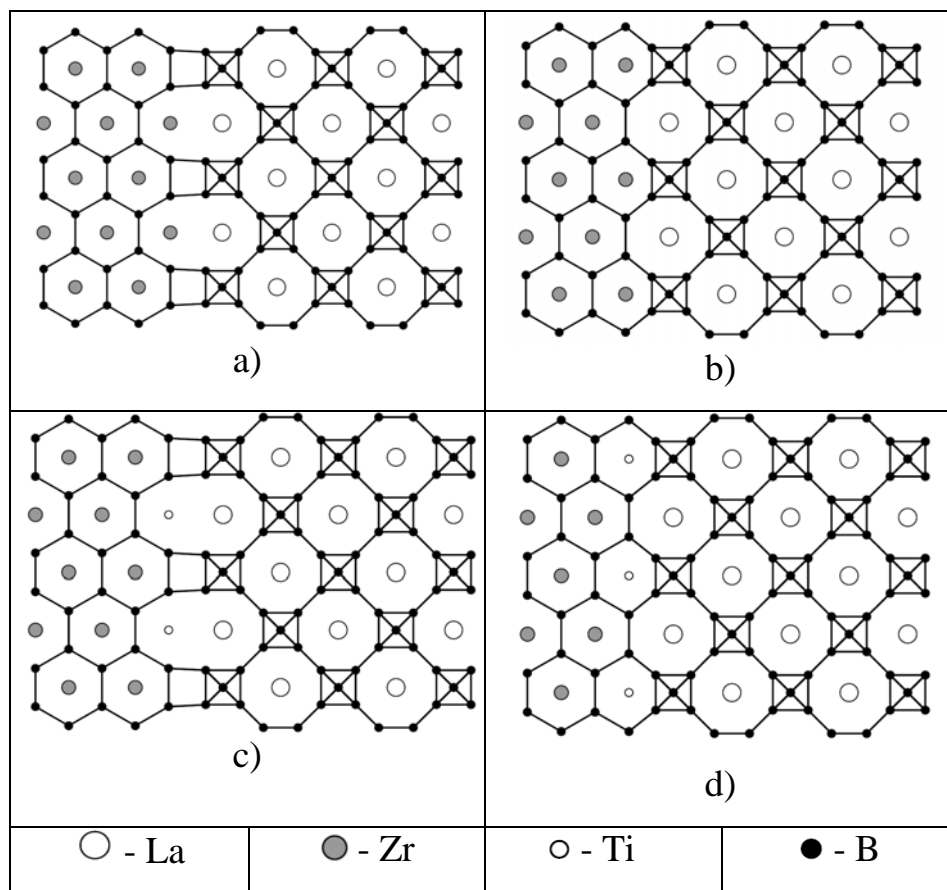
Fig. 56. Atomistic models of interface [001]-LaB$_6$//[001]-Zr(Ti)B$_2$, (110)-LaB$_6$//(110)-Zr(Ti)B$_2$: a - d — models M1 – M4 respectively

In the M1 model boron atoms on the interface surfaces of LaB$_6$ and ZrB$_2$ are linked by "bridging" ties. Due to this structure of interface, there are regions in which atoms of lanthanum and zirconium are situated opposite each other and are located close enough. In the M2 model lanthanum and zirconium atoms are surrounded by atoms of boron and do not contact each other. In the M3 and M4 models zirconium atoms closest to the interface plane are replaced by titanium atoms. This substitution allows us to trace the influence of titanium admixture on the ideal work of adhesion.

The energies of the systems under consideration are calculated as a function of the distance between the interface surfaces. The obtained dependences are shown in Fig. 57. From these curves the equilibrium distances d_0 between the interface

surfaces and the magnitude of ideal work of adhesion W_{ad} are determined. The results of the calculation are given in Table 17.
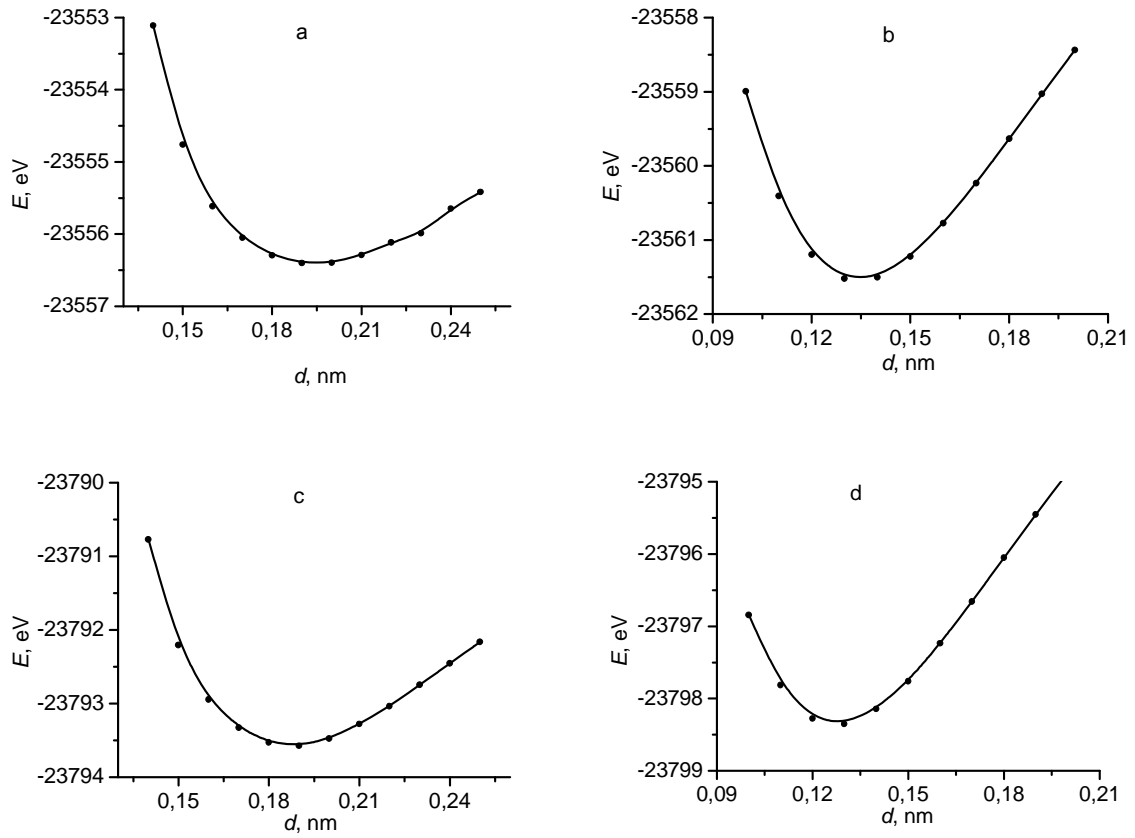

Fig. 57. Interface energy as a function of the distance between the interface surfaces: a - d — models M1 – M4, respectively.

Table 17. Ideal work of adhesion and equilibrium distances between interface planes.

Parameter	M1	M2	M3	M4
W_{ad}, J/m^2	1.89	1.34	2.23	5.39
d_0, nm	0.189	0.198	0.186	0.127

At the equilibrium distance $d_0 = 0.189$ nm between the interface surfaces, the distance between the nearest atoms of zirconium and lanthanum in the model M1 is equal to 0.277 nm. This distance is less than the sum of the atomic radii (0.160 nm

for Zr and 0.186 nm La [70]) of the respective elements. In connection with this, the question arises of the validity of the model M1. Note, however, that in LaB_6 and ZrB_2 chemical bond between the metal atoms and boron has a partially ionic character and the metal atoms are ionized in these compounds. It is therefore more correct to consider the ionic radii which are equal to 0.087 nm for Zr^{+4} and 0.122 nm for La^{+3} [70]. Comparing Fig. 57a, b and 57c, d shows that more energetically advantageous are interface models M4 and M2 in comparison with the models M1 and M3, respectively.

From these data it follows that the presence of titanium atoms in the plane of the interface leads to a considerable increase in the work of adhesion.

The ideal work of adhesion W_{ad} in the approximation of semicoherent interface taking into account relaxation of atomic positions were calculated for ZrB_2, $Ti_{0.57}Zr_{0.43}B_2$, TiB_2.

Fig. 58 shows the model of semicoherent interface.

⬤ - La   ○ - Zr   ● - B

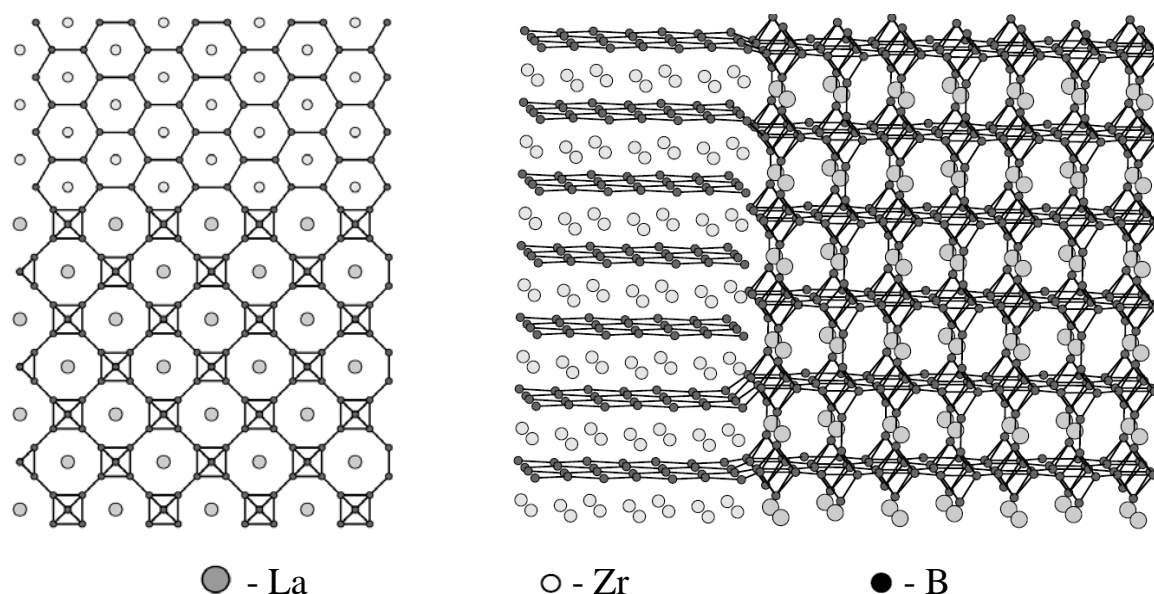Fig. 58. Model of semicoherent interface for LaB_6-ZrB_2: left – top view; right – side view.

For calculations of ideal work of adhesion W_{ad} in the approximation of semicoherent interface taking into account relaxation of atomic positions in a reasonable time, we had to use a supercell with fewer layers of LaB_6, ZrB_2/TiB_2, than for calculations in the approximation of a coherent interface. However, the computational experiments showed that a reduction in the number of atoms in supercell by 30% changes only third decimal place in the calculated ideal work of adhesion. In this case, the calculation time is reduced by about ten times

Fig. 59 shows the appearance of semicoherent interface LaB_6-ZrB_2 before relaxation and after relaxation of atomic positions.
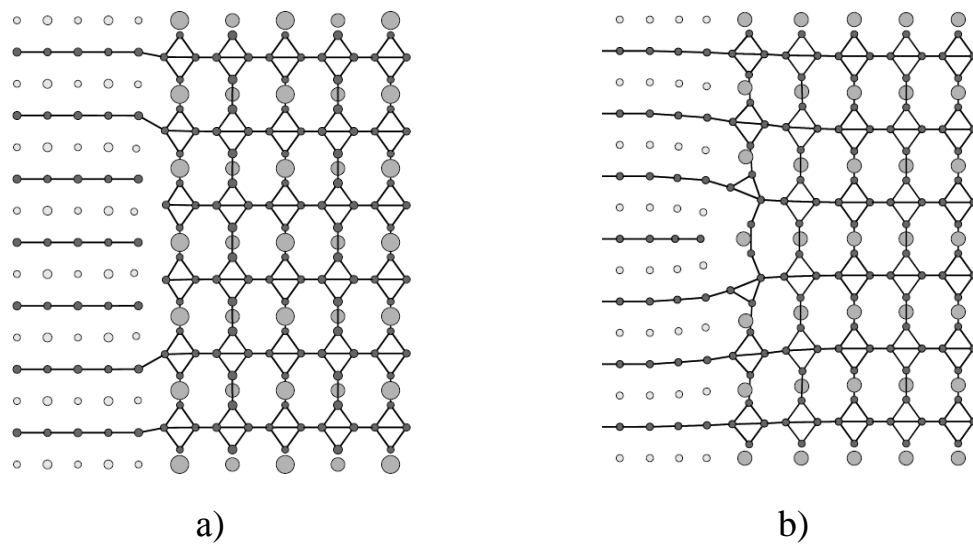

a) b)

Fig. 59. Semicoherent interface: a) before relaxation of atomic positions; b) after relaxation. Atoms La – large gray circles, Zr – small gray circles, B – black circles.

Energy of LaB_6-$Ti_xZr_{1-x}B_2$ (x = 0, 0.43, 1) systems was calculated as a function of the distance d between the interface surfaces (Fig. 60).
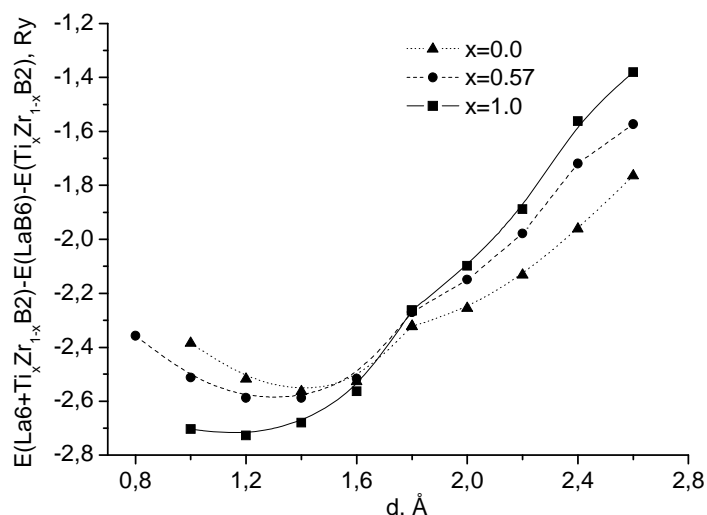
Fig. 60. Energy of the interface as a function of the distance d between interface surfaces.

The table below shows the equilibrium distances d_0 between interface surfaces and ideal work of adhesion W_{ad} calculated from these curves.

Table 18.

x	d_0, Å	$W_{ad}, J/m^2$
0.00	1.429	3.828
0.57	1.329	3.874
1.00	1.139	4.075

The table shows that the presence of titanium increases the ideal job of adhesion. The greatest work of adhesion is observed for the interface with TiB_2.

In [71] it was shown that the substitution of zirconium by titanium causes a change in the growth direction of the fibers during directional solidification of LaB_6-$Ti_xZr_{1-x}B_2$ eutectics. One reason for this behavior of the system may be a significant energy loss in case of constant growth direction of the TiB_2 fibers. For a qualitative understanding of the problem the calculations have been carried out of the magnitude of additional energy that have to be expended to ensure

semicoherent interface for TiB_2 and ZrB_2 taking into account the availability of free surface. For ZrB_2 additional energy was 1.11 eV/(elem. cell), and for the TiB_2 – 3.78 eV/(elem. cell). Thus, energy loss during the formation of the semicoherent interface in the case of titanium diboride is substantially higher – 3.4 times than in the case of zirconium diboride.

Conclusions.

The ideal work of adhesion of interface $[001]$-LaB_6//$[001]$-$Ti_xZr_{1-x}B_2$, (110)-LaB_6//(110)-$Ti_xZr_{1-x}B_2$ increases with increasing titanium content. Change in the direction of fibers growth during directional solidification of LaB_6-$Ti_xZr_{1-x}B_2$ eutectics is associated with a large loss of energy in the formation of semicoherent interface with increasing titanium content.

7. Simulation of the segmentation process of $Ti_{14}C_{13}$ and $Ti_{13}C_{14}$ nanoclusters

The interest to cluster models of crystal segmentation increased after stable nanoclusters were experimentally obtained. For the Ti-C system Ti_8C_{12} titanocarbohedrene [72] proved to be the most stable, having the fullerene-like form of C_{20}. It was also shown [73], that clusters with such stoichiometric composition can exist in different symmetric forms. In [74] the synthesis of a number of cubic nanocrystals with the structure of NaCl was reported: $Ti_{14}C_{13}$ (3x3x3), $Ti_{18}C_{18}$ (4x3x3), $Ti_{23}C_{22}$ (5x3x3), $Ti_{24}C_{24}$ (4x4x3), $Ti_{27}C_{27}$ (6x3x3), $Ti_{30}C_{30}$ (5x4x3), $Ti_{32}C_{32}$ (4x4x4), $Ti_{36}C_{36}$ (6x4x3). The existence of these samples was confirmed in experiments [75].

In [76] "ab initio" calculations were carried out within the framework of density functional theory using the method of generalized gradient approximation (GGA) for a series of clusters including mentioned $Ti_{14}C_{13}$, $Ti_{13}C_{14}$ and truncated fragments of these clusters without corner atoms Ti_6C_{13} and $Ti_{13}C_6$. With the help of estimates of the interatomic distances for Ti-C bonds and average energies of

these bonds it was concluded that angle atoms weakened by bonds do $Ti_{13}C_{14}$ cluster metastable. This conclusion is also confirmed by calculations of the vibrational spectra of atoms.

Obviously, the combination of many unique structural and electronic features, it creates the preconditions for the development of materials promising for application in many fields by segmenting or assembling clusters [77]. Self-assembly of nanoclusters in crystalline structures strongly depend on the type of symmetry of nanoclusters themselves and composites based on them. In [78] group-theoretic relations are detailed conducive to the evolution of the crystals. It is shown that the same group-theoretic conditions can lead to a variety of macrostructures, determined by the physico-chemical properties of atoms (e.g. atomic radii, electronic structure), and this stipulated the introduction of the concept of channels of evolution.

Questions of self-assembly or segmentation of nanocrystals mentioned above, as well as their stability has not yet been studied adequately. In particular, it is interesting how cubic nanocrystallites of (3x3x3) (4x3x3) type and the like, but with a larger number of atoms, which are composites of a series of two flat fragments of Ti_5C_4 and Ti_4C_5 are formed. Can there be such forms, at least in a metastable state; whether fragmentation of nanocrystals from these planes is possible? In this section we describe approaches to answer these questions. With this purpose in mind, we theoretically investigated the stability and the interaction of plane nanoclusters of Ti_5C_4 and Ti_4C_5 types and conducted a number of computational experiments to help understand the conditions of their segmentation into cubic clusters $Ti_{14}C_{13}$ and $Ti_{13}C_{14}$. Cluster model calculations were carried out "from first principles" within the density functional theory framework using the software package "Gaussian'03" [79].

Electronic properties and stability of planar nanoclusters Ti_5C_4 and Ti_4C_5

Fig. 61 presents planar clusters, which can be regarded as the splitting of the cubic nanocrystallite (3x3x3) into three planes Ti_5C_4-Ti_4C_5-Ti_5C_4 or Ti_4C_5-Ti_5C_4-Ti_4C_5.
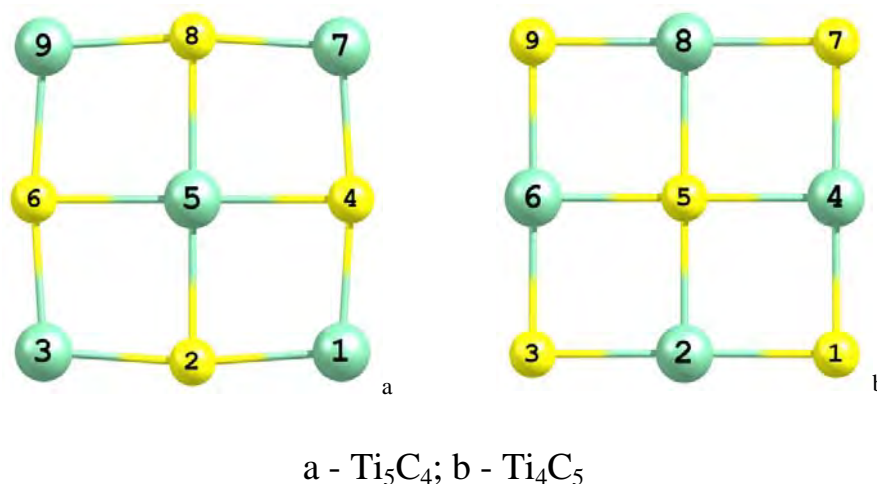

a - Ti_5C_4; b - Ti_4C_5

Fig. 61. Optimized planar clusters

In the first case $Ti_{14}C_{13}$ crystallite contains one atom of titanium in excess, and in the second $Ti_{13}C_{14}$ – one carbon atom. As can be seen from Fig. 61, both planar nanoclusters have only three inequivalent atoms: one central with a coordination number $K = 4$, four corner ($K = 2$) and four atoms at the centers of the edges ($K = 3$). Accordingly, they form 12 bonds Ti–C, and among them only two are different "corner atom – center of the edge" (1,2) and the "center of the edge – central atom of the facet" (2,5). The angle between the atoms $2 – 1 – 4$ we denote as $A(2,1,4)$. Table 19 provides the structural, energetic, and electronic properties of these forms. The average energy of the Ti-C bond was calculated as the binding energy divided by the number of bonds in the cluster. The gap in the energy spectrum, which separates the occupied states from free (LUMO-HOMO) has a plus sign in the presence of a semiconducting gap and the minus sign in the case of overlapping zones. The values of the electronic charge transfer according to Mulliken are given for non-equivalent atoms.

Table 19. Geometric and electronic properties of planar nanoclusters

	Ti_5C_4	Ti_4C_5
Ti-C Bond length (1.2), nm	0.1936	0.1925
Ti-C Bond length Ti-C (5.2), nm	0.2018	0.1977
Angle (2,1,4) grad.	94.99	93.13
Binding energy/atom, eV	8.3753	8.0917
Average energy of Ti-C bond, eV	6.2815	6.0688
LUMO-HOMO, eV	0.6942	0.6095
Charge transfer by Mulliken:		
Angle atom (1)	Ti 0.2117	C -0.2284
Atom in the edge center (2)	C -0.3135	Ti 0.2589
Central atom (5)	Ti 0.4071	C -0.3103

The effect of optimization can be seen from the geometrical parameters of the planar clusters. As the initial value of the Ti-C bond length the magnitude of 0.21 nm was taken (the experimental value 0.2176 nm). Table 19 shows that in the result of optimization the compression of the structure has occurred, but not entirely uniform. The distance from the central atom to the midpoints of the sides of the rectangle became greater than the distance from the corner atoms towards the midpoints of the edges. For Ti_5C_4 the ratio of these lengths is equal to 1.04, and for Ti_4C_5 – slightly less than 1.03. Accordingly, the angle of the rectangle in the first case increased to 95°, and in the second – to 93°. Overall, in both cases the structure of the figure is preserved but only with some distortion. Cohesive energy and the average energy of the Ti-C bond is a little more in the cluster Ti_5C_4. This indicates that the cluster has a more strong structure. Calculations show that both objects have in the energy spectrum a small semiconductor gap. Charge transfer is of the same type: titanium atoms give some fraction of the electron charge to carbon atoms. However, if in Ti_5C_4 titanium atom located in the center of the fragment, gives the greatest charge, and angular titanium atoms - lower, but equal,

and carbon atoms have equal charge, then in Ti_4C_5 titanium atoms 4 and 6 give somewhat greater charge than atoms 2 and 8. In the carbon subsystem central atom takes the largest share of the charge, and angular atoms – a smaller but equal parts.

Software package "Gaussian'03" allows to calculate vibrational spectra of atoms, molecules and clusters. Calculation of atomic vibrations allows one not only determine the most active frequencies and type of oscillation, but also provide information on the structural stability of the object. Thus, the presence of imaginary frequencies in the spectrum indicates that during optimization not stationary condition was found but transit [80]. In the case of planar nanoclusters the calculations indicated the presence of imaginary frequencies in the spectra of both structures. It means that Ti_5C_4 and Ti_4C_5 are metastable structural formations that have a limited lifetime. During this period of time nanoclusters may undergo structural changes or merge with other clusters during segmentation. Oscillations corresponding to imaginary frequencies in both cases are due to oscillations of carbon subsystem. In the case of Ti_5C_4 it is double type E_u of longitudinal and transverse (Z = 0) plane oscillation of carbon atoms. In Ti_4C_5 imaginary frequency corresponds to oscillations A_{2U} of five carbon atoms along the axis Z, perpendicular to the plane of the nanocluster.

Segmentation of planar nanoclusters Ti_5C_4 and Ti_4C_5

Geometric optimization of a molecule or cluster in software package "Gaussian'03" is achieved by finding the minimum of the potential energy surface by gradient methods [80]. As the minimization parameters we used nonequivalent nearest interatomic distances, angles between the interatomic bonds and sums of the lengths of the bonds between the four atoms. Thus, even for small clusters the number of parameters can be quite large. For example, for planar Ti_5C_4 and Ti_4C_5 clusters consisting of 9 atoms the number of geometrical parameters is 52 and 68, respectively. To optimize structure of 27-atom cubic cluster of $Ti_{14}C_{13}$ 930 parameters are used.

Such a powerful optimization procedure can be used not only to clarify the configuration of atoms in the clusters already complete, but also in the analysis of dynamic behavior of free atoms, molecules, and small fragments. Some of these tasks include segmentation of several nanoclusters, separated by a sufficiently large distance from each other. This section examines possible cases of segmentation of three planar nanoclusters of Ti_5C_4 and Ti_4C_5 type, spaced at some distance in two coordinate axes. The goal of computational experiments is to address two issues. First, whether segmentation of three planes into cubic nanocluster is possible and under what conditions can this happen? Second, how will selected planar structures behave themselves under a sufficiently large disordering?
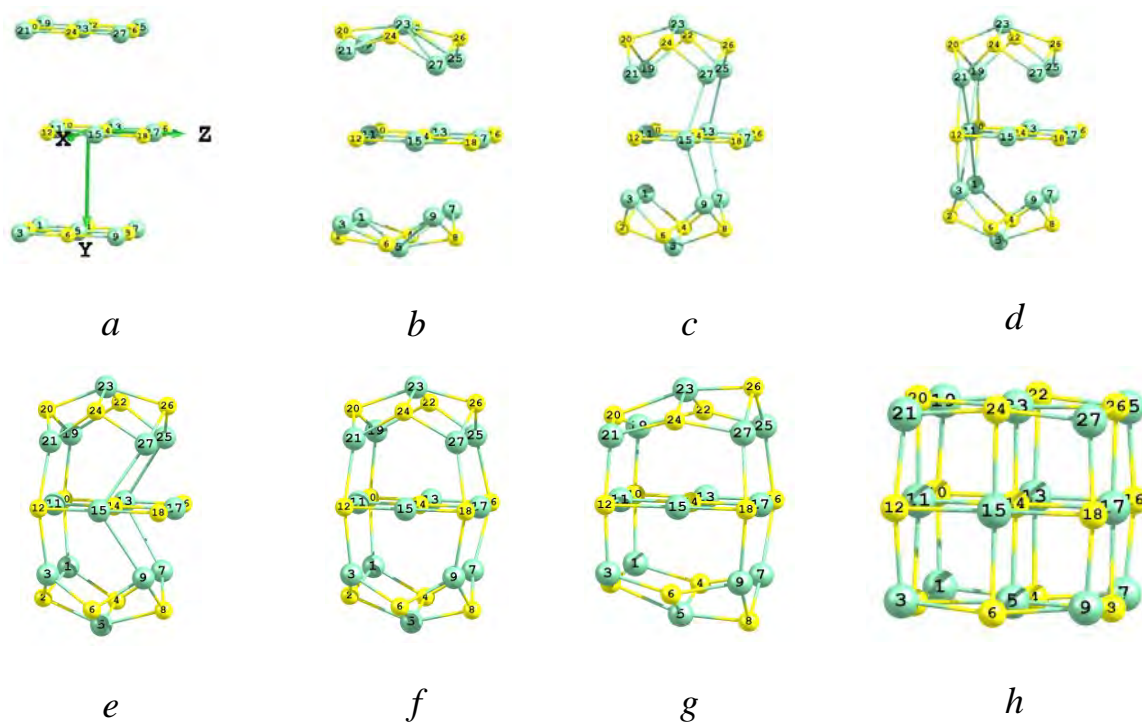
a – initial configuration; b - step 25; c - step 33; d - step 36; e - step 41; f - step 42; g - step 50; h - step 93, optimized structure

Fig. 62. Segmentation of planar fragments Ti_5C_4 - Ti_4C_5 - Ti_5C_4 (Dy = 0.4 nm, Dz= 0.1 nm) into cubic nanocluster during geometric optimization

In a simple parallel shift of three planes in the segmentation into cubic nanocluster no special problems do emerge. More interesting are the cases of

mutual movement of the planes along two axes. The results of five segmentation variants are shown in Fig. 62-66. Sequence of three planar fragments Ti_5C_4 - Ti_4C_5 - Ti_5C_4 we denote as (1) - (2) - (3). Origin of coordinates is placed to the central atom of fragment (2), in this case a carbon atom. Fragment (2) lies in plane XZ, fragments (1) and (3) are separated from the central (2) along the Y axis in both directions. Fig. 62 illustrates an optimization process of the **first variant** of the system with fragments shifted along the Y axis by an Dy = 0.4 nm and along the Z axis by Dz = 0.1 nm.

As can be seen from Fig. 62 segmentation of planar fragments into cubic nanocluster $Ti_{14}C_{13}$ (3x3x3) is a rather complex process. First of all, we note that titanium atoms are the most active, it is the metal-metal interaction of adjacent planes that causes the attraction of fragments (1) and (3) to the center (2). After the "skeleton" is built with titanium atoms (e), a process of ordering of carbon atoms to the full cube symmetry is started. Characteristically, the central fragment (2) remains substantially unchanged and the picture retains symmetry with respect to the Y axis, because planes (1) and (3) in the initial configuration are shifted with respect to (2) by the same distance.

In the **second variant** the segmentation of the system of planar fragments with a predominance of carbon atoms $Ti_4C_5 - Ti_5C_4 - Ti_4C_5$ into cubic nanocluster $Ti_{13}C_{14}$ (3x3x3) was considered. The coordinate system was selected similarly to the case considered, but now in the center of the fragment (2) is titanium atom, the displacements along the axes remain the same.

The optimization process proceeds approximately similar to the scenario of the first variant but with some difference. At the first stage fragments (1) and (3) approach planar fragment (2) and attempt to establish interaction between the metal atoms. Fig. 62c and Fig. 63c illustrate methods of bonding. In the first case, the metal atoms of the central chain of atoms Ti – C – Ti of the plane (2) interact with the metal atoms of the boundary chains Ti – C – Ti of fragments (1) and (3) that have lost their flat shape. In the second, on the contrary, the metal atoms of

central chains of Ti – C – Ti fragments (1) and (3) bind to the metal atoms of the boundary chain Ti – C – Ti of planar fragment (2). But this interaction is unstable (Fig. 64*d*) and after some displacement of fragments (1) and (3) along the Z axis it becomes possible and energetically advantageous to establish links Ti - C between the boundaries of fragments (Fig. 63*e*).
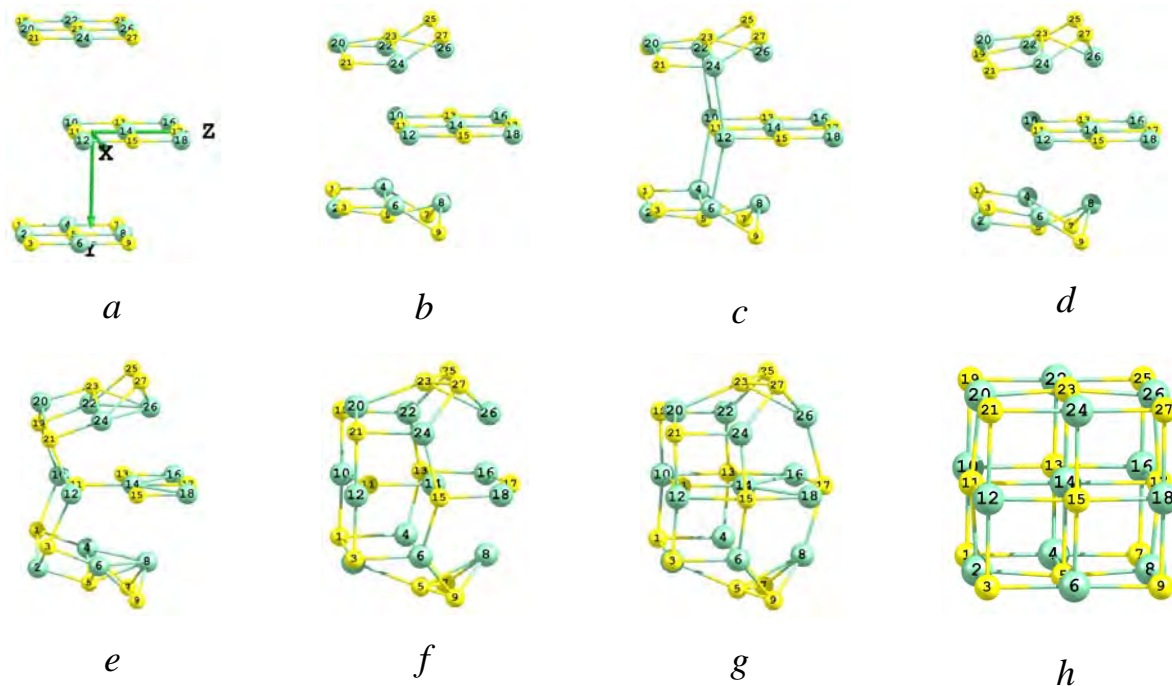
a – initial configuration; *b* - step 24; *c* - step 25; *d* - step 30; *e* – step 40; *f* - step 70; *g* - step 73; *h* - step 107, optimized structure

Fig. 63. Segmentation of planar fragments $Ti_4C_5 - Ti_5C_4 - Ti_4C_5$ (Dy = 0.4 nm, Dz = 0.1 nm) in a cubic nanocluster during geometrical optimization

A similar transition was observed also in the first variant (Fig. 62*d, e*). In both cases, these bonds were formed on one borders, then the fragments approached and bonds were formed on the opposite boundaries of the fragments (Fig. 63*f, g*). Then highly symmetrical cubic shape of the nanocluster was finally established.

In the ***third variant*** (Fig. 64) the segmentation of planar fragments $Ti_4C_5 - Ti_5C_4 - Ti_4C_5$ into cubic nanocluster $Ti_{13}C_{14}$ (3x3x3) was considered. However, unlike the previous case, planes (1) and (3) are shifted with respect to (2) by Dz =

+0.1 nm and Dz = – 0.1 nm, respectively. Offset along X axis was as before Dx = 0.4 nm.

And in this case the main role in segmentation is played by the interaction of "metal – metal" atoms of planes (1) and (3) with atoms of (2). The central fragment (2) no longer maintains the shape of the plane due to displacement of carbon atoms 13 and 17 (Fig. 64, *b* and *c*). The "skeleton" of cubic nanocluster (Fig. 63, *d* and *e*) is also formed mainly by long-range bonds of titanium atoms.
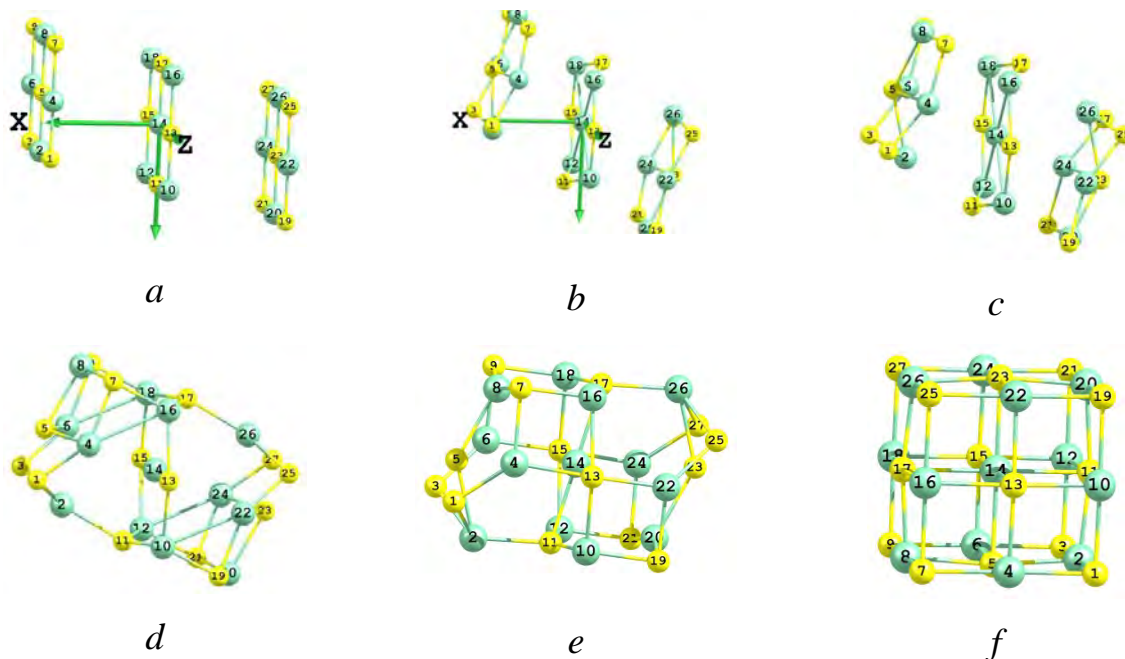
a – initial configuration; *b* - step 20; *c* - step 30; *d* - step 35; *e* - step 45;

f - step 82 - optimized structure

Fig. 64. Segmentation of planar fragments $Ti_4C_5 - Ti_5C_4 - Ti_4C_5$ (Dy = 0.4 nm, Dz = 0.1 nm) in a cubic nanocluster during geometric optimization

The ***fourth variant*** with the system Ti_5C_4 - Ti_4C_5 - Ti_5C_4 (Fig. 65) differs from the first in that the central plane (2) is shifted along the Z-axis relative to the planes (1) and (3) by 0.2 nm. Thus, the nearest neighbors of the upper boundary of planes (1) and (3) become a chain of atoms Ti – C – Ti in the center of plane (2). And in the first steps of optimization it can be seen (Fig. 65*b*, *c*) that the coupling of fragments (1) and (3) takes place with the center of fragment (2) due to metal - metal interaction. But after a few steps atomic configuration changes – fragment

(2) "is pushed out" along the positive direction of Z axis and, as can be seen in Fig. 65g, establishes Ti – C bonds of titanium atoms from the upper boundaries of fragments (1) and (3) with carbon atoms of the lower boundary of fragment (2). Lower boundaries of fragments (1) and (3) consist of the same type of atoms. The attempt to establish interaction between titanium atoms (Fig. 65*e*) is energetically less advantageous than their remote location (Fig. 65*f, g*). Optimized shape resembles the bucket. Central fragment (2) retained plane shape and the fragments (1) and (3) arranged symmetrically with respect to (2), changed their shape significantly.
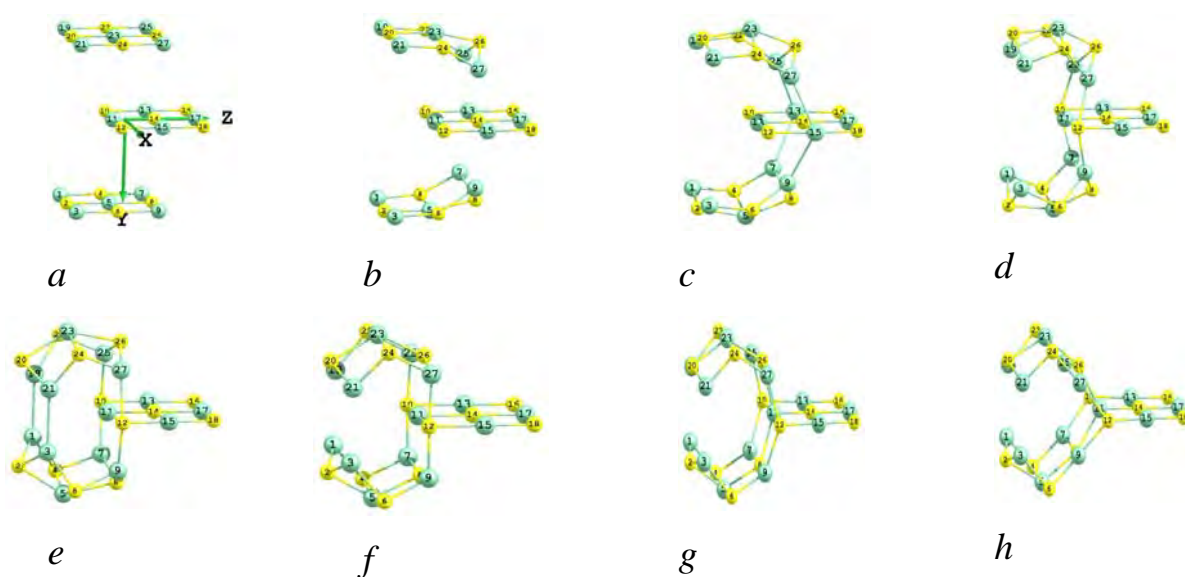
a – initial configuration; *b* - step 20; *c* - step 25; *d* - step 30; *e* - step 37; *f* - step 45; *g* - step 55; *h* - step 77 - optimized structure

Fig. 65. Segmentation of planar fragments Ti_5C_4 - Ti_4C_5 - Ti_5C_4 (Dy = 0.4 nm, Dz = 0.2 nm) during geometric optimization
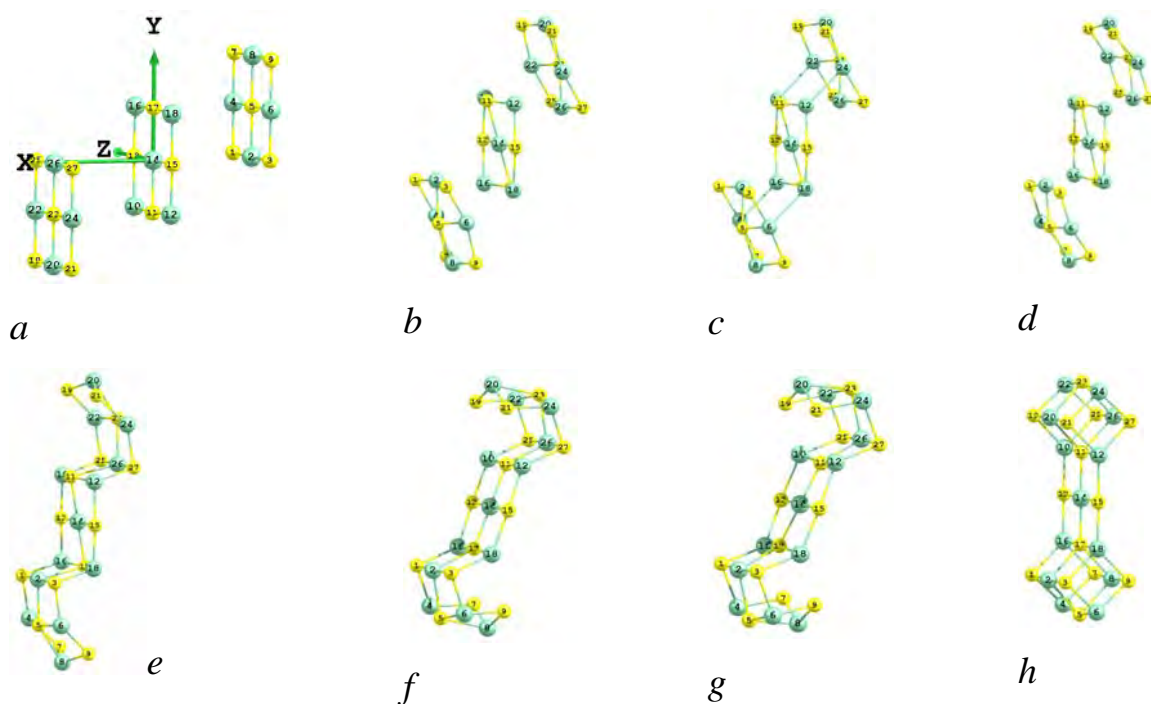
a – initial configuration; *b* - step 20; *c* - step 25; *d* - step 35; *e* - step 40; *f* - step 60; *g* - step 62; *h* - step 85 – optimized structure

Рис. 66. Segmentation of planar fragments $Ti_4C_5 - Ti_5C_4 - Ti_4C_5$ (Dx = 0.4 nm, Dy = 0.2 nm) during geometric optimization

Fifth variant of segmentation shown in Fig. 66, has an initial shape of fragments Ti_4C_5 - Ti_5C_4 - Ti_4C_5 similar to the third variant, but with a shift of planes (1) and (3) with respect to (2) by 0.2 nm. Shifting planes (1) and (3) along axis Z by a distance twice as much has led to the configuration where the nearest atoms of the upper boundary (1) and the middle (2) are the two pairs of carbon atoms and only one – of titanium atoms. This does not lead to the formation of bonds between them, and forces (Fig. 66, *b*) fragments (1) and (3) move toward the upper and lower boundaries of the fragment (2). Initially, metal atoms in the middle of fragments (1) and (3) are coupled with metal atoms at upper and lower boundary of fragment (2) (Fig. 66*c*). However, this configuration is unstable, established bonds are broken (Fig. 66*d*), fragments (1) and (3) are displaced even more (Fig. 66*e*) and a more advantageous belt-type configuration is formed. The process ends up by rounding of free boundaries of fragments (1) and (3) and their

coupling to the common chains of fragments (1) – (2) and (2) – (3). The last stage of the segmentation can be seen in Fig. 66*f*, *g*, *h*. The optimized shape resembles a dimer, it is symmetrical relative to the central fragment (2) which maintained a planar shape. Fragments (1) and (3) rolled up into distorted rectangles (2x1x1).

The conducted computational experiments show that the planar Ti_5C_4 and Ti_4C_5 nanoclusters under certain distance conditions can spontaneously segment into cubic nanoclusters $Ti_{14}C_{13}$ and $Ti_{13}C_{14}$. The process of assembly takes place exclusively due to the interatomic interaction of 9-atomic fragments with each other. Common to all variants is a long-range metal – metal interaction, drawing fragments to each other. Only after the fragments have shifted so much that can form a kind of "skeleton", the process begins of finding the most advantageous from the energy point of view configuration of the atoms. In the case, when the distance between the planes is about 0.4 nm, which is close to twice the length of the Ti – C bond in the bulk crystal, and a mutual shift in the direction perpendicular to the planes is in the range of ~ 0.1 nm (about half the length of the Ti – C bond in the bulk crystal), segmentation of planar fragments results in the formation of 27-atomic cubic nanocluster. With a larger shift (~ 0.2 nm) segmentation of fragments leads to non-cubic forms.

As a result of computational experiments a number of possible nanoclusters were obtained: two nanoclusters with the stoichiometric composition $Ti_{14}C_{13}$ with cubic symmetry (3x3x3) (Fig. 62*h*) and in the form of a "bucket" (Fig. 65*h*), as well as two nanoclusters $Ti_{13}C_{14}$ with the structure of a cube (3x3x3) (Fig. 63*f*, 64*h*) and "dimer" (Fig. 66*h*). Table 20 shows some of the structural and energetic characteristics of these nanoclusters. Note that the values of the lengths of Ti-C bonds in all four variants of clusters are quite close, and the ratio of maximum to minimum bond length is about ~ 1.08 – 1.09. Only for "bucket" cluster is this ratio slightly more – 1.11. The disbalance of bonds within the cluster can lead to the structural instability. In this sense, the least stable is a "bucket" configuration.

Table 20. Geometric and electron properties of segmented nanoclusters

Characteristic	$Ti_{14}C_{13}$ "cube"	$Ti_{14}C_{13}$ "cube"	$Ti_{13}C_{14}$ "cube"	$Ti_{13}C_{14}$ "димер"
Maximum length of Ti-C bond, nm	0.2158	0.2088	0.2194	0.2101
Minimum length of Ti-C bond, nm	0.1990	0.1874	0.2021	0.1943
Number of atoms with three C-Ti bonds	0	10	8	9
Binding energy, eV/atom	10.373	9.510	10.370	9.804
HOMO – LUMO, eV	0.666	0.392	0.716	0.573

Structural stability of the cluster is highly dependent on the amplitude of oscillations of the individual atoms or group of atoms. In the studied objects the most mobile are light carbon atoms that have three or four bonds with titanium atoms. Apparently, it is the triple bonds that are the least strong. A more rigorous analysis was carried out in [76] in the study of the stability of cubic nanoclusters $Ti_{14}C_{13}$, found experimentally and $Ti_{13}C_{14}$, not recorded in the experiments. The reason of instability of the latter is that the cluster contains eight carbon atoms located at the corners of a cube having three bonds with titanium atoms. In this regard it is useful to compare for the clusters considered the number of carbon atoms having three C-Ti bonds. From Table 20 it can be seen that the most stable structure is cubic nanocluster $Ti_{14}C_{13}$, in which all carbon atoms have four bonds with the atoms of titanium. Cluster "bucket" has 8 carbon atoms with triple C-Ti bonds, and two atoms (angular in the central planar fragment) have only two bonds with atoms of titanium. Estimates of the magnitude of the binding energy confirms the findings: highest binding force is in cubic structures and the lowest in "bucket".

If we assume that considered four types of nanoclusters are stable or metastable and may participate in the self-assembly of crystal structures, we can point out the possible ways of further segmentation of nanoclusters. For the cubic nanoclusters expansion of the form $Ti_{14}C_{13}$ - $Ti_{13}C_{14}$ in all three directions is obvious. "Bucket" nanocluster can be stabilized if the coupling of $Ti_{14}C_{13}$ - $Ti_{14}C_{13}$ will go on in such a way that the planar fragment (2) will enter into the gap between the fragments (1) and (2) and this will lead to the formation of new Ti - C

bonds. Planar fragment (2) also can become more stable if contact with the fragments (1) and (3) will take place. In this case, double C - Ti bonds will transform to triple. Such coupling increases the deficit of carbon atoms, but crystalline titanium carbides are known for their fairly wide range of homogeneity. Nanocluster "dimer" has two components of shape: planar fragment (2) and parallelepipeds Ti_6C_6 (2x1x1) formed from the initial fragments (1) and (3).

Ti_6C_6 nanoclusters have high symmetry and can be stable by themselves. Calculations of binding energy and of atomic oscillations showed that IR spectrum contains no imaginary frequencies, which confirms the stability of the Ti_6C_6 cluster. This means they can be "building blocks" during segmentation into the crystalline structure. Planar fragment (2) has probably the weakest bonds, where carbon atoms located in the center of the side edges each have three C - Ti bonds. Further segmentation and stabilization of "dimers" can occur, for example, when Ti_6C_6 nanoclusters are coupled in directions that allow formation of new C - Ti bonds. Besides, stabilization of fragment (2) is possible during extension of "dimer" – "dimer" perpendicular to its plane. Such coupling leads to the enrichment of the boundary carbon atoms by one bond with titanium atoms.

Conclusion

With the help of the program complex "Gaussian'03", in the approximation of density functional theory, computational experiments on the segmentation of carbide nanoclusters were performed for the first time. It was shown that even metastable planar forms of Ti_5C_4 and Ti_4C_5 type can spontaneously form nanoclusters $Ti_{14}C_{13}$ and $Ti_{13}C_{14}$ of various shapes (cube, "bucket", "dimer"), depending on the distance and relative orientation of free surfaces. Segmentation mechanism is due, primarily, to long-range interaction of metal atoms from different planes. After the formation of "skeleton" from metal atoms, formation of Ti - C bonds and final configuration takes place.

III. MEZOSCALE

8. Imitational modeling of the process of eutectic co-crystallization on the basis of the cellular automaton method.

Eutectic co-crystallization of boride-boride composites occurs at relatively high ($T_m \sim$ 2000–3000°C) temperatures and is associated with very specific physical conditions [81]. This necessitates the employment of the formalism of nonequilibrium thermodynamics and nonlinear equations in the mathematical models developed for the description of these processes. In the nonlinear thermodynamics, there is a convenient conventional approach, which uses the partitioning of all the space of the subject under consideration into a large number of "elementary volumes", each of them being specified with its own set of state parameters. Such an approach is analogous to the method of the imitational modeling known as "cellular automata" (CA) [82]. At present, there are practically no works, which would exploit this methodology for simulating real processes of crystallization. The available publications are mostly illustrative and aimed at the demonstration of the capabilities of the approach rather than solving actual specific problems [83]. In this work the CA approach is implemented for 2D imitational modeling of eutectic structures.

Developing the model

In order to define the "life" rules for CA, let us consider the simplified physical model of the crystallization process occurring in nonequilibrium dynamical conditions.

In the state of a melt, the processes of nucleation in the system are absent, as are the conditions needed to provide the crystal growth. The melt represents the uniform system described by the state parameters, which determine its behavior.

In the process of cooling the system, there appear local deviations of the average chemical composition (chemical fluctuations), or local changes in the temperature, pressure, etc. (the fluctuations of the state parameters of the system).

The occurrence of the local meta-stability in the system gives rise to the preconditions for the nucleation in the melt.

Within the local (physically microscopic) volume in the meta-stable state, i.e., far from equilibrium, there are two random processes possible, namely, the return to the average state of volume within the system ("dissolving" the fluctuations due to the diffusion, or relaxation of fluctuations), or the transition to a new quality, the formation of a solid nucleus.

The crystal growth and the formation of the inter-crystallite boundaries occurs from the "stable" nuclei of the leading phase.

On this basis, we can formulate the following stages of the CA development for the binary system to be modeled:

- onset of the crystallization process, i.e. the appearance of a fluctuation;

- diffusion between the elementary volumes;

- occurrence of the initial nuclei of the eutectic colony in the two-dimensional space;

- destruction or stabilization of nuclei;

- layered crystal growth;

- formation of inter-crystallite boundaries;

- termination of the process;

- formation of the stable (steady-state) microstructure.

To perform the numerical experiment, we chose the model sample based on the two-phase LaB_6–ZrB_2 alloy with fiber structure (Figs.67, 68).
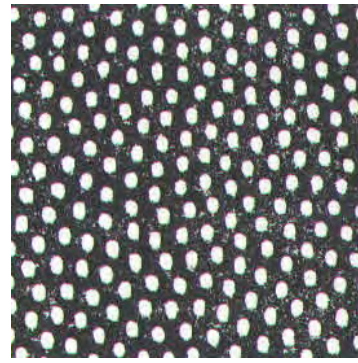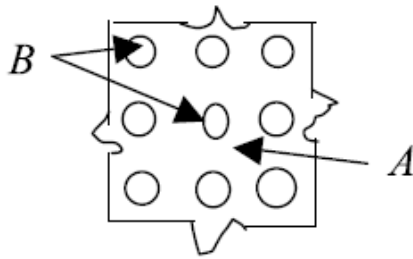
Fig. 67. Schematic of the composite to be modeled; here A and B are the components mutually insoluble in the solid state, *A* is the matrix (lanthanum hexaboride, LaB$_6$), and *B* is the fibered diboride phase (zirconium diboride, ZrB$_2$).

Fig.68. Cross-section microstructure of the directionally crystallized two-phase alloy LaB$_6$–ZrB$_2$ (micrograph obtained by scanning electron microscope «Stereoscan S4–10»[84].

The physical parameters of the sample of the material prototype are as follows: [81]:

- eutectic temperature at which the crystallization occurs: $T_E = 2740 \pm 40$ K;
- eutectic volume fraction for ZrB$_2$: $C = 16\%$;
- average fiber diameter: 0,2 – 1,0 micron;
- inter-fiber spacing: 0,8 – 1,2 micron.

As the result of the imitational modeling, the CA field filled with the cells of two types, A and B, should be formed, with the relevant structure and in accordance with the above physical parameters. Each cell type has to be specified via the vector of physical and chemical material parameters (density, specific heat, latent heat, heat and temperature conductivities, etc.), which are needed for further simulation.

The simulation has to be performed on the square CA field consisting of $n \times n$ cells (n is one of the basic model parameters), representing the cross-section of the sample. Every cell may occupy one of three states:

- empty cell (contains 0, associated with the melt);
- nucleus cell (contains the information about the nucleus and fiber);
- fiber cell (contains 1, associated with the solid phase B).

The evolution of CA field proceeds in two stages. At the first stage, there emerge B phase nuclei on the CA field. At the second stage, they grow and give rise to the formation of fibers. Within the proposed model, the fiber cross-section is assumed to be square.

The nucleus cell contains all the information related to the nucleus itself and, partially, to the fiber originated from it. The fiber cannot exist independently, without a nucleus. The nucleus cell contains the following data:

- x, y — nucleus coordinates in the field;
- *status* — nucleus state; can take three values:
  - ○ "n" —nucleus; the default value,
  - ○ "g" —growing fiber,
  - ○ "f" —full-grown fiber;
- *left*, *right*, *up*, *down* — the number of cells, which the nucleus did grow in the corresponding direction.

The nucleus can grow in any direction to form the fiber. The fiber can grow one cell left, right, up, or down per one step, while retaining the rectangular form. The fiber growth is limited by $f \times f$ size. f is one of the basic model parameters. The examples of the fiber growth are given in Fig. 69. Alternatively, the nucleus can "die". The fiber grown from it "dies" therewith as well; all the related information is deleted and all fiber cells are filled with zeros.
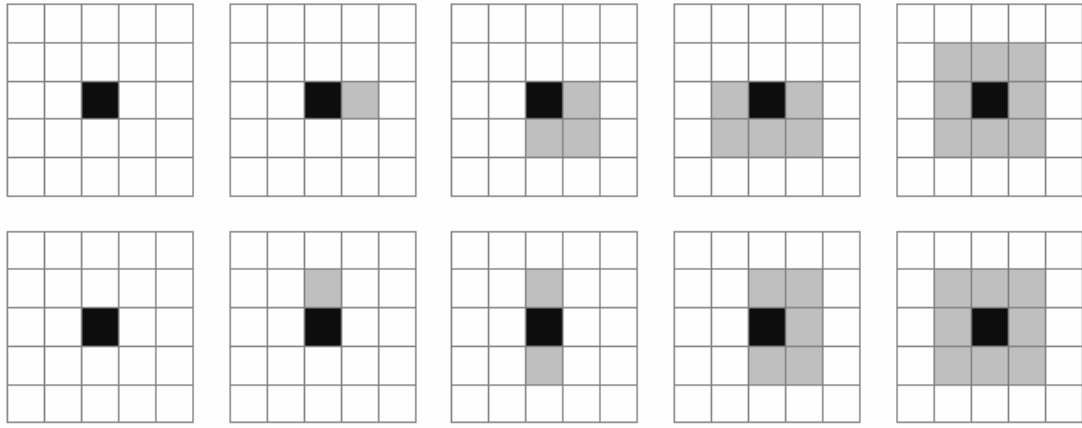
Fig. 69. Two possible implementations of the successive states in the process of fiber growth up to the 3x3 cell size. The nucleus and the growing fiber are shown in black and grey, respectively.

Some neighborhood near every nucleus or fiber is viewed as the "dead zone". The dead zone is defined by the following considerations: a) within the dead zone, no other nucleus can emerge; b) growing fibers cannot occupy the dead zone cells belonging the other fibers; c) dead zone width g is one of the basic model parameters. Within the framework of the model, it is allowed to set different dead zone widths on the stages of nucleation (g_1) and fiber growth (g_2).

A nucleus neighborhood of the width g is defined as the set of cells with the coordinates, which differ from the nucleus coordinates no more than by g in both directions. Therefore, the neighborhood of the nucleus with the coordinates (x_0, y_0) contains all cells with the coordinates (x, y) satisfying the relation

$$x_0 - g \leq x \leq x_0 + g$$
$$y_0 - g \leq y \leq y_0 + g$$

The fiber neighborhood of a radius g includes all cells with the coordinates, which differ from the coordinates of the *nearest fiber cell* no more than by g. Therefore, for the case that the nucleus has the coordinates (x_0, y_0) and did grow by

left, right, up, down cells in each of these directions, the neighborhood will be represented by the cells with the coordinates (x, y) fulfilling the relation

$$x_0 - left - g \leq x \leq x_0 + right + g$$
$$y_0 - up - g \leq y \leq y_0 + down + g$$

An example of the nucleus and fiber neighborhood is given in Fig. 70. In this model, the notion of the neighborhood is introduced for nucleus and fiber only. The neighborhood of an arbitrary cell is undefined.

a)   b)
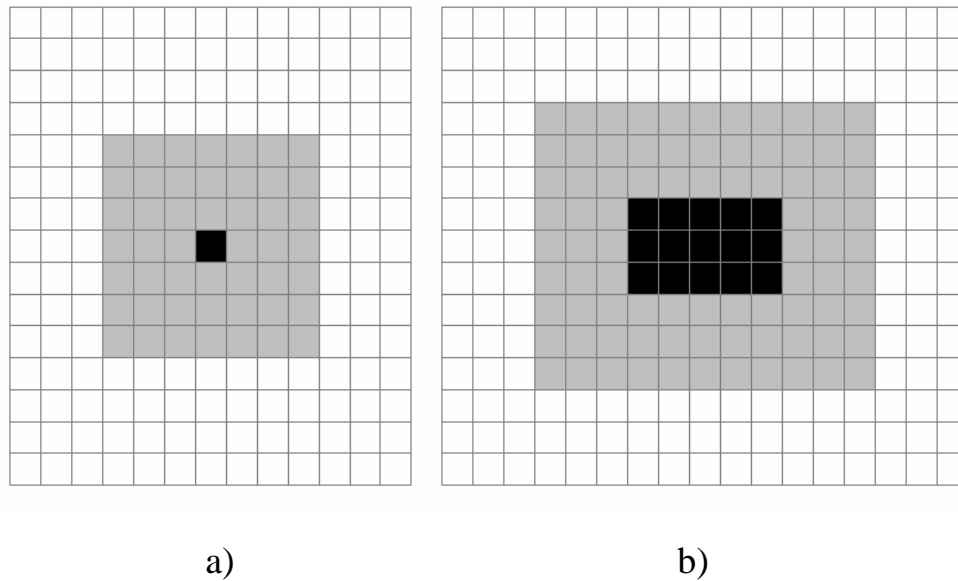
Fig. 70. Example of the nucleus (a) and fiber (b) neighborhood. The nucleus and the fiber are displayed in black and their neighborhood in grey, for $g_1 = g_2 = 3$.

Initially, the CA field is filled with zeros.

At the first stage, the nucleation on the CA field is modeled; an^2 attempts of seeding are made (a is one of the basic parameters of the model). The first stage of nucleation proceeds as follows: a random cell from the set, where the seeding yet not been attempted, is chosen; then, in this cell a nucleus is created. In the case that the nucleus appears in the dead zone of another nucleus, it dies immediately.

At the second stage, the revision of all the nuclei in the order of seeding is made. Such a revision repeats $2f - 2$ times. In the course of revision, an attempt for

every nucleus to grow by one cell is made. The direction of growth is chosen at random, with the following rules being fulfilled:

- as the result of the growth, the fiber should not occupy the dead zone of another fiber or nucleus;
- it should not leave the area of CA field;
- its size in both directions cannot exceed f cells.

In the case that there are no directions allowed for fiber growth, which would meet above conditions, and, at the same time, the fiber did not reach its maximum $f \times f$ size, it dies and is excluded from further revisions.

As the result of this process, there forms a number of square fibers of $f \times f$ cell size on the CA field. By using the number of the grown fibers, one can evaluate the concentration for the phase B as the ratio of the number of cells occupied by fibers to the total number of cells,

$$C = \frac{Nf^2}{n^2} \tag{83}$$

Description of the program

To implement the model, a program has been written by using the Python programming language. Pseudo-random number were generated by using the built-in generator "Mersenne twister". To visualize the cellular automaton, the well known library Matplotlib has been exploited.

Basic parameters of the model and program are as follows:

- n — field size.
- a — the ratio of the number of seeding attempts to the total cell number; in total, an^2 seeding attempts are made.
- f — size of the full-grown fiber.
- g — dead zone width:

○ g_1 — in the process of fiber formation;

○ g_2 — in the process of fiber growth.

The program is implemented as the library written in Python language. It has command line (not graphical) interface. The model can be launched by the regular library call, for instance,

```
import sys
sys.path.append ("[path to the "models" directory]")
from model6 import *
Model6(n = 300, a = 0.1, f = 8, g1 = 14, g2 = 7).run(step = 0.1, plot = True)
```

Such an approach simplifies the numerical experiment, because it enables one to start the model with different parameters and accumulate the results of the work. Alternatively, the program can be started by directly running the source code file model6.py; in this case the parameters have to be specified within the file itself (Fig. 71).

The process of nucleation can take long time. To indicate the progress, the program displays the intermediate results (the number of attempts and the nuclei seeded) with the period determined by the parameter 'step': the period is equal to $an^2 \cdot step$. At the stage of fiber growth, the program displays the intermediate results after each revision, namely, the current revision number and the current number of the fibers left. Then, the concentration of the fiber material is calculated in accordance with Eq. (83) and the field image is plotted. An example of the program output is given in Fig. 71.
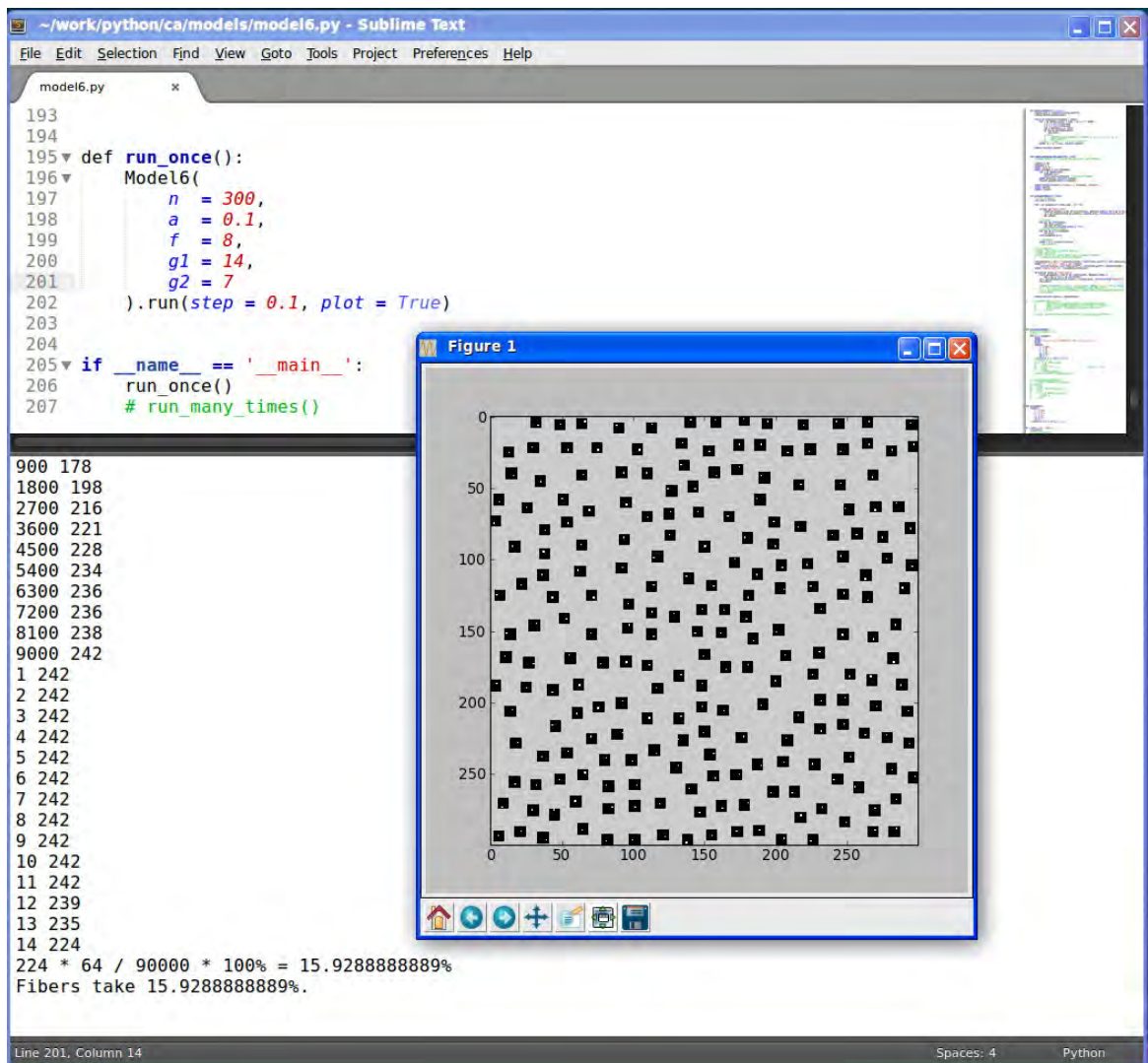
Fig. 71. The example of the program output started from the source code editor Sublime Text.

The program user has to specify, in first place, the value of the fiber concentration. For the eutectic composition of LaB_6–ZrB_2 , the latter amounts to 16%. After that, the initial values for basic parameters are set and the program gets launched. A good choice for the initial values are the ones given in Fig. 71. If the resulting fiber concentration is far from the desired value, the basic parameters have to be adjusted until the needed concentration is obtained. First of all, the parameters f, g_1 and g_2 should be varied. As was observed in practice, the value for g_2 must be close to $g_1 - f + 1$. Otherwise, the image of CA field gets essentially different from that given in Figs. 67 and 68.

The program has the option to vary the field size parameter n. With increasing n, the computational time grows rapidly. In order to reduce it, one can diminish the parameter a, which affects the number of seeding attempts. In so doing, it is desirable to keep the number of nucleation attempts an^2 much greater than the maximum number of nuclei to be seeded (the latter obtains at $a = 1.0$). Otherwise, the structure of CA field obtained in simulation will be different from the one needed. By using the personal computer of typical configuration, the reasonable computation time of the program corresponds to the numbers of n within the limit of 1000 cells.

Testing the program by varying the basic parameters

For testing purposes, the numerical experiment has need performed.

In particular, the effects of basic parameters on the final B phase concentration, the uniformity of fiber distribution, and the computational time has been examined.

Study of the boundary effects

According to the rules accepted within this model, there exists the minimum distance between nuclei/fibers, which is equal to g cells. At the same time, the rules do not limit the minimum distance between nuclei/fibers and the field boundary. This suggests that the fiber concentration near field boundaries can be higher than that at distance. This assumption is confirmed by the results of numerical experiment with varying the field size (see below). The elevated fiber concentration near field boundary is demonstrated by Fig. 71.

In the numerical experiment, the following notations were used (Fig. 72):

- d —*distance* from the given cell to the field boundary, exactly, the minimum distance between the cell and field boundaries expressed in the

number of cells. Therefore, for the cells located immediately on the field boundary, $d = 0$ (cells).

- *Layer* of cells at the separation d from the boundary is the set of all cells, for which d has the same value (i.e., equally separated from the field boundary).

The fiber concentration in the given layer is defined as the ratio of the number of cells in this layer occupied by the fibers to the total number of layer cells. The program has been restarted 100 times with the following parameters: $n=600$, $a=0.04$, $f=14$, $g_1=30$, $g_2=15$. In every run, a new field was obtained. For each field, the fiber concentration in each layer has been evaluated. After that, the concentration C averaged over all the results for the given d was calculated. The dependence of the average concentration C on the distance d is given in Fig. 73.
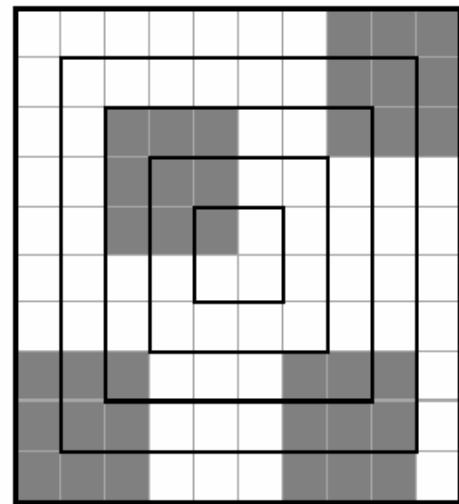
a)   b)

Fig. 72. Cell layers located at the given separation from the field boundary, by taking as an example the 10×10 cell field. a) the layers distinguish by colors, the values for d are given in cells. b) colors indicates the possible fiber configuration.
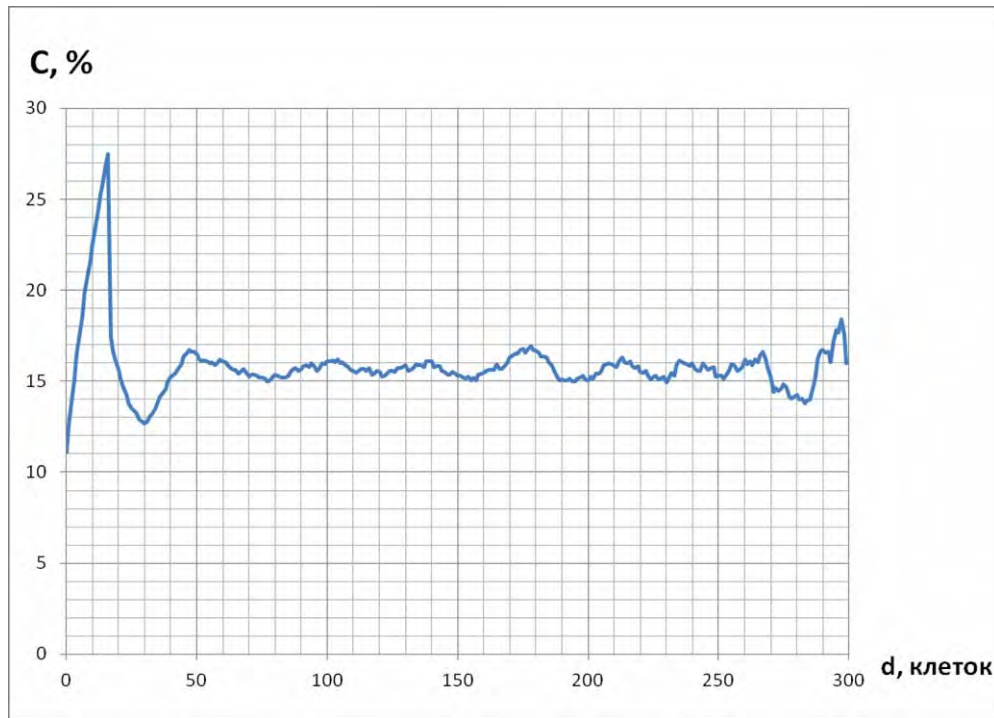
Fig. 73. Dependence of the B phase concentration on the separation from the field boundary.

The numerical experiment has confirmed the existence of the boundary effect. Considerable increase in concentration is observed near the field boundary. Starting from the field boundary, the concentration grows with the parameter d and reaches its maximum, which is 1,5 - 2 times greater than the average value. The peak is located approximately at the distance f from the field boundary. The peak is followed by the "gap", i.e. the fiber concentration reduces and becomes less than the average value, however, with the deviation much less than that of the peak. Further oscillations do not exceed the standard deviation for the concentration. The standard deviation increases while approaching the field center. Apparently, this is due to the reduce in the number of cells in the relevant layers. Thus, the layers which are close to the field center should be dropped in analysis.

Similar results were obtained for the other parameters ($n = 200$, $a = 1.0$, $f = 4$, $g_1 = 7$, $g_2 = 3$, 50 runs). The ways to diminish or eliminate the boundary effects require further refinements of the model proposed.

Investigation of the concentration dependence on the field size

To study the dependence of the B phase concentration on the field size n, a series of numerical experiments has been performed. The parameters were: $a = 0.2$, $f = 8$, $g_1 = 14$, $g_2 = 7$. The field size n has been varied within the range from 50 up to 1000 cells. For each value of n, there were made 10 program runs, and the results were averaged. The dependence obtained is given in Fig. 74.
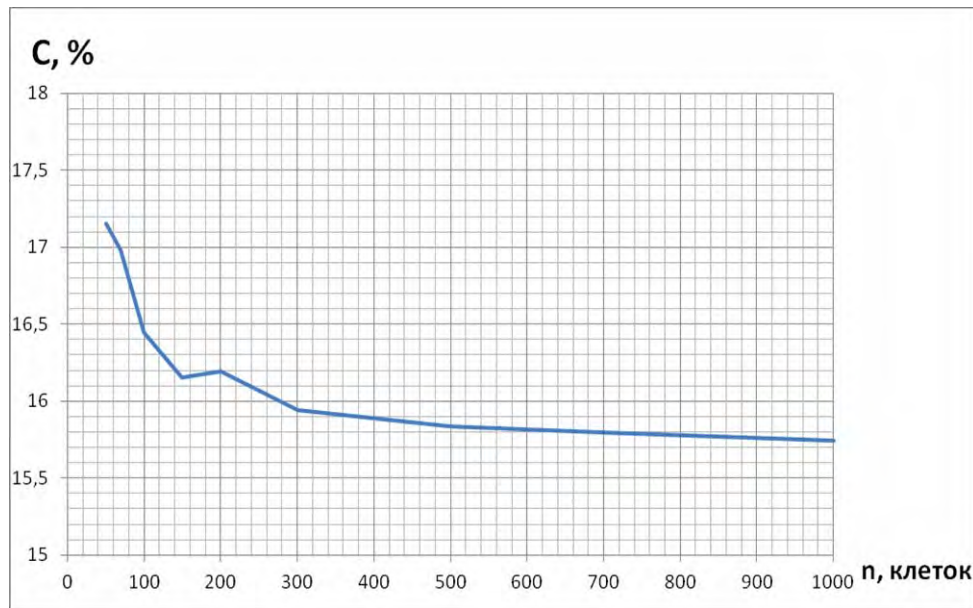
Fig. 74. Dependence of the B phase concentration on the field size.

The results of the numerical experiment have shown that the increase in the field size results in the moderate reduce of the B phase concentration. For larger field sizes, B phase concentration is nearly constant; the changes do not exceed the standard deviation. The standard deviation of the concentration decreases rapidly with growing n (presumably, in accordance with the hyberbolic law).

Study of the dependence of the computational time of the program on the field size

To examine the **temporal computational complexity** of the algorithm, a series of numerical experiments with the parameters $a = 1,0$, $f = 8$, $g_1 = 15$, $g_2 = 7$

was performed. The field size n was varied within the range from 50 to 800 cells with adjusting the values of n in such a way, that every next n was approximately $\sqrt[3]{2}$ times greater than the foregoing one. For every n within the limits from 50 to 400, 10 runs were performed, and for the values 500, 630 and 800 the program was run only once (per one value) in view of considerable increase of computational time.

The operation time of the program was determined by using the four core CPU AMD Athlon™ II X4 620 at the frequency 2,60 MHz (with the use of one core only). The averaged results of measurements are given in Table 21 and in Fig.75. The analytical approximation for the results of measurements has been derived, which indicates that the obtained dependence can be fitted well by the following relation:

$$t = Cn^{B+A\log_2 n}, \tag{84}$$

where $A = 0{,}2487$, $B = -0{,}5509$, $C = 9{,}1825 \cdot 10^{-3}$ c.

As is seen from Fig. 75 and Table 21, Eq. (84) approximates the experimental data rather well.

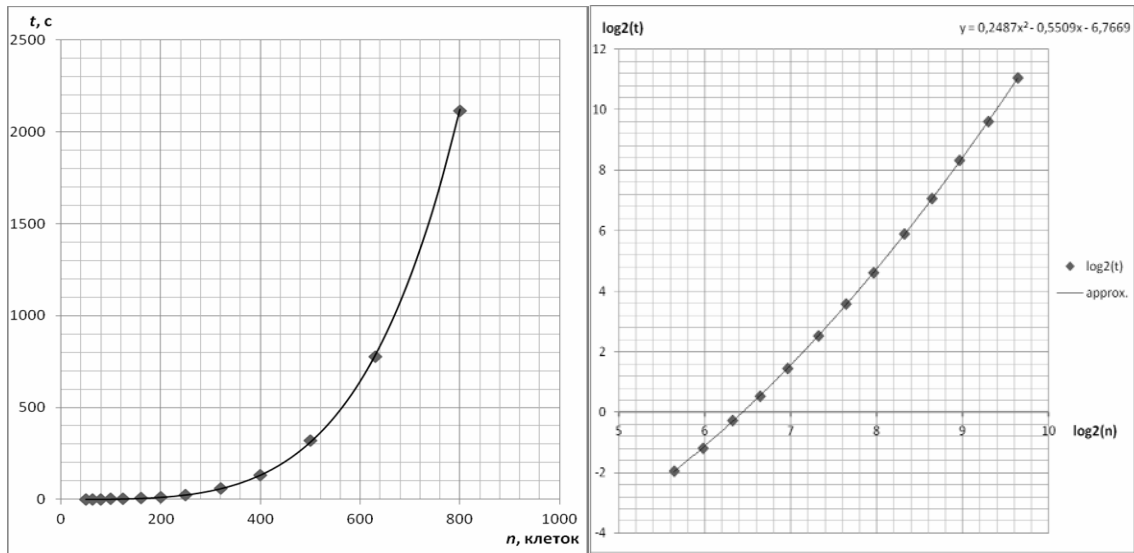a)   b)

Fig. 75. Dependence of the operation time of the program on the field size (the experimental data and their approximation according to Eq.(84)) on linear (a) and logarithmic (b) scale.

Table 21

a) comparison of the measured time with the fit;

b) predictions for the time by using Eq. (84) for the numbers in the range from 1000 to 10000.

n, cells	t, s	approximation for t, s
50	0,26	0,258059
63	0,44	0,443112
80	0,82	0,806692
100	1,45	1,464924
125	2,73	2,757022
160	5,76	5,785399
200	11,87	11,73934
250	24,56	24,68721
320	59,03	58,57217
400	133,36	132,8021
500	318,7	312,0586
630	778,4	785,0108
800	2113,3	2120,792

a)

n, cells	prediction for t, s	prediction for t in alternative units
1000	5568,428	93 minutes
2000	140268,9	39 hours
3000	1086524	12,6 days
4000	4987953	2 months
5000	16946530	6,5 months
6000	47270274	1,5 year
7000	$1,15 \cdot 10^8$	3,6 years
8000	$2,50 \cdot 10^8$	8 years
9000	$5,04 \cdot 10^8$	16 years
10000	$9,51 \cdot 10^8$	30 years

b)

The derived relation (84) indicates that the operation time grows drastically with increasing the field size. For the field size as much as several thousand cells, the operation time becomes impractical. The increase in computing capacity cannot remedy the problem. For instance, for $n > 1000$ cells, and for the given operation time, the 1000-fold increase in computing capacity enables one to increase the field size by less than one order. One should expect that changing the parameters will yield the similar results. Solution to the problem could be, probably, the optimization of the algorithm of nucleation.

Study of the dependence of operation time of the program on the parameter a.

As was demonstrated by the above mentioned experiment, the increase in field size results in rapid increase in simulation time. The examination of the functioning of the program has revealed that the most computational efforts are spent for simulations of the process of nucleation, whereas the nucleus growth is much less time consuming (the latter proceeds 2-3 orders more rapidly). Therefore, it is the nucleation process that should be optimized to make simulations more efficient. For instance, the nuclei can be generated in randomly selected cells only, instead of seeding every cell. For this purpose, we introduced the parameter a $(0 \leq a \leq 1)$ defined as the fraction of the cells, wherein the seeding was attempted. Thus, the nucleation requires an^2 attempts to be made. To make the simulation time reasonable, it is advisable to reduce the value of a with increasing the field size. It is natural to expect that the simulation time depends linearly on a (provided that the other parameters remain unchanged). To verify this assumption, the numerical experiment has been performed. The program was started with the following parameters: $n = 250$, $f = 8$, $g_1 = 15$, $g_2 = 7$. The parameter a varied from 0.0 till 1.0 with the increment of 0.1. For each a, the program has been repeatedly started 20 times. The averaged experimental results were used to plot the relevant dependence along with the approximation by the linear function (Fig.76). In doing so, the point $t(0)=0{,}04994c$ was regarded as being known and was measured independently.
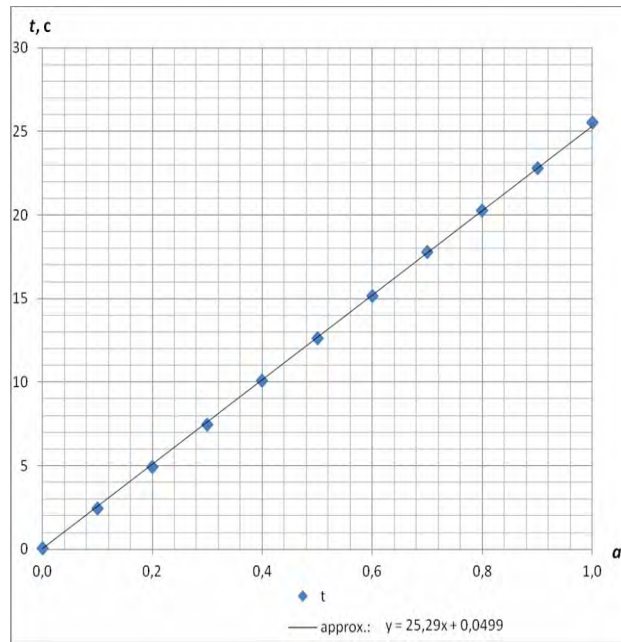
Fig. 76. Dependence of the operation time of the program on the parameter a along with the linear approximation.

As is seen from Fig. 76, the dependence $t(a)$ for given model parameters is well reproduced by the linear function starting from the point near the coordinate origin. It is natural to expect that the other parameters will yield similar results. Therefore, the model operation time can be assumed to be proportional to the parameter a.

It should be noted, that diminishing the parameter a results in decrease in the number of nuclei, and, as the consequence, in decrease of B phase concentration. To form the field with given concentration, the other parameters (f, g_1, g_2) should be adjusted.

Distribution of the number of nuclei

The results of numerical experiments for the same set of parameters differ because of the use of the pseudo-random number generator in simulations. To examine the distribution of the number of nuclei (at the nucleation stage; the growth stage was not considered), the following numerical experiment was performed. The program has been restarted repeatedly with the parameters n =

100, $a = 1{,}0$, $f = 4$, $g_1 = 7$, and the number of nuclei created was monitored. The total number of runs was 3238, and the results were used to plot the relevant bar chart (Fig.77). The following quantities were evaluated:

- Average number of nuclei: 103,51;
- Standard deviation: 3,35;
- Coefficient of asymmetry: 0,0343;
- Coefficient of excess: –0,0693.

The curve for the normal distribution (scaled by the factor 3238) with the same parameters is plotted in Fig. 77 as well. Fig. 77 demonstrates that the distribution of the number of nuclei is close to the normal one.
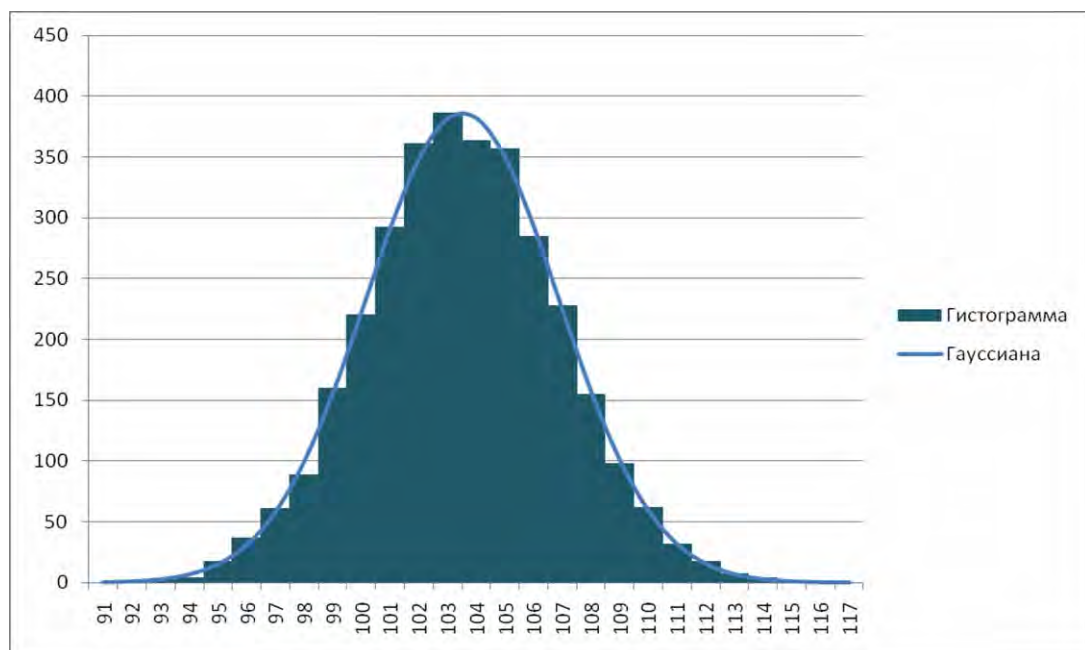
Fig. 77. Bar chart for the distribution of the number of the nuclei seeded in 3238 runs. For comparison, the Gaussian distribution (scaled by 3238) is displayed.

Visualization of the results of the numerical experiment

2D-visualization

In the present model, the fiber cross-section is assumed to be square. For the purpose of visualization, the question was considered as of replacing the squares by the circles of equal area, with the coinciding centers.

This feature was implemented by the Matplotlib library. An example for the program output for the parameters $n = 300$, $a = 0,1$, $f = 8$, $g_1 = 14$, $g_2 = 7$ is shown in Figs. 78, 79. In Fig. 78, the CA field with the square fibers is displayed. In Fig. 79, the same field is represented by the fibers with circle cross-sections. For better visualization of circles, the field size was scaled from 300×300 to 1500×1500, i.e. each single cell of the initial field was replaced by 25 (5×5) cells. A possibility is provided to specify the different field size, by using the optional scaling parameter z (which, in the case under consideration, is equal to 5).
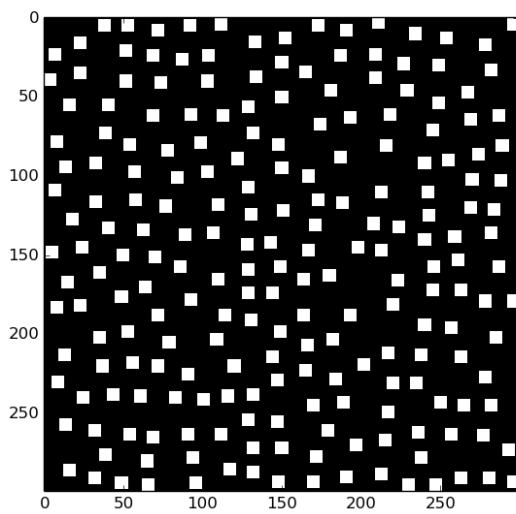
Fig. 78. Initial CA field. Fiber cross-section is square.
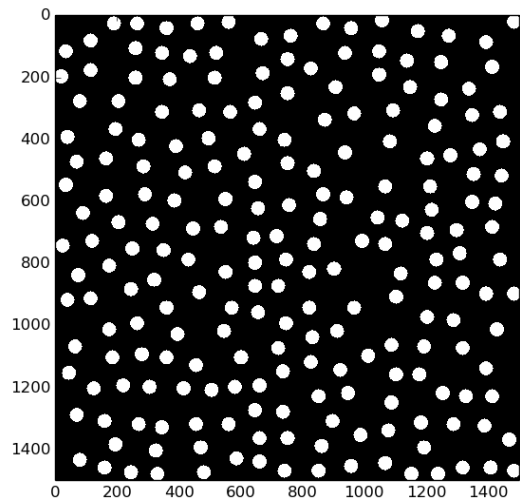
Рис. 79. Initial CA field. Fiber cross-section is circle.

3D visualization

For 3D visualization, we employed the Mayavi application, which can be used as a library and as an independent application.

By using Mayavi, starting from the initial CA field with the circle cross-sections of fibers (Fig. 79), the cylinders can be constructed, which imitate the configuration of fibers in a real sample (Figs. 80, 81). The height of the sample can be adjusted by the parameter h.

Рис. 80. 3D visualization of the initial CA field.

Рис. 81. 3D visualization of the initial CA field with plotting sample contour.

The Mayavi application has the option of changing the orientation of the 3D model (Fig. 82).

Рис. 82. 3D visualization of the initial CA field with plotting sample contour.

Conclusions

A model for imitational 2D simulation of eutectic structure formation based on the CA technique has been developed and implemented as a computer program. As the model sample, the two-phase alloy LaB_6–ZrB_2 was employed. The progr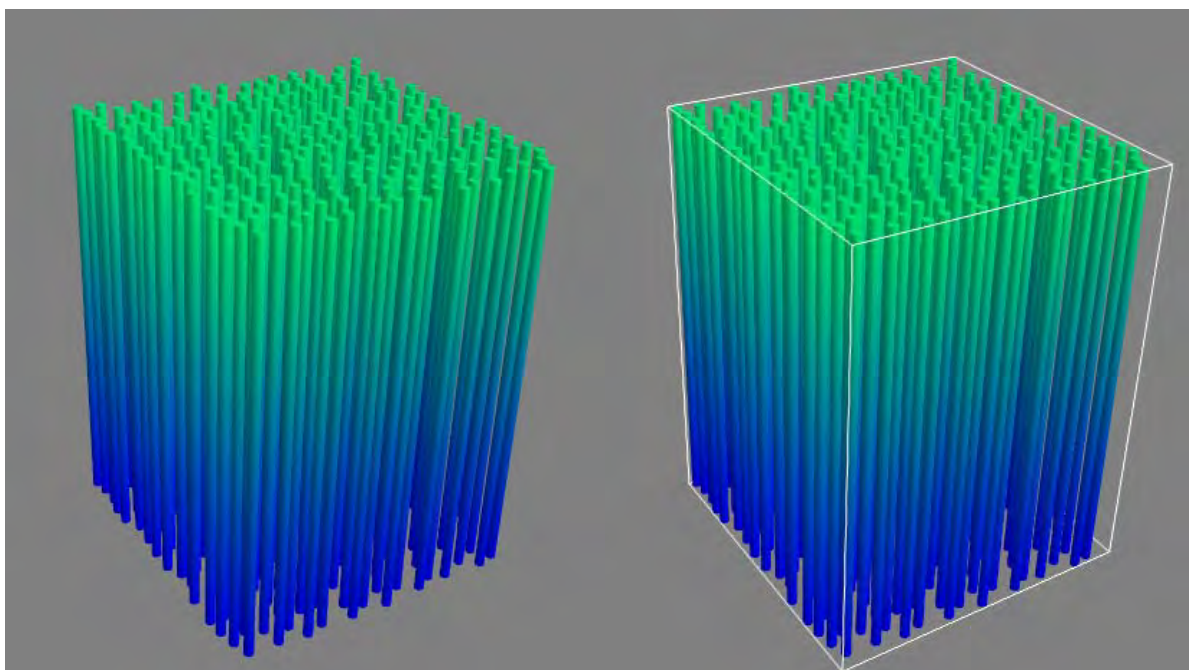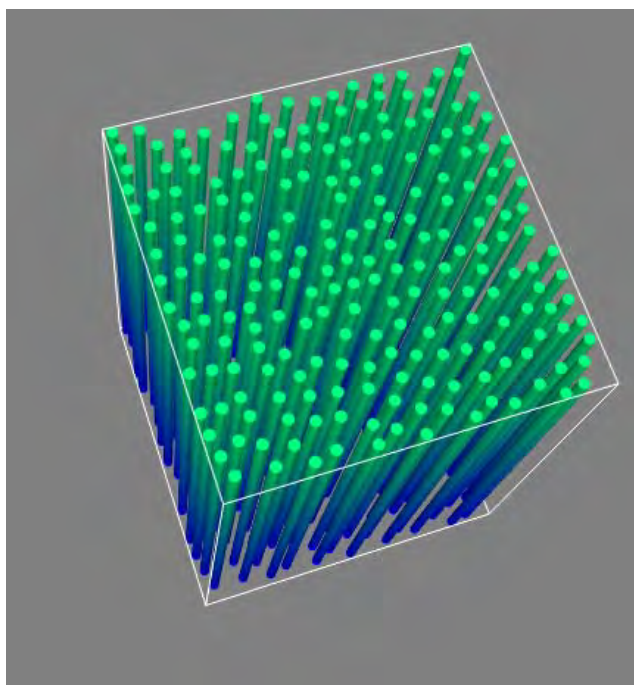am implementation of the proposed model is described. The basic parameters of the model are determined, and their effects on the structure formation are investigated. By means of numerical experiments, the ranges for the basic model parameters, which provide the adequate imitation of the eutectic structure formation, are established.

9. Fractal characteristics of the destruction surfaces

In the investigation of the deformation and destruction of materials, one of the important characteristics is the structure of the material itself. To describe the latter, in recent years, the formalism of the fractal geometry is employed [85-87].

However, at present there are no unified algorithms for calculations of fractal characteristics of materials available, in particular, for images obtained in various ways, such as, for instance, via the electron microscopy.

In our earlier investigations [88], we have shown that the programs widely used for evaluation of the fractal dimensionality have a number of drawbacks. These are, in first place, the high instability and sensitivity to image size.

In view of this, we have implemented the algorithm for calculation of the block (Hausdorff) fractal dimensionality and performed the investigation of the behavior of the program while processing both the artificially designed model images with pre-defined characteristics like Sierpiński carpet, and real images obtained by means of electron microscopy.

On the basis of the approach employed, an algorithm for calculations of the multifractal characteristics of two-dimensional images has been developed and implemented.

Algorithm for calculation of the fractal dimensionality of two-dimensional images

The analysis based on the formalism of fractal geometry plays an increasingly important role among the mathematical models [85-87, 89-90].

Since the 1980s, the notion of fractal structures, or fractals, gained wide acceptance among researchers.

The entities, which can be characterized by fractional dimensionality of their spatial components, are called fractals. The objects with the fractional geometrical dimensionality gained the attention of mathematicians since the beginning of 20th century, however, they did not find any practical application in physical and chemical investigations. The interest in fractal structures has been awakened after the publication of Mandelbrot's monographs [91, 92], where it was shown that the vast majority of natural systems can be regarded as fractals. The adoption of the notion of fractals made possible a deeper insight into the structural organization of various physical and chemical systems, as well as the regularities of diverse processes occurring therein.

There are several ways of defining the fractal dimensionality. From the viewpoint of mathematics, these definitions are not equivalent. The details concerning the introduction of the fractal dimensionality, can be found in one of the most cited monographs in this area [87].

The evaluation of the **block fractal dimensionality** can be described briefly as follows. Consider a set P of points in Euclidean space with the dimensionality E (in the case of plane images $E = 2$). The fractal dimensionality of P is evaluated by means of the following procedure. Let us cover the set of points by the net of E- dimensional cells of the size Δx, and denote the number of the cells containing at least one element of the set P as $N(\Delta x)$. The sought-for block fractal dimensionality D_B of the set can be derived from the relation $N(\Delta x) \square \Delta x^{-D_B}$.

This approach for defining the fractal dimensionality directly relates to the classical definition of fractal dimensionality, which is accepted as the basic one in [93]: the fractal dimensionality of any physical object can be found from the relation $d_f = \lim\limits_{\delta \to 0} \dfrac{\ln N(\delta)}{\ln(1/\delta)}$, where N is the number of blocks (spheres) of typical linear size δ, which completely cover the subject under consideration.

In the case of a two-dimensional black and white image (which is the case typical for electron microscopy), the set P is represented by the image itself, and the net of cells is nothing but the partitioning of the image into the squares. Since the simplest way to obtain the fractal dimensionality D_B is the least square technique applicable to the linearized expression $\ln N \square -D_B \ln(\Delta x)$, it is desirable that the values of $\ln(\Delta x)$ would be distributed uniformly. In other words, if we are going to obtain M experimental points of the function $\ln N = f(\ln \Delta x)$, then the relevant values for Δx should be

$$\Delta x_i = \left\lfloor e^{\frac{\ln S}{M-1} i} \right\rfloor, \quad i = \overline{0, M-1},$$

(85)

where S is the maximum image size in pixels, M is the total number of points. Notice that the actual total number of points may be less than M in the case that rounding off will yield equal values of Δx_i for different i.

Technically, it is more efficient to consider the quantity $2 - D_B$, i.e., in order to determine the fractal dimensionality, the dependence $N(\Delta x)\Delta x^2 \square \Delta x^{2-D_B}$ (or, in linearized form, $\ln N\Delta x^2 \square (2 - D_B)\ln \Delta x$) should be employed.

Computer implementation of the algorithm and the study of its properties

Description of the program for determining the block fractal dimensionality of two-dimensional images

The program for processing the images obtained from the electron microscope based on the above technique for determining the fractal dimensionality is written in the programming language Open Watcom C++ (http://www.openwatcom.org) with the use of the library wxWidgets (http://www.wxwidgets.org). Both of these products are freely distributed as open-source programs; in addition, they both allow the compilation of the applications for Windows, OS/2 and Linux operating systems. Thus, the program developed can be, in principle, transferred to any of the above listed operating systems. At present, it operates under the system MS Windows (it is verified and tested under MS Windows XP и Windows 7, although there are no any specific requirements for operating systems).

Presently, the developed program provides the evaluation of both block and mass fractal dimensionality. The overall appearance of the program window is given in Fig. 83.

The program enables one to set, prior to computations, the global tunings (which are saved in registry file and, therefore, remain valid for subsequent program runs), as is shown in Fig. 84.

The first global setting is the selection of the algorithm (block or mass) for calculations, the second one is the number of points of experimental curve. The calculation of the derivative of the experimental curve (which is, in fact, the basic issue for the evaluation of fractal dimensionality) can be based on the algorithms for calculation of the derivative by means of constructing the finite-difference scheme, with the use of three or five points. The last parameter specifies the units, which are used to set the threshold for transforming the images into the black and white mode (the meaning of this parameter will be considered in details below).
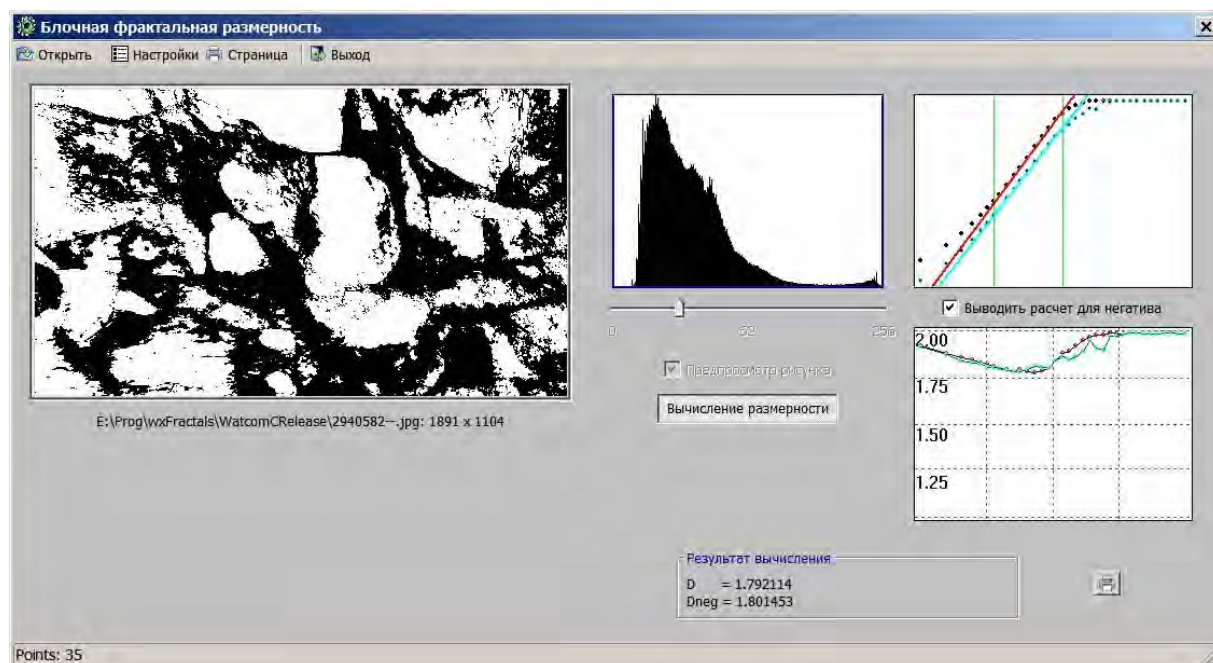
Fig.83. Overall look of the window of the program for computing the fractal dimensionality of images.

Fig.84. Window of global settings of the program for computing the fractal dimensionality of images.

The program works as follows. After selecting the global settings (or, if you don't open the settings window, accepting the previous ones), you open the image file (the basic graphical formats, BMP, GIF, JPEG and TIFF, are supported). If the file relates to the color image, it transforms to the grayscale format according to the conventional algorithm implying that a pixel with red, green, and blue, accordingly, R, G, and B, is replaced by the pixel from grayscale with the value $0.299 \times R + 0.587 \times G + 0.114 \times B$ (as recommended by ITU-R BT.601). A bar chart indicating the number of pixels with different brightness is displayed.

Then the image is transformed to black and white mode (1 bit per pixel), which provides the basis for further computations. Here one can control the process of transformation by setting the threshold value (in percentage or absolute values, from 0 to 256); all the pixels with the brightness exceeding the threshold, will be transformed to white, and those below the threshold, - to black colors. The choice of the threshold value is made using a slider; if the flag of preview is herewith set on, the resulting (scaled) image for the given threshold is displayed.

On the first image load, the program evaluates the recommended threshold value (which will be discussed in detail thereafter). According to our practice, such a recommended value turns out, as a rule, to be the best one.

A possibility of grayscale to black and white image transformation with the use of two threshold values is considered in [94]. In doing so, all shadowed points, which get between these thresholds, become white, while the others are transformed to black. There is a number of alternatives for image transformation, however, the choice there is based on the knowledge of specific subject (namely, which specific image details are important; what is to be stressed; what is to be removed from the image, etc.). For this reason, such transformations are irrelevant in the program aimed at the generalized determination of the fractal dimensionality of images; they should be implemented in other programs for the operation with the graphical information specific for the problems of analysis of images obtained from the electron microscopy.

The button "Evaluation of dimensionality" starts the processing of the image in accordance with the selected (block or mass) algorithm. As the result, one obtains two curves, $\ln N\Delta x^2 \Box (2 - D_B)\ln \Delta x$, or $\ln\left(r^2/M(r)\right) \Box (2 - D_M)\ln r$, as dependent on the algorithm used, and the associated derivative curve for this function (see Fig. 83). As is seen from the figure, each plot contains two curves, and, in addition, there is a switcher "Display the calculation for the negative". This switcher indicates that the calculation is performed for two cases. In the first case, the set P is represented by black points in the transformed image, and in the second case P is the set of white points. As a rule, if the threshold value is close to the recommended one (which corresponds to the case that the numbers of black and white points are approximately equal), the curves obtained for the positive and negative turn out to be sufficiently close to each other.

By double-clicking the mouse, the user can specify the left and the right boundaries of the range, where the numerical value of the image fractal dimensionality should be calculated (i.e., where the curve is as close as possible to the straight line; actually, these are the points, where the derivative reaches its extremum, and the second derivative turns to zero).

The calculated values are displayed on the screen, and the print button enables one to send the report to the printer. In the last versions of the program, at this stage the program estimates the supposed range for calculations and offers it the user.

While evaluating the block fractal dimensionality, the question may arise, what should be done in the case that due to the box size, the complete covering of the image is impossible (i.e., a portion of boxes on the boundary gets outside the image). In this case, we employed the following technique: while scanning the image from the left to the right and from the top to the bottom, the program takes into account only the boxes, which completely fit into the image. Next, the procedure repeats in the opposite direction, i.e., from the right to the left and from the bottom to the top. After that, the obtained results are averaged.

The results obtained in processing of real images demonstrate, that such a solution for the above issue is reasonably justified. In Fig. 85, the curves obtained for the same image of 1024×1024 pixel size are shown. On the left, the curves for the boxes of $2^i, i = \overline{0,10}$ size are plotted, which completely fit into the image. On the right, the number of points is increased up to 14, therefore, the boxes are used, which get outside the image. As is seen from Fig. 85, the obtained curves are identical. Therefore, the processing method, which was developed and employed in the program, is quite acceptable and adequate for the problem under consideration.
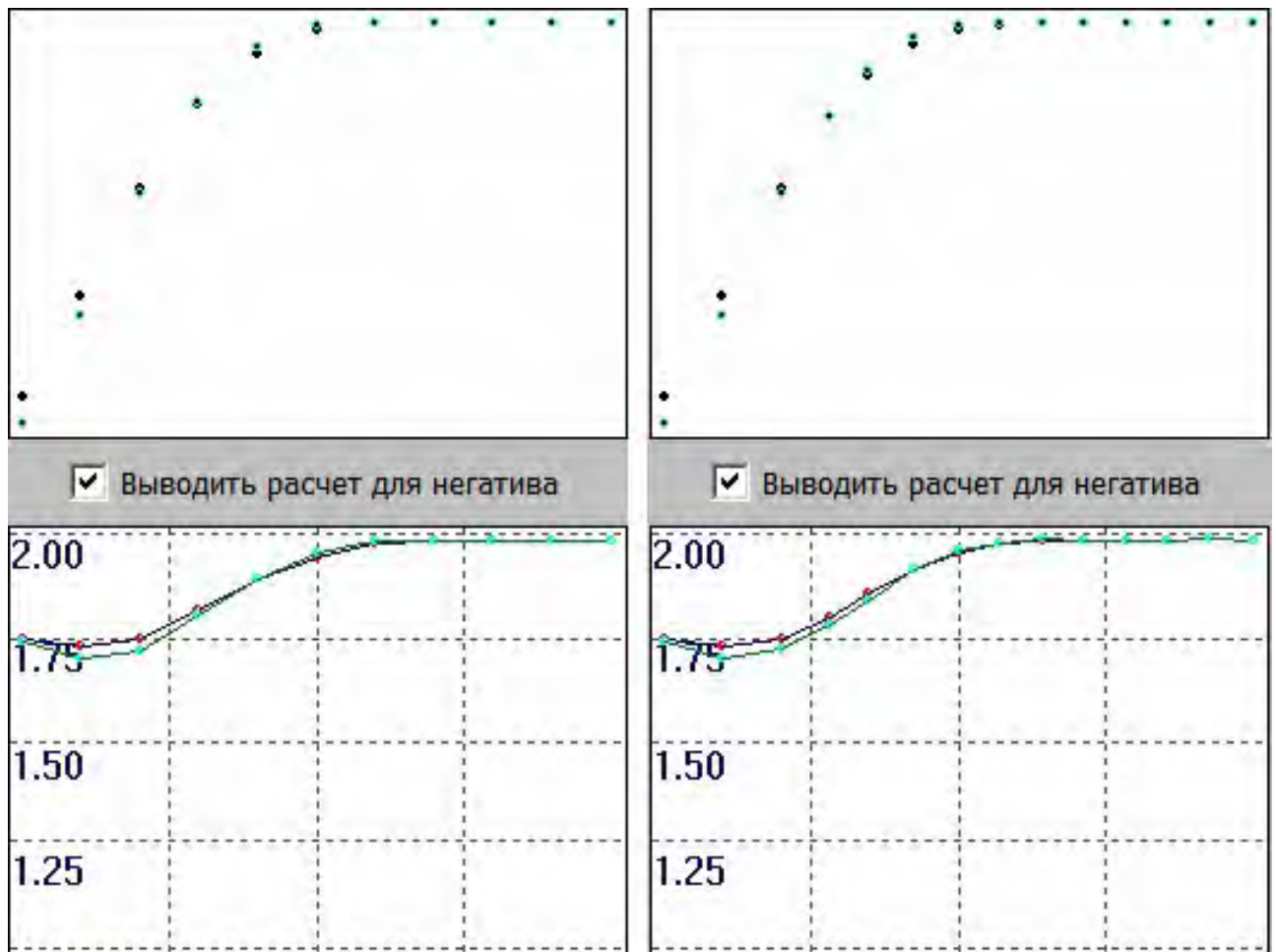

Fig. 85. Results of calculations for the boxes which completely fit (left) and do not fit (right) into the image.

Study of the stability of the developed software

As is known from practice, the programs for obtaining the fractal characteristics do not always provide the stable, exact and reliable results [88]. In view of this, we performed a number of investigations of the program developed. The need to have an a priori exact information about the fractal properties of the subject under examination has pre-determined the Sierpinski carpet as the model subject (Fig. 86) with the fractal dimensionality $D_0 = \ln 8 / \ln 3 \approx 1.8928$.
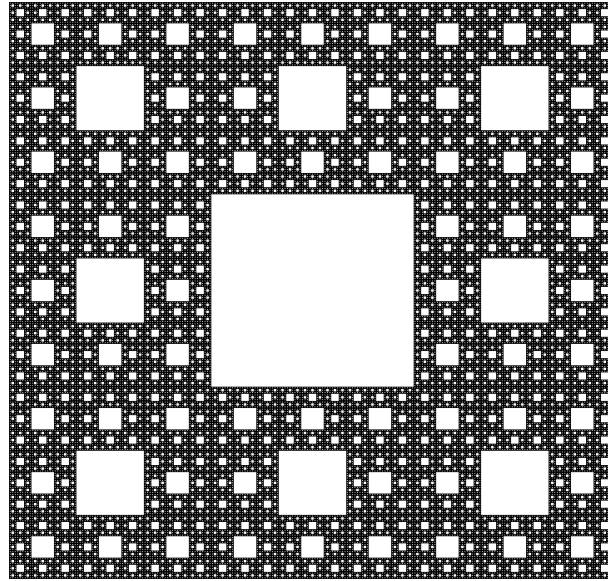
Fig.86. Sierpinski carpet; the fractal dimensionality is $D_0 \approx 1.893$

The first test was aimed at the study of the effect of the number of included points on the results of calculation. Since the range of the number of points should be in this case as wide as possible, we took as the model the image of 6561 x 6561 pixel size. The results of the experiment are given in Fig. 87. As can be concluded from the figure, the effects of the number of experimental points on the dimensionality are insignificant.
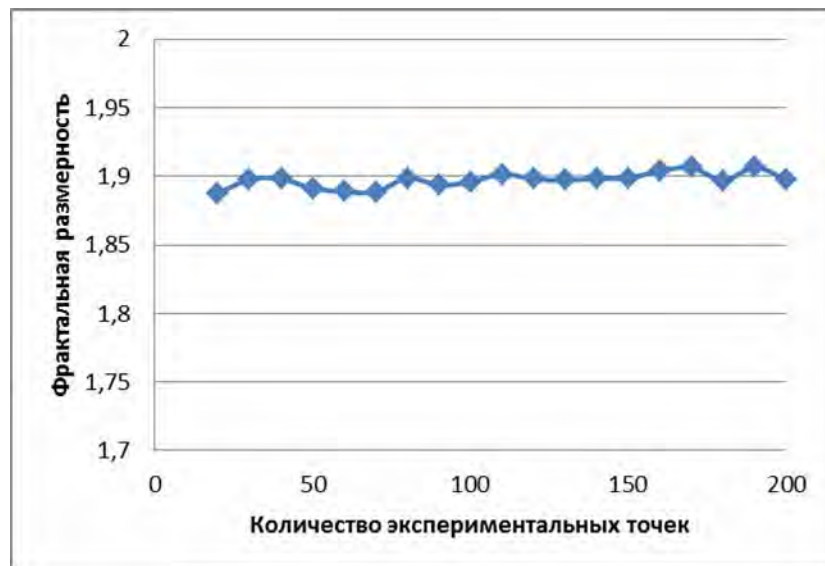
Fig. 87. Dependence of the measured fractal dimensionality on the number of the experimental points.

The next experiment consisted in examination of the effect of the cyclic displacement of the image on the fractal dimensionality. In this case we used the Sierpinski carpet of smaller size, 2187 by 2187 pixels. As can be seen from the results of the numerical experiment given in Fig. 88, the influence of the displacement of the image on the calculated fractal dimensionality is rather weak and irregular.
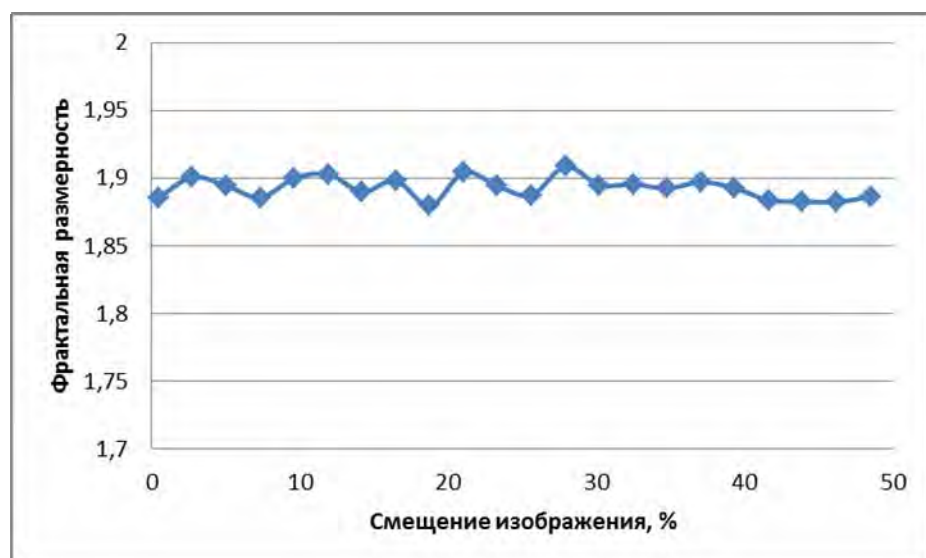

Fig. 88. Dependence of the measured fractal dimensionality on the displacement of the Sierpinski carpet.

For real images obtained via electron microscopy, it is often only a portion of the image which is of interest, as, for instance, in Fig 89. For this reason one more numerical experiment was the arbitrary random "whitening" of a portion of the Sierpinski carpet with subsequent examination of the effects of the size of this portion on the obtained fractal dimensionality.
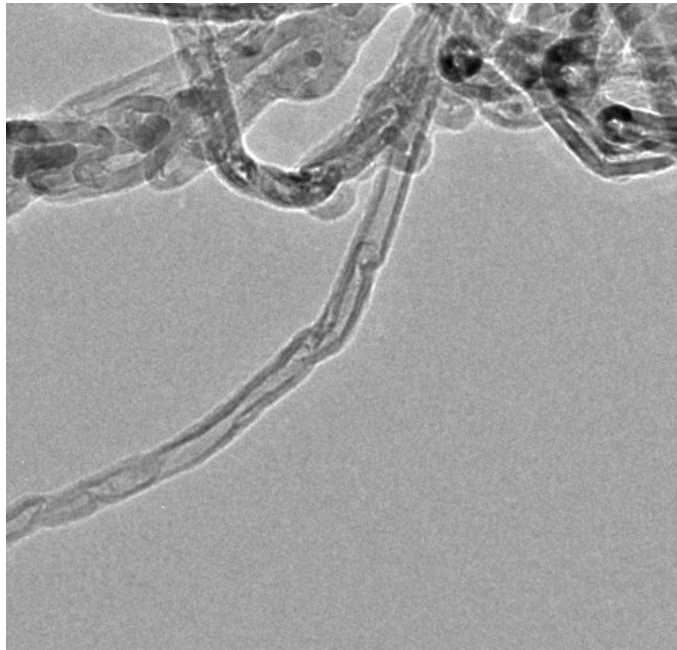
Fig. 89. Example with the subject occupying only a small portion of the image.

In this case, as is seen from Fig. 90, we observe a strong effect on the calculated fractal dimensionality for large areas of filling, larger than 80%. However, a closer inspection of experimental data of such images discovers that there are *two* linear portions on the curve $\ln N \Delta x^2 (\ln \Delta x)$. As an example, in Fig. 91, the experimental data for Sierpinski carpet 80% filled with white color are shown. The fractal dimensionality of Sierpinski carpet is associated with the curve of less steep slope.
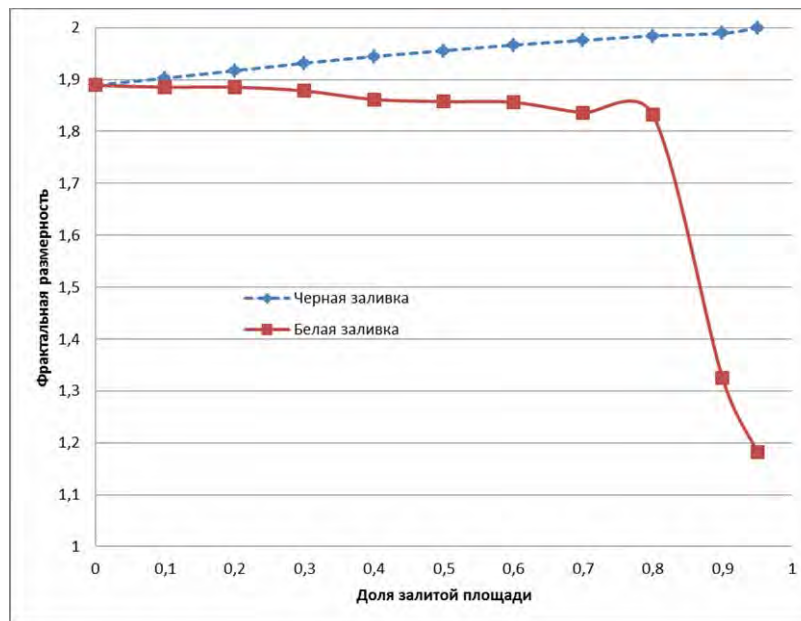
Fig. 90. Effect of the filling a portion of the image area on the magnitude of the fractal dimensionality.
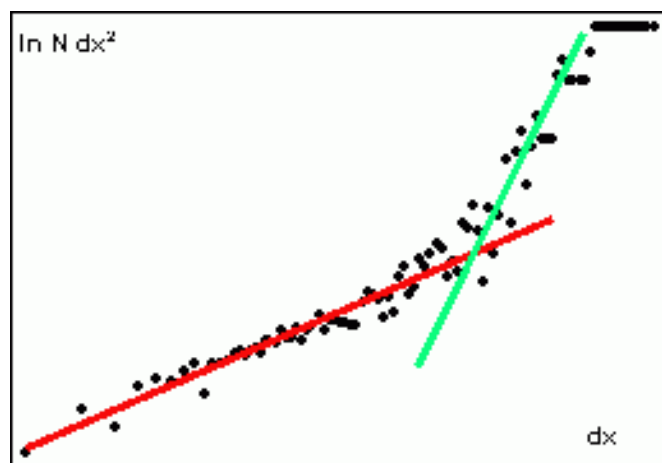
Fig. 91. Experimental data for the function $\ln N\Delta x^2 (\ln \Delta x)$ for Sierpinski carpet 80% filled with white color.

Thus, even in the case that the subject to be examined does not occupy the whole image field, we can still determine its fractal dimensionality provided that the associated range of fractality can be identified.

This result has one more consequence for the program, which we elaborate. At present, we implemented three versions of the automatic selection of the range for evaluation of fractality: by searching the minimum value for fractal dimensionality; by removing the horizontal portions of the curve $\ln N\Delta x^2 (\ln \Delta x)$

(which are associated with fractal dimensionality equal to 2); and by identifying the range where the points yield the maximum for the coefficient of linear correlation. However, the possible presence of several linear portions in the experimental function $\ln N\Delta x^2 (\ln \Delta x)$ makes practically impossible the complete automation of the computation of fractal dimensionality without controlling it by user. In view of this, the option for selection of the automated determination of the fractality range is provided in the program.

One more idea was inspired by the operation with the images similar to the one shown in Fig. 89. It concerns the possibility of compiling the image with the minimized non-informative component, even at the cost of moderately reducing the image size. To simulate such a treatment with Sierpinski carpet, we performed the following numerical experiment. The initial Sierpinski carpet of 6561 by 6561 pixel size has been sectioned into the parts of a given size, which were then mixed up at random by using the algorithm presented in [95]. After that, the evaluation of the fractal dimensionality and the range of fractality was performed. The results of this experiment are given in Fig. 92.
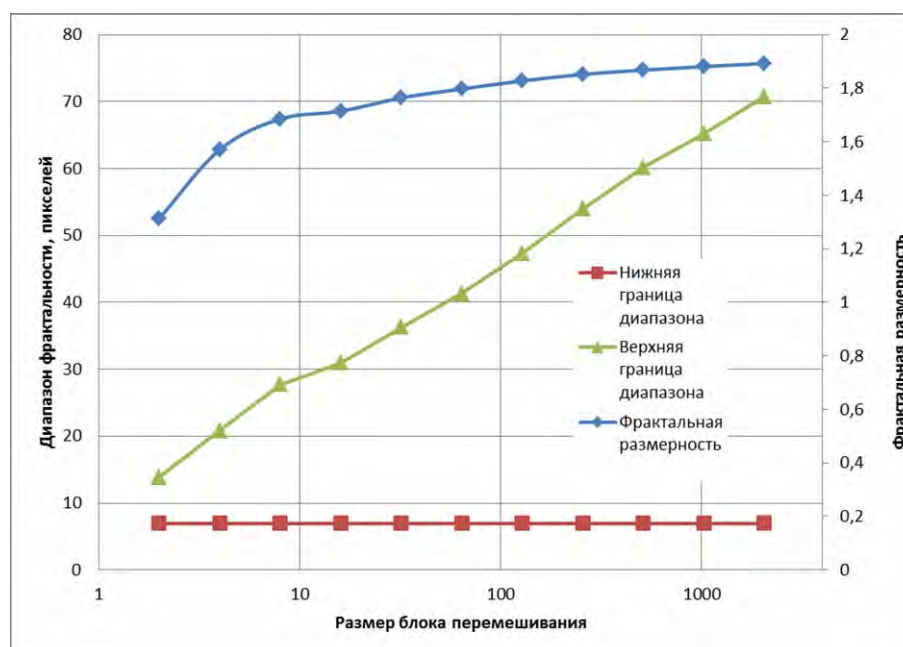

Fig. 92. The results of the experiment with the random mixing of the blocks of the Sierpinsli carpet.

As one would guess a priori, such a "mixed up" image should lose the information about its self-similarity with reducing the block size; this is fully confirmed by the experiment, which suggests that the upper limit of the range of image fractality is with good accuracy proportional to the logarithm of block size. As for the fractal dimensionality, it considerably depends on the block size as well, and, in the case of small blocks, is much less than its theoretical value. Therefore the above treatment based on putting together all the subjects to be examined in one image turns out to be a poor solution to the problem, since it can influence the subject characteristics to be evaluated.

Further experiments similar to those performed in the study of the program MFRDrom [88] are aimed at the elucidation of the effects of size and orientation of Sierpinski carpet on its fractal dimensionality.

The effect of the size of Sierpinski carpet on its fractal dimensionality obtained in computations is demonstrated in Fig. 93. It should be noted that, along with size, the number of experimental points are of importance. For example, it is physically impossible to obtain more than 27 experimental points for Sierpinski carpet with 27 pixels on a side. Actually, for this size the non-horizontal portion of the curve contains 8 points. The change of the range in one point only considerably influences the fractal dimensionality evaluated. According to our estimates, more or less reliable characteristics can be obtained only for the images with at least 500 pixels on a side.
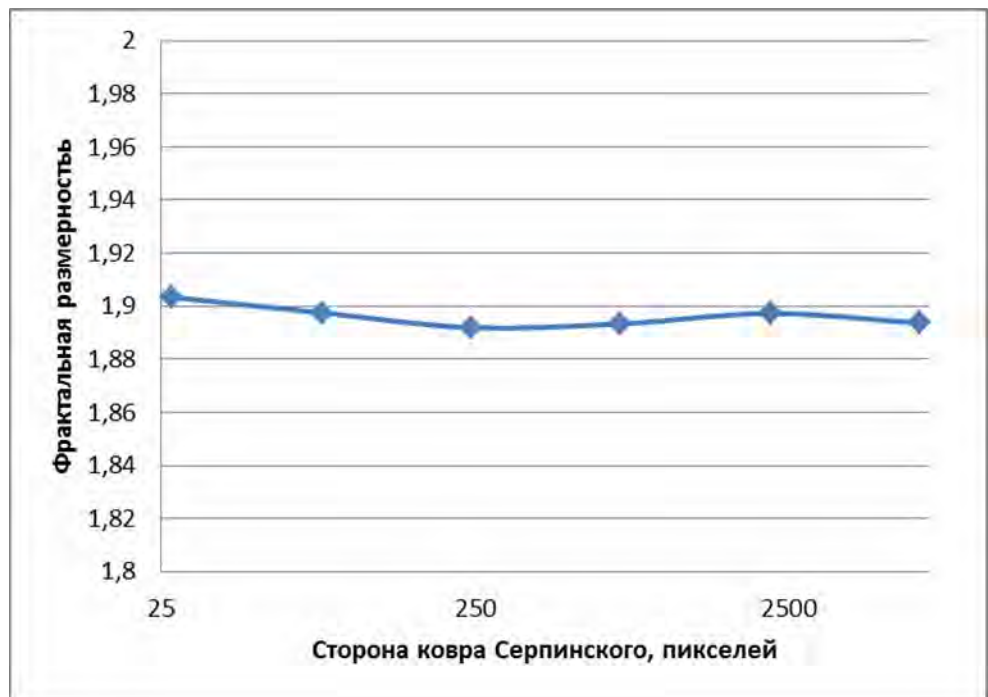
Fig. 93. Effect of the size of Sierpinski carpet on the calculated fractal dimensionality.
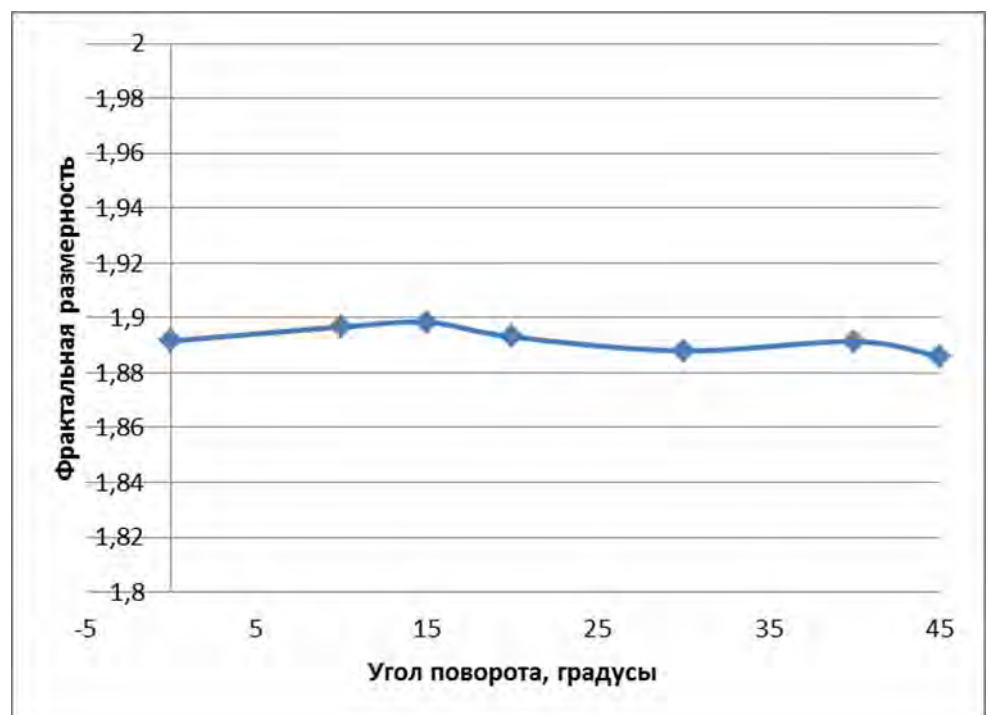

Fig. 94. Effect of orientation of Sierpinski carpet on the calculated fractal dimensionality.

Effect of orientation of Sierpinski carpet on the calculated fractal dimensionality is demonstrated in Fig. 94. As can be seen, the rotation, like other

distortions, which leave the structure of Sierpinski carpet invariant, influence the fractal dimensionality insignificantly and in a irregular manner.

Thus, the numerical experiments performed with the model subject have demonstrated the stable functioning of the program and the stability of the results, which it provides. This suggests that the results obtained by processing the real micrographs, are adequate.

Developing the algorithm for obtaining the multifractal characteristics of two-dimensional images

In spite of the success achieved with employment of the concept of regular fractals for the evaluation of fractal dimensionality of the structures typical for material science aimed at the computer analysis, there is a number of studies, which point out the insufficiency of such an approach [96]. Real material structures are essentially different from the regular fractals, and the fractal dimensionality as a numerical characteristic is not always adequate for the description of the diversity of the information contained in digital images. It may fail in qualitative description of structure nonuniformity, spatial ordering and other structural characteristics.

It can be regarded as the well established fact that the fractal dimensionality as the only fractal characteristic is insufficient for the description of self-similarity of structures of real materials. In the number of works (see, for instance, [97,98]) it has been shown that such a possibility can be provided by the multifractal formalism.

The basis of the multifractal approach for qualitative description of two-dimensional structure is the methodology for constructing the measure of set, which would approximate the structure to be examined, by putting it in Euclidian space partitioned into small square cells of equal size (equal-cell partition).

Each cell acquires some measure represented by a positive number associated with the portion of structure occupying this cell. The ratio of the number of unit structure elements, which fall into the cell, to the total number of structure elements, is accepted as the sought-for measure.

To define the measure, one can use various physical characteristics of the subject under consideration. For instance, it can be the mass of inclusions in the matrix being of interest for the researcher; in that case the total number of structure elements in the cell is associated with its mass, and the number of unit elements to be counted is given by the mass of inclusions.

However, it should be pointed out that the structures to be studied in material science are mostly represented by two-dimensional images (e.g., by micrographs obtained from the electron microscopy). In the present-day computer technology such images are represented in digital form, i.e., as the arrays of discrete equally sized image elements, the pixels. The pixel can be regarded as the smallest indivisible image element which has three numerical characteristics, namely, the coordinates specifying the position of the pixel in the two-dimensional image, and its color.

Therefore, for multifractal image analysis, it is natural to introduce the measure associated with color properties of pixels (in the simplest version, these are the two-colored pixels representing the structure under the study, along with its matrix).

Consider the general definition of a multifractal. Let there be a fractal object occupying some limited area ζ of linear size L in Euclidean space of the dimensionality d (in the case of two-dimensional image $d = 2$). Let it represent, at some stage of its construction, the set of $N \gg 1$ points distributed over this area in a certain way. We assume that $N \to \infty$.

Let us partition the overall area ζ into the square cells with the side $\varepsilon \ll L$ and the area ε^d. We will be interested in the occupied cells only, which contain at least one point of the fractal object. Let these cells be numbered as $j = \overline{1, N(\varepsilon)}$,

where $N(\varepsilon)$ is the total number of the occupied cells (which depends on the cell size ε).

Denote the number of object points in the cell with the index i as n_i.

Then, the quantity

$$p_i(\varepsilon) = \lim_{N \to \infty} \frac{n_i(\varepsilon)}{N} \qquad (86)$$

gives the probability that a randomly chosen point belonging to the constructed set is located in the cell i, i.e., it characterizes the relative population of cells. The probability normalization condition yields

$$\sum_{i=1}^{N(\varepsilon)} p_i(\varepsilon) = 1. \qquad (87)$$

The conventional method of multifractal analysis is based on the notion of *the generalized partition function* $Z(q,\varepsilon)$ where the power index can take any values within the range $-\infty < q < \infty$:

$$Z(q,\varepsilon) = \sum_{i=1}^{N(\varepsilon)} p_i^q(\varepsilon). \qquad (88)$$

The spectrum of *the generalized fractal dimensionalities (Renyi dimensinalities)*, which characterize the given distribution of points within the area ζ, is defined by the relation

$$D_q = \frac{\tau(q)}{q-1}, \qquad (89)$$

where the *scaling exponent* $\tau(q)$ is defined, in turn, as

$$\tau(q) = \lim_{\varepsilon \to 0} \frac{\ln Z(q,\varepsilon)}{\ln \varepsilon}. \qquad (90)$$

For the case that $D_q = D = const$ for all q, the set under examination is the *monofractal* described by one fractal dimensionality D. If D_q is some function of q, the set of points under consideration represents the multifractal.

By combining the above equations, one can evaluate the Renyi dimensionality as follows:

$$D_q = \frac{\tau(q)}{q-1} = \frac{\lim_{\varepsilon \to 0} \dfrac{\ln Z(q,\varepsilon)}{\ln \varepsilon}}{q-1} = \frac{1}{q-1} \lim_{\varepsilon \to 0} \frac{\ln \sum_{i=1}^{N(\varepsilon)} p_i^q(\varepsilon)}{\ln \varepsilon}. \qquad (91)$$

The uncertainty of the $0/0$ type in D_1 resulting from zero denominator $q-1$ can be resolved by using the evident relation

$$\sum_{i=1}^{N(\varepsilon)} p_i^q = \sum_{i=1}^{N(\varepsilon)} p_i e^{(q-1)\ln p_i} \qquad (92)$$

and performing the transition to the limit $q \to 1$:

$$D_1 = \lim_{\varepsilon \to 0} \frac{\sum_{i=1}^{N(\varepsilon)} p_i \ln p_i}{\ln \varepsilon}. \qquad (93)$$

Program implementation of the algorithm for obtaining the multifractal characteristics of two-dimensional images

The complex of programs, which we developed, computes the multifractal characteristics of the structures represented by the set of values of D_q for different values of q. The calculations are based on the above equations, however, as this was in the case of program implementation of the algorithm for calculation of the block fractal dimensionality, we are again limited to using the pixel as the smallest structure element. In view of this, instead of calculating the expression (91) in the limit of zero cell size, we consider the functional dependence

$$\ln \sum_{i=1}^{N(\varepsilon)} p_i^q(\varepsilon) = D_q(q-1)\ln \varepsilon + o(\varepsilon), \qquad (94)$$

and find D_q from the slope angle of the linear portion, by approximating the obtained points by the straight line, and with the use of the least square method.

This program is the development of the program elaborated earlier and its basic features are the same, as is the view of the main program window shown in Fig. 95.
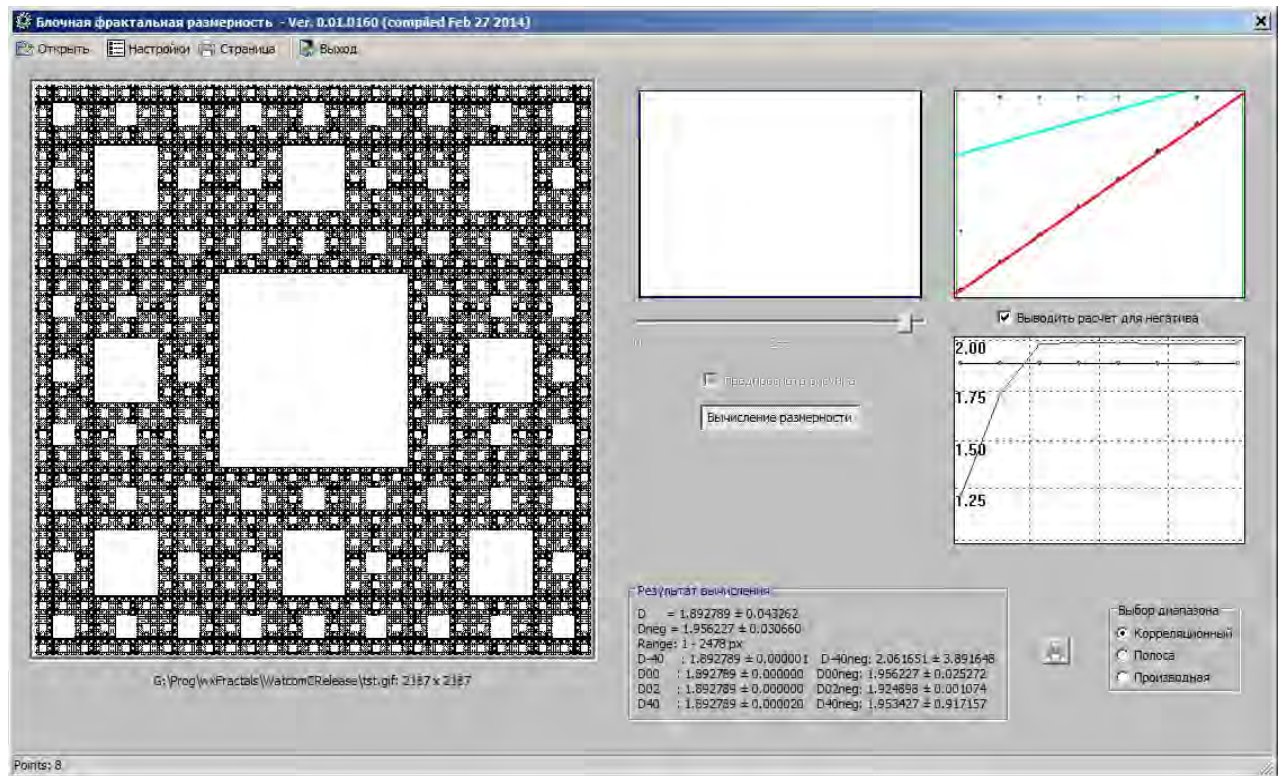
Fig.95. Overall look of the main program window.

After fixing the linear portion of the plot, the program performs the calculations and displays the fractal dimensionalities with the accuracy evaluated in accordance with the above relations.

As is seen from the screenshot given in Fig. 95, the test image (Sierpinski carpet of 2187x2187 pixel size) yields identical values for all fractal dimensionalities D_q, which are consistent with the theoretical value $D = \ln 8 / \ln 3 \approx 1.89279$, as one would expect for this monofractal.

As was shown by preliminary investigations similar to those described above, the present implementation of the algorithm is rather stable to the distortions of the test image.

The problem associated with certain sensitivity of the employed algorithm to the way of partitioning the image into the cells (actually, to the number of points) should be pointed out. This concerns, in first place, the regular fractals. For instance, in Fig. 96, the experimental points for Sierpinski carpet for 8 (top) and 20 (bottom) points of partitioning are shown, and in Fig. 97, there are given the same results for the image of real structure obtained by the electron microscopy. As is seen from the given figures, for the case of the regular fractal, the number of points considerably affects the accuracy of the evaluation of fractal characteristics due to the dispersion of experimental points, whereas in the case of real images this effect is much less pronounced.
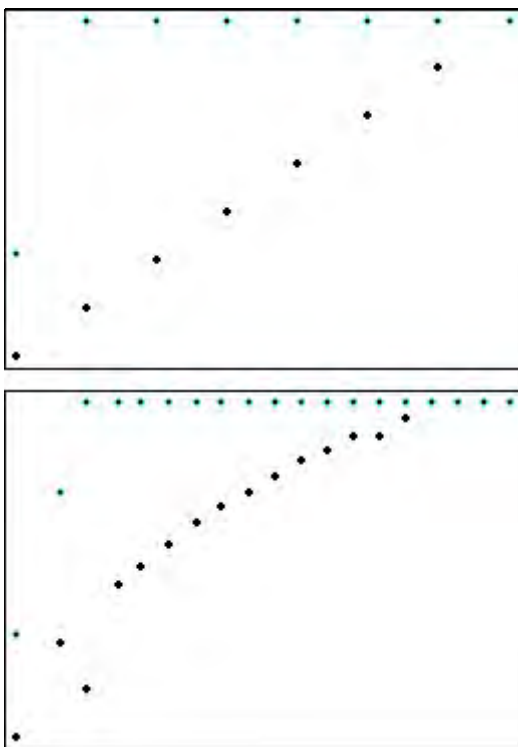

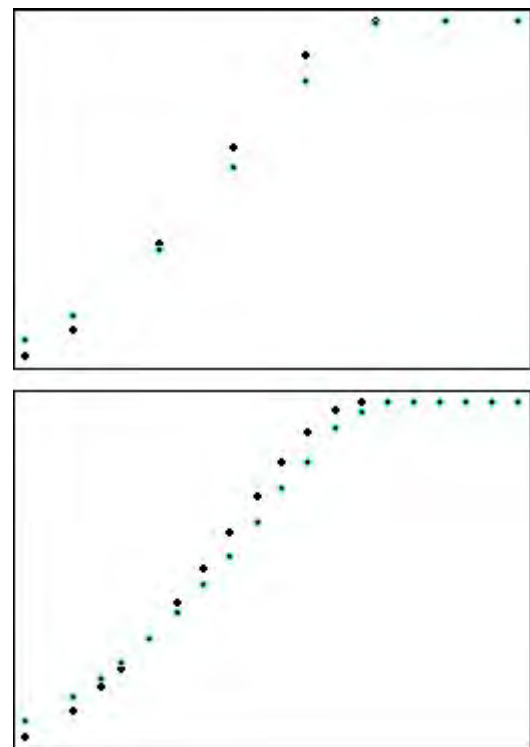Fig. 96. Experimental curves for Sierpinski carpet for 8 (top) and 20 (bottom) points.

Fig. 97. Experimental curves for the image of the real structure   for 8 (top) and 20 (bottom) points.

The matter is that in the regular fractal the ideal self-similarity manifests itself only for certain size of trial cells associated with the specific structure of the fractal itself. For example, for the above Sierpinski carpet, such ideal self-similarity is observed in the case that the trial cells are reduced in size exactly 3 times every next step. Exactly this choice of cells corresponds to the choice of 8 points for Sierpinski carpet of 2187x2187 pixel size.

For the images of real structures, the ideal self-similarity is absent. For this reason, the experimental data for different number of points used in calculations remain close to each other.

Nevertheless, one of the options of further program development should be, probably, the possibility to analyze the image size and calculate the recommended number of points in the case that this size is an exact power of some number. This would detect the possible ideal self-similarity and, and addition, solve the problem of boundary effects associated with the fact that the trial cells cannot exactly cover the image to be investigated.

Study of fractal characteristics of physical objects

The developed software was employed in the Institute for material science problems for practical investigation of images of various subjects.

In particular, the fractal analysis of the chromium films deposited under the argon on the silicon substrate, as dependent on the conditions of production, has been performed [99].

For example, in Fig. 98, there are shown four images of the surface of chromium films obtained by the deposition under argon at different ratios of partial pressures of oxygen and argon. The associated dependence of the fractal dimensionality of the image of chromium film on the ratio of partial pressures of oxygen and argon is given in Fig 99. As can be seen, there is an expressed

correlation between the fractal dimensionality of the image of the film and the conditions of its production.
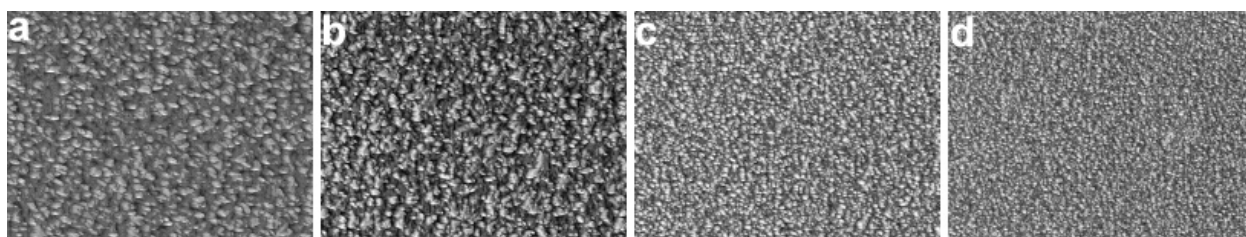
Fig. 98. Morphology of the surface of chromium films deposited at different ratios of partial pressures of oxygen and argon: 0 (a), $0.88 \cdot 10^{-2}$ (b), $2.99 \cdot 10^{-2}$ (c), $4.01 \cdot 10^{-2}$ (d)
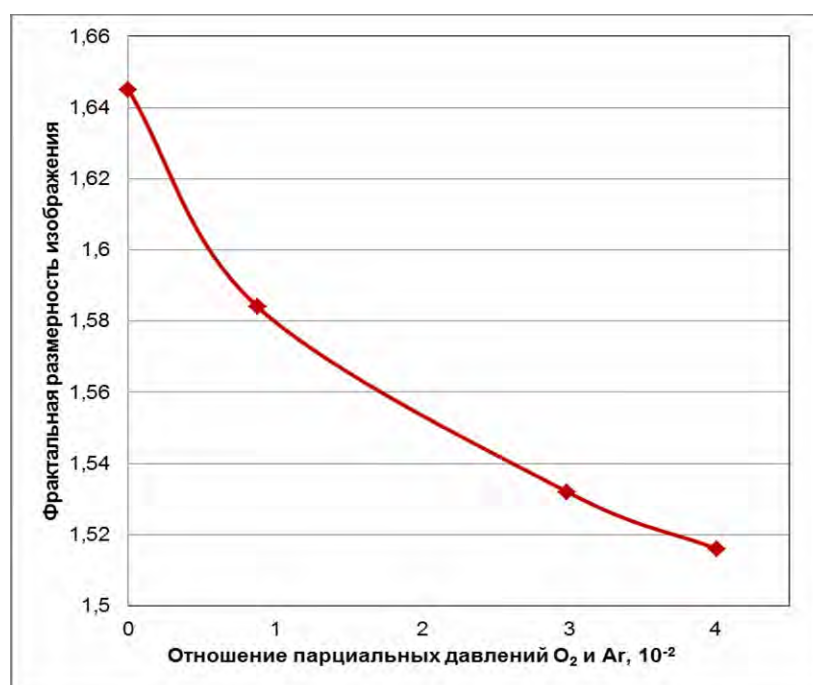
Fig. 99. Fractal dimensionality of the image of chromium film as dependent on the ratio of partial pressures of oxygen and argon during the deposition.

Four other images of the surface of chromium films obtained by the deposition under argon at different temperatures are shown in Fig. 100.
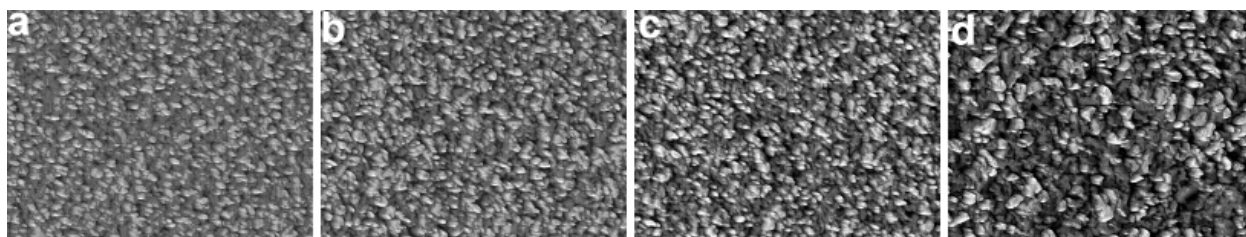
Fig. 100. Morphology of the surface of chromium film deposited at the temperature 25 (a), 230 (b), 400 (c) and 510 (d) ˚C

The results of the investigation of the fractal dimensionality and hardness of the films are given in Fig. 101.
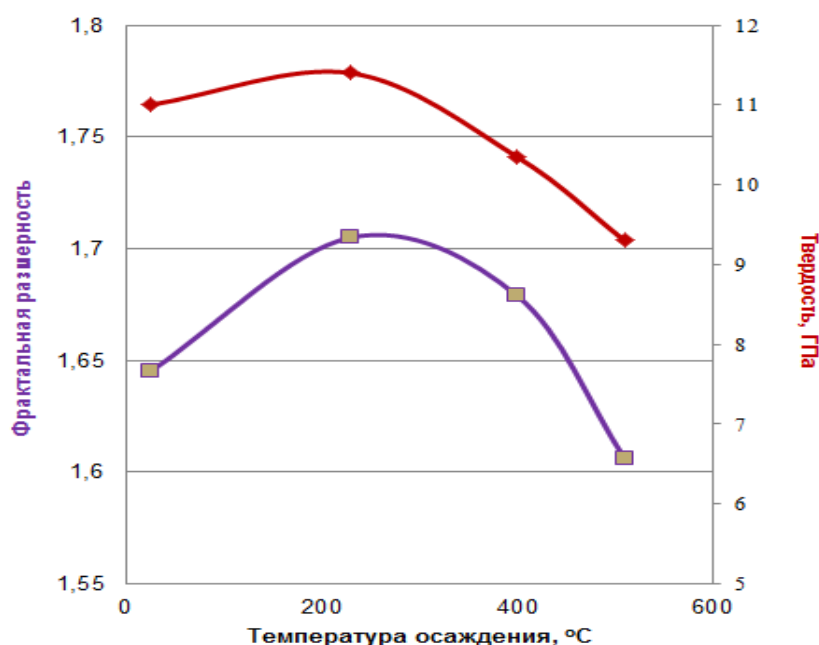
Fig. 101. Correlation between the fractal dimensionality and the hardness of the chromium films deposited at different temperatures.

As we can see, in this case the correlation between the fractal dimensionality of the obtained film and its physical property, the hardness, is observed.

Thus, the obtained results evidence that the developed software is applicable for obtaining the fractal characteristics of images of real objects, and the fractal characteristics can represent one more parameter for the description of the objects under examination.

10.Conclusion

Summarizing the results obtained we would like not only to highlight and present the main of those but point out possible further directions of their development. The first project P 273 (EOARD #068009) made a solid background of computer modeling of basic components of technological process of directed solidification of boride-boride composites in systems LaB_6-MeB_2(Me=Ti, Zr, Hf). The next project P 510 (EOARD #118003) developed a complex of mathematical models which describe this technological process and typical properties of materials-prototypes in the investigated systems and brought those to implementation in real codes. On the base of these codes, a spectrum of computative experiments (at macro-, meso-, and microscales) targeted to develop the understanding of peculiarities of eutectic composites was carried out. The results of these computative experiments are presented in the above report and they originate the following problems for further work:

I. Macroscale

-To develop the suggested conception of inner energy sources up to a level of theory, which describes the crystallization process of melts near eutectic point

- To perform complex multiscale modeling of the process of formation of «diffusion zone» for eutectic composites in refractory systems with a possibility to use this for the first time recorded and thermo-dynamically grounded formation of components, as controlling component for formation of required service properties of these composites.

II. Microscale

- to develop both the methodology of construction of interface between components of eutectic compositions and methodology of investigation of

influence of atomic parameters of interface on macro mechanical characteristics of composites.

- to develop apparatus of modeling of self-construction of atomic clusters which are components of the investigated class of composites from dimmers to nanoparticles.

III. Mesoscale

- being based upon close cooperation with other participants of the projects of «eutectic direction», to modify programs of definition of fractal characteristics of materials and construction of cellular automates up to standard software of general use by means of gaining experience while using those for different objects present in works of other participants (initial codes of computer programs are in the open public release).

11. References under the project P510

1. Zakarian D.A., Kartuzov V.V., Khhachatrian A. V. Calculation of the theoretical strength of the eutectic composites LaB_6 - MeB_2 (Me - Ti, Zr, Hf)// Works of IPMS, Mathematical modeling and numerical experiment in materials science. - Kiev: IPMS NASU. - 2011. — vol. 13. - pp. 3-8.

2. Zakarian D.A., Kartuzov V.V., Khhachatrian A. V. B. Ab initio calculation of thermal expansion coefficients of borides MeB_2 (Me - Ti, Zr), LaB_6, and eutectic composites LaB6 - MeB_2 // Powder metallurgy.- 2012.- №5/6. -pp. 65-72.

3. Baranovskaya L.V., V. V. Kartuzov. Solution of Stephan's problem by potential methods in the model of formation of fibrous composites for directional solidification. I. // Mathematical modeling and numerical experiment in materials science. - Kiev: IPMS NASU. - 2012. — vol. 14. - pp. 52-60.

4. V. L. Bekenev, V. V. Kartuzov, E. V. Kartuzov. Theoretical investigations of structure and energy of interface of LaB6-ZrB2. // The 4th International Workshop on Directionally Solidified Eutectic Ceramics, 2012.

5. Khachatrian A.V. Ab «Initio» calculation of the characteristic parameters of boride eutectic composites formation // Works of IPMS NASU, Mathematical modeling and numerical experiment in materials science. - Kiev - 2012, vol. 14.-pp. 47-51.

6. Zakarian D.A. Investigation of quasi-binary eutectic composites in a liquid - solid from first principles// NANU reports. 2012. №6.-pp. 95-100.

7. Zakarian D., Kartuzov E., Khachatrian A. AB - initio calculation of mechanical characteristics LaB_6 and MeB_2 (Me - Ti, Zr, Hf) // Directionally solidified 4,

Eutectic ceramics, 15-17 October 2012; - abstracts. - Washington, USA-2012. - P. 24.

8. V. V. Kartuzov, A. V. Bystrenko Computer modeling of contact melting of binary eutectic on the base of phase filed theory; XIV International Scientific Kravchuk Conference, 19-20 April, 2012, Kyiv.

9. V. V. Kartuzov, A. V. Bystrenko. Modeling of contact melting in binary eutectics, on the base of phase field theory, // 4th International Workshop on Directionally Solidified Eutectic Ceramics, Washington D.C., U.S.A. 14-17, October 2012.

10. V. N. Paderno, V. V. Kartuzov, V. B. Filipov, B. A. Galanov, E. A. Efimova Peculiarities of formation of eutectic structure LaB6-ZrB2 at low crystallization rates 4th International Workshop on Directionally Solidified Eutectic Ceramics, Washington D.C., U.S.A. 14-17, October 2012.

11. V. L. Bekenev, V. V. Kartuzov, E. V. Kartuzov. Theoretical investigations of structure and energy of interface of LaB6-ZrB2, 4th International Workshop on Directionally Solidified Eutectic Ceramics, Washington D.C., U.S.A. 14-17, October 2012.

12. Kartuzov V.V., Bystrenko O.V., Phase-field simulations of eutectic melting. International Conference PROBLEMS OF THEORETICAL PHYSICS October 8-11, 2012, Kyiv, Ukraine, Conference proceedings, p.70.

13. Kartuzov V.V., Baranovskaya L.V. Solution of Stephan's problem by potential method in the model of formation of fibrous composites; XIV International Scientific Kravchuk Conference, 19-20 April, 2012, Kyiv

14. Kartuzov V.V., Baranovskaya L.V. Solution of Stephan's problem by potential method in the model of formation of fibrous composites // XIV International

Scientific Kravchuk Conference, April 19-20, 2012, Kiev: Proceeding. T. 1. Differential and integral equations and their application. - Kiev : "КПІ", 2012. - pp. 211-214.

15. Baranovskaya L.V. Modification of the Method of Resolving Functions for Difference-Differential Pursuit's Games // Scientific news "KPI". - 2012. - № 4. - pp. 14-20.

16. Baranovskaya L.V. Development of methods for numerical solution of functional-differential equations // Herald of Kiev National University named after Taras Shevchenko: proceeding of XVI International Conference "Dynamical system modelling and stability investigation", May 29-31 2013. - Kiev, 2013. - pp. 69

17. Kartuzov V.V., A.A.Priadko Formation of field of cellular automates for modelling of the process of deposition of impact resistant coatings on titanium substrate // Mathematical modeling and numerical experiment in materials science. — Kiev: IPMS NASU, 2013, vol. 15, pp.113-119.

18. V.V Ogorodnikov, O.N. Grigoriev, V.L. Bekenev, Kartuzov V.V. Interatomic potentials of interaction for especially refractory compounds // Mathematical modeling and numerical experiment in materials science. — Kiev.: IPMS NASU, 2013, vol. 15, pp. 86-97.

19. Zakarian D.A., Kartuzov V.V., Khachatrian A.V. Determination of the characteristic parameters of the eutectic in the system of LaB_6 –$Me^{IV - VI} B_2$ by the temperatures of components fusion // 4-international conference. «HighMatTech», October 7-11 2013:. – Kiev.: - 2013. - A- 334.

20. Zakarian D., Kartuzov E., Khachatrian A. Ab initio investigation of the dependence of the strength on deformation in refractory eutectic

nanocomposites LaB6 -MeB2(Me-Ti, Zr,Hf) // The 19th Internat. Confer. On composite materials -Kanada-2013/ abstract -2p.

21. Zakarian D.A., Khachatrian A.V. Modelling of intermolecular interactions in the system LaB_6 - MeB_2in the framework of the pseudo-potential method // NANU reports. - 2013. - №1. - pp. 77-82.

22. V. L. Bekenev, V. V. Kartuzov. Computer engineering of the interface in the nanocomposite LaB_6-$Zr(Ti)B_2$// Mathematical modeling and numerical experiment in materials science. — Kiev.: IPMS NASU. - 2013. — vol. 15. — pp. 30-35.

23. I.E.Krasikova, V.V.Kartuzov, I.V.Krasikov. Characteristics of the computer implementation of the algorithm for two-dimensional images fractal dimension calculating // Mathematical models and numerical experiment in materials science, vol. 15, Kiev, 2013, pp.69 - 73.

24. Zakarian D.A., Kartuzov V.V., Khhachatrian A. V. The strength characteristics of the materials in the system LaB_6 - MeB_2 (Me – Ti, Zr, Hf)// Mathematical models and numerical experiment in materials science. - 2013. - vol. 15. - pp. 46-49.

25. V.Kartuzov, O.Bystrenko, I.Motienko. Simulation of structure formation in the process of directional crystallization of LaB_6- ZrB_2// Mathematical models and numerical experiment in materials science. - Kiev.:IPMS NASU. - 2014. - vol. 16. - C. 69.

26. V.Kartuzov, O. Bystrenko Phase-Field Modelling of Contact Melting in Binary Alloys http://arxiv.org/pdf/1301.1081v2.pdf (2014)

27. O.Bystrenko, V. Kartuzov Contact melting and the structure of binary eutectic near the eutectic point J. Alloys and Compounds, 617, (2014), Pages 124-128 http://arxiv.org/pdf/1404.3379v2.pdf

28. V.V. Kartuzov, A.N. Machulenko, E.A. Efimova.. Simulation modelling of the formation of eutectic structures based on cellular automata method.// Mathematical models and numerical experiment in materials science. - Kiev.: IPMS NASU. - 2014. -vol. 16. – pp. 120-132.

29. Krassikova I.E., Kartuzov V.V., Krasikov I.V. The program implementation of the algorithm for two-dimensional image processing to calculate multifractal characteristics // Mathematical models and numerical experiment in materials science, vol. 16, Kiev, 2014.

30. Zakarian D.A., Kartuzov V.V., Khachatrian A.V. The theoretical strength of quasi-binary eutectic composites LaB6 - MeB2 considering the influence of inter-component communication in the interface EMRS -204, 14-19.09. Warsaw.

31. Zakarian D.A., Kartuzov V.V., Khachatrian A.V. Calculation of the energy of components interface in quasi boride eutectic systems// the 4th World Congress on Engineering and Technology (CET 2014) which will be held on October 26-28, 2014 in Wuhan China/ abstract –1p.

32. Zakarian D.A., Khachatrian A.V. Modeling of the theoretical strength's dependence of the strain and temperature in the quasi-binary eutectic systems LaB_6 - MeB_2 from "first principles" //55 International conference «Actual problems of strength ».- June 9-13, 2014.: - Kharkov, pp. -116.

33. Zakarian D.A., Khachatrian A.V. AB Initio researching of boride-boride composite materials // International conference on powder metallurgy.- 22 - 25.04.*2014* PM-*2014*: Kiev. :-5. 312.

34. Kartuzov V.V., Bystrenko O.V. Modelling of kinetics of contact melting in eutectic systems // International Conference on Sintering 2014, 24-28 August, Germany, P.275

35. Kartuzov V.V., Bystrenko O.V Simulations of structure formation in boride-boride composites // Powder Metallurgy. Frantsevich Institute for Problems of Materials Science of NASU (in press).

36. Zakarian D.A. Mechanical characteristics of quasi binary eutectic composites with the influence of inter-component communication at the interface // NANU reports -2014, in print

37. Zakarian D.A., Kartuzov V.V., Khachatrian A.V. Empirical formulas for determining the characteristic parameters in quasi-metal eutectic systems // NANU reports-2014, in print

38. Zakarian D.A. Calculation of the surface energy of the component's contact in quasi eutectic systems // NANU reports -2014, in print

39. Zakarian D.A., Kartuzov V.V., Khachatrian A. V. The theoretical strength of borides and quasi-boride eutectic systems at high temperatures (Powder Metallurgy. -2014, in print)

References

1   Paderno Yu.B., Paderno V.N., Fillipov V.B. Directionally solidified ceramic fiber-reinforced boride composites. Ogneupory i tekhnicheskaya keramika, 2000, Vol. 11, p. 7-12 (in Russian).

2   Ordanian S.S., Paderno Yu.B., Khoroshilova I.K., Nikolaeva E.E. Interaction in system LaB6 – CrB2. Powder Metallurgy, 1984, Vol. 5, p. 64-66 (in Russian).

3   Ordanian S.S., Paderno Yu.B., Khoroshilova I.K., Nikolaeva E.E. Interaction in system LaB6 – HfB2. Powder Metallurgy, 1984, Vol. 2, p. 79-81 (in Russian).

4   Tiller W.A. Liquid Metals and Solidification. Cleveland: ASM, 1958.

5   Chalmers B. Principles of Solidification. New York-London-Sydney: John Wiley & Sons Inc, 1964.

6   Deng H., Dickey E.C., Paderno Y. et al. Crystallographic characterisation and indentation mechanical properties of LaB6-ZrB2 directionally solidified eutectics. Journal of materials science, 2004, Vol. 39, p. 5987-5994.

7   Paderno Yu., Paderno V., Filippov V. Some peculiarities of structure formation in eutectic d- and f-transition metals boride alloys. Boron-rich solids, AIF Conference proceedings N 231, Albuquerque, NM, 1990, p. 561-569.

8   Paderno Yu., Paderno V., Filippov V. Crystal Chemistry of Eutectic Growth of d- and f-Transition Metals Boride. JJAP Series, Japan Sci. Soc., Tokyo, 1994, Vol. 10, p. 190-193.

9   Samarskii A.A., Moiseenko B.D. Economic scheme of the end-to-end method for the multidimensional Stefan problem, J. of Numer. Math. and Math. Physics, 1965. Vol. 5, No. 5, p. 816-827.

10   Louchev O.A., Otani S. Marangoni convection and enhanced morphological stability in floating zone traveling solvent crystal growth of LaB6. J. Appl. Phys., 1996. Vol. 80, p. 6567.

11   Wu J., Choi J., Zhang S., Hilmas G. A Process Model for Laser Surface Treatment of Plasma Sprayed Coatings. Proc. IMECE04. ASME 2004 International Mechanical Engineering Congress and Exposition. Anaheim, California, USA, November 13 – 19, 2004, pp. 447-455.

12   Bokhonov B., Korchagin M. In-situ investigation of the formation of eutectic alloys in the systems silicon-silver and silicon-copper. J.Alloys and Compounds, 2002. Vol. 335, p. 149-156.

13   V.M. Zalkin, Nature of Eutectic Alloys and Effect of Contact Melting, Metallurgiya, Moscow, 1987.

14   A.I. Somov, M.A. Tikhonovskii, Eutectic Compositions, Metallurgiya, Moscow, 1975.

15   Yu. B. Paderno, V. N. Paderno, V. B. Filippov, Yu. V. Mil'man, A. N. Martynenko. Sov. Powder Metallurgy and Metal Ceramics 31, (Issue 8), (1992), 700.

16   W.J. Boettinger, J.A. Warren, C. Beckermann, A. Karma, Annu. Rev. Mater. Res. 32 (2002), 163.

17   I. Singer-Loginova, H.M. Singer, Rep. Prog. Phys. 71 (2008), 106501.

18   A.A. Wheeler, G.B. Mc Fadden, W.J. Boettinger, Proc. R. Soc. Lond. 452 (1996) 495.

19   B. Bokhonov, M. Korchagin, J. of Alloys and Compounds 335 (2002), 149.

20   B. Bokhonov, M. Korchagin, J. of Alloys and Compounds 312 (2000), 238.

21   Automated Solution of Differential Equations by the Finite Element Method, The FEniCS Book, Eds. A. Logg, K.-A. Mardal, G. N. Wells, Springer-Verlag, Berlin, 2012; http://fenicsproject.org.

22   R.W. Olesinski, G.W. Abbaschian, Bulletin of Alloy Phase Diagrams 7 (1986) 170.

23   Tables of Physical Quantities, the Handbook (in Russian), Ed. I.K.Kikoin, Atomizdat, Moscow, 1976.

24   J. Tang, X. Xue, J. Mater. Sci 44 (2009) 745.

25   F. Drolet, K.R. Elder, M. Grant, J.M. Kosterlitz, Phys.Rev.E 61 (2000), 6705.

26   L. Granasy, G. Tegze, G. I. Toth, Tamas Pusztai, Phil. Magazine 91 (2011), 123.

27   M. Plapp, Phil. Magazine 91 (2011), 25.

28   M. Apel, B. Boettger, H.J. Diepers, I.J. Steinbach,. of Crystal Growth 154 (2002), 237–239.

29   B. Nestler, A.A. Wheeler, Computer Physics Communications, 147 (2002), 230.

30   Ordanian S.S Prospetives for creating novel ceramics for engineering // Chemical Journal of Armenia.- 2009. - 62, №5. – P.547-556 (in Russian).

31   Hua Chen. High-temperature strength of directionally reinforced LaB6-TiB2 composite/ Chun Hua Chen, Yi Xuan, Shigeki Otani // Journal of Alloys and Compounds. – 2003.-Volume: 350, Issue: 1-2, ISSN:09258388.- DOI:10.1016/S0925-8388(02)00988-X.

32   Bogomol V. High-temperature strength of directionally reinforced LaB 6-TiB2 composite / Bogomol V., Nishimura T., Vasylkiv O., Sakka Y., Loboda P. // Journal of Alloys and Compounds.-2010.-Volume: 505, Issue: 1, Pages:

130-134.-ISSN:09258388.-ISBN:0925-8388.-
DOI:10.1016/j.jallcom.2010.05.003

33 Zakaryan D., Kartuzov V., Kartuzov E., Khhachatrian A., and Sayir A. Calculation of composition in LaB6 - TiB2, LaB6 - ZrB2 eutectics by means of pseudopotential method" Journal of the European Ceramic Society.-2011.-V.31.- №7 –P. 1305-1308.

34 Zakaryan D.A. A priori model pseudopotential in the theory of cubic crystals // Abstract of PhD thesis. Kiev.- 1987. P.-19 (in Russian).

35 Zakaryan D.A, Khhachatrian A.V. Simulation of the molecular interaction in the system LaB6 - MeB2 based on the pseudopotential approach // NASU Reports. - 2013. - №1. - P. 77-82 (in Russian).

36 Zakaryan D.A, Kartuzov V.V., Khhachatrian A.V. Calculation of the typical parameters of LaB6 - MeB2 alloys based on the pseudopotential method // Proceedings of IPMS NANU. Series "Simulation in material science", " Mathematical models and computing experiment in Material Science ". Kiev - 2008. – Issue 10. P. 21 - 27 (in Russian).

37 Zakaryan D.A, Kartuzov V.V., Khhachatrian A.V. Calculation of the theoretical strength in LaB6 - MeB2 (Me - Ti, Zr, Hf) compounds of eutectic composition // Proceedings of IPMS NANU. Series "Simulation in material science", " Mathematical models and computing experiment in Material Science ". Kiev -2011. – Issue 13. P. 3 – 8 (in Russian).

38 Khhachatrian A.V. Ab initio calculation of mechamical properties of LaB6 and MeB2 (Me – Ti, Zr, Hf) // Proceedings of IPMS NANU. Series "Simulation in material science", " Mathematical models and computing experiment in Material Science ". Kiev –2012, Issue. 14. – P. 47-51 (in Russian).

39   Zakaryan D.A, Kartuzov V.V., Khhachatrian A.V. Strength characteristics of materials in the system LaB6 - MeB2 (Me – Ti, Zr, Hf) // Proc. of IPMS NANU. Series "Simulation in material science", " Mathematical models and computing experiment in Material Science ". Kiev – 2013. – Issue 15. – P. 46 (in Russian).

40   Zakaryan D.A, Kartuzov V.V., Khhachatrian A.V. Strength characteristics of materials in the system LaB6 - MeB2 (Me – Ti, Zr, Hf) // Proc. of IPMS NANU. Series "Simulation in material science", " Mathematical models and computing experiment in Material Science ". Kiev – 2013. – Issue 15. – P. 46 (in Russian).

41   Zakaryan D.A, Kartuzov V.V., Khhachatrian A.V.   Ab initio calculation of the coefficients of thermal expansion of the borides MeB2   (Me – Ti, Zr) and eutectic composites LaB6 –   MeB2.// Powder Metallurgy.- 2012.- №5/6. –P. 65-72 (in Russian).

42   Zakaryan D.A, Kartuzov V.V., Khhachatrian A.V. Theoretical strength of borides and quasi-binary boride eutectic systems at high temperatures (Powder Metallurgy -2014, in press) (in Russian).

43   Zakaryan D.A Calculation of the surface energy of the component contact in quasi-binary eutectic systems // NASU Reports. - 2014. - №11. - P. 82-87 (in Russian).

44   Zakaryan D.A Mechanical properties of quasi-binary eutectic composites with account of the effects of inter-component interaction at the interface // NASU Reports - 2014. - №12. (in press) (in Russian).

45   Zakaryan D.A, Kartuzov V.V., Khhachatrian A.V.Calculation   of   the theoretical   strength   in LaB6 - MeB2 (Me - Ti, Zr, Hf) compounds of eutectic composition // Proceedings of IPMS NANU. Series "Simulation in material   science", " Mathematical models and computing experiment in Material Science ". Kiev -2011. – Issue 13. P. 3 – 8 (in Russian).

46   Kurts V.V., Zam P.R. Directional Crystallization of eutectic materials. - M. : Metallurgiya. 1980. - 271 p (in Russian).

47   Serebryakova T.I., Neronov V.A., Peshev P.D. High-temperature borides. M., Metallurgiya, 1991, 367 p (in Russian).

48   Kittel C. Introduction to the solid state physics. – M. Nauka, 1978. – c. 790 (in Russian).

49   Zhai Zhang-Yin, Peng Ju, Zuo Fen, Ma Chun-Lin, Cheng Ju, Chen Gui-Ben, Chen Dong "Pressure and temperature effects on NaCl - type transition metal carbide from first- principles calculation" // Physica   B doi:10.1016/j.physb.2010.08.047.

50   Heine V., Cohen M. L., and Weaire D. Pseudopotential theory. – M.: Mir, 1973. – p. 557 (in Russian).

51   Belan-Gaiko L.V., Bogdanov V. I., Fuks D.L. Calculation of elastic and thermal properties of alkali metals based on the pseudopotential approach // Izvestiya Vuzov. 1979. -№ 2. –p. 25-38 (in Russian).

52   A.I. Somov, M.A. Tikhonovskii, Eutectic Compositions, Metallurgiya, Moscow, 1975 (in Russian).

53   Rondy David, Cohen Marvin L. Ideal strength of diamond, SiC and Ge //Physical review B. 2001. – 64, № 21 – P. 212103/1-212103/3.

54   Raju G. B., Basu B., Tak N. H., Cho S. J. Temperature dependent hardness and strength properties of TiB2 with TiSi2 sinter-aid // Journal of the European Ceramic Society.-2009.- Volume: 29, Issue: 10, Pages: 2119-2128.-ISSN:09552219.- DOI:10.1016/j.jeurceramsoc.2008.11.018

55   Panda K. B., Ravi Chandran K. S. Thermoelastic properties of ScB2, TiB2, YB4 and HoB4.Experimental and theoretical studies // Acta Materialia.- 2011. -Volume: 59, Issue: 12, Pages: 4886-4894.-ISSN:13596454.-ISBN:1359-6454.- DOI:10.1016/j.actamat.2011.04.030

56   Panda K. B., Ravi Chandran K. S. Determination of elastic constants of titanium diboride (TiB2) from first principles using FLAPW implementation of the density functional theory //Computational Materials Science. – 2006.- Volume: 35, Issue: 2, Pages: 134-150.- ISSN:09270256.- DOI:10.1016/j.commatsci.2005.03.012

57   Zakaryan D.A, Kartuzov V.V., Khhachatrian A.V. Calculation of the thermodynamical potentials for the systems B4C – TiB2 , TiB2 - SiC,   B4C - SiC based on the pseudopotential method // Powder Metallurgy, 2009. - № 9-10 . –p.124-132 (in Russian).

58   Zakaryan D.A, Kartuzov V.V., Makar V.A., Khhachatrian A.V. Computer simulation of the conditions for eutectic formation in the system Hf – HfB // NASU Reports. 2010. № 10.- p. 95-100 (in Russian).

59   Kakhramanov K, S., Didyk V. V., Study of the nature of the interface interaction in the eutectic // Metallofizika T.3, 1981, 31-39 (in Russian).

60   Dutchak Ya. I., Kavich I. V., Shevchuk P. I. X-ray spectral study of the electron structure of selected simple eutectic alloys // Ukr. J. Phys. - 1977. -v.-22, №5.- p.822-826 (in Russian).

61   V.M. Zalkin, Nature of Eutectic Alloys and Effect of Contact Melting, Metallurgiya, Moscow, 1980.- 146p (in Russian).

62   Wang S.Q., Ye H.Q. Theoretical studies of solid – solid interfaces // Current Opinion in Solid State. Materials Science.- 2006.- № 10. –P. 26-32.

63   Arya A, Carter EA. Structure, bonding, and adhesion at the ZrC(100)/ Fe(110) interface from first principles.// Surf Sci.-2004.-560; 103-20.

64   Wang XG, Smith JR. Si/Cu interface structure and adhesion.//Phys. Rev. Lett. – 2005; 95: 156102.

65   Paderno V. N., Paderno Yu. B., Martynenko A. N., Filippov V. B. Structural aspect of the formation of viscous fiber boride-based ceramics //

Elektronnaya mikroskopiya i prochnost' materialov.- 1995. - P. 95-112 (in Russian).

66   S.Q. Wang, H.Q. Ye. Current Opinion in Solid State and Materials Science 10 (2006) 26–32.

67   P. Giannozzi et al., http://www.quantum-espresso.org.

68   C.H.Booth, J.L. Sarrao, M.F.Hundley et al. Phys. Rev., B63, 224302 (2001).

69   V.A.Gasparov, N.S.Sidorov, I.I.Zver'kova and M.P.Kulakov. JETP Lett., 73,532 (2001).

70   G.V. Samsonov. Element properties. Part 1 — M.: Metallurgiya, 1976. — 600 p. (in Russian).

71   I. Jouanny, M. Sennour, M.H. Berger, V.B. Filipov, A. Ievdokymova,V.N. Paderno,   A. Sayir. Effect of Zr substitution by Ti on growth direction and interface structure of LaB6–TixZr1–xB2 directionally solidified eutectics // Journal of the European Ceramic Society 34 (2014) 2101–2109.

72   Guo B. C., Kerns K. P., Castleman A. W. Ti8C12+-metallo-carbohedrenes: A new class of molecular clusters //Science. – 1992. – 255. – P. 1411 – 1413.

73   Dasog M., Scott R. W. J. Understanding the oxidative stability of gold monolayer-protected clusters in the presence of halide ions under ambient conditions // Langmuir. - 2007. – 23, No. 6. – P. 3381 – 3387.

74   Pilgrim J. S., Duncan M. A. Beyond metallo-carbohedrenes: Growth and decomposition of metal-carbon nanocrystals // Journal of the American Chemical Society. – 1993. – 115. – P. 9724.

75   Helden G., Heijnsbergen D., Meijer G. Resonant Ionization Using IR Light: A New Tool To Study the Spectroscopy and Dynamics of Gas-Phase Molecules and Clusters // J. Phys. Chem. – 2003. – A107, No. 11. – P. 1671 – 1688.

76   Zhang Q., Lewis S.P. Weak bonding of carbon atoms at corner sites in titanium-carbide nanocrystals // Chem. Phys. Letters. – 2003. – 372. – P. 836 – 841.

77   Sau T. K., Pal A., Pal T. Size regime dependent catalysis by gold nanoparticles for the reduction of eosin // Journal of Physical Chemistry. – 2001. – A105, No. 38. – P. 9266-9272.

78   Ilyushin G.D. Simulation of the processes of self-organization in crystal-forming systems // M.: Editorial URSS, 2003. – 376 p. (in Russian).

79   Frisch M.J., Trucks G.W., Schlegel H.B., et al. Gaussian 03 // Gaussian, Inc., Pittsburgh PA, 2003.

80   Foresman J. B., Frisch E. Exploring Chemistry with Electronic Structure Methods // Gaussian, Inc, Pittsburgh PA, 1996 – 303 p.

81   Loboda P.I., Pecularities of structure formation of directianally solidified eutectic alloys in LaB6–MeB2 systems // Prozessy Litya. –2002.– №1. – P. 83 – 89 (in Russian).

82   J. von Neumann Theory of self-reproducing automata. M.: «Mir», 1971. (in Russian). Toffoli T., Margolus N. Cellular automata machines. - M.: Mir, 1991. - 280 p (in Russian).

83   A. A. BURBELKO, W. KAPTURKIEWICZ, D. GURGUL. Analysis of causes and means to reduce artificial anisotropy in cellular automaton modelling of the solidification process // W: SP07 : Solidification Processing 2007 : proceedings of the 5th decennial international conference : 23–25 July 2007 / ed. Howard Jones. — Great Britain : University of Sheffield. Department of Engineering Materials, 2007. — ISBN-10: 0-9522507-4-8; ISBN-13: 978-0-9522507-4-6. — S. 31–35. — Bibliogr. s. 35, Abstr).

84   Paderno Yu.B., Paderno V.N., Fillipov V.B. Directionally solidified ceramic fiber-reinforced boride composites. Ogneupory i tekhnicheskaya keramika, 2000, Vol. 11, p. 7-12 (in Russian).

85   Vstovsky G. V. Elements of informational physics. M.: MGIU, 2002. — 260 p. (in Russian).

86   Ivanova V.S., Vstovsky G.V., Kolmakov A.G., Pimenov V. N. Multifractal method for testing the structure stability in materials. — M.: Interkontakt Nauka, 2000, 54 p. (in Russian).

87   Feder J. Fractals. New York: Plenum Press, 1988. (Available in Russian: M.: Mir, 1991.)

88   I. E. Krasikova, I. V. Krasikov, V.V. Kartuzov. Determining the fractal characteristics of material structure by means of multifractal image analysis. Numerical experiment with model objects. — Proceedings of IPMS NANU. Series "Simulation in material science", " Mathematical models and computing experiment in Material Science ". -Kiev, 2007, Issue 9, p. 79–84 (in Russian).

89   Vstovsky G.V., Kolmakov A.G., Terentiev V. F. Izvestiya RAN, series Metally, 1993, №4, p.164–178 (in Russian).

90   Jaffard S. Multifractal Formalism for Functions. — Philadelphia: SIAM, 1997.

91   B.B. Mandelbrot. Fractals: Form, Chance, and Dimension. Freeman, San Francisco, 1977.

92   B.B. Mandelbrot. The Fractal Geometry of Nature. Freeman, San Francisco, 1982.

93   V. I. Roldugin. Fractal structures in disperse systems. — Uspekhi Khimii 72 (10) 2003, p. 931–959 (in Russian).

94   B. K. Barakhtin, N. V. Lebedeva, U. A. Pazilova. Digital processing and multifractal analysis of diffraction images of structures. — Deformatsiya i razrusheniye materialov, №9, 2006. — p. 18–23 (in Russian).

95   T. Kormen, Ch. Leizerson, P. Rivest, K.Shtain. Algorithms: development and analysis. — M.: "Vilyiams", 2005 г. — 1296 p. (in Russian).

96   I. E. Krasikova, V. V. Kartuzov, I. V. Krasikov. Computer implementation of the algorithm for calculation of fractal dimensionality of the material structure of the images obtained by means of electron microscopy. // Proceedings of IPMS NANU. Series "Simulation in material science", " Mathematical models and computing experiment in Material Science ". -Kiev — 2011. — Issue 13. — P.82–89 (in Russian).

97   G. V. Vstovsky, A.G. Kolmakov, I. J. Bunin. Introduction to multifractal parametrization of material structure. (Izhevsk: RC «Regular and Chaotic dynamics », 2001) 116 (in Russian).

98   M.Giona, P. Piccirili. Multifractal analysis of chaotic power spectra. J.Phys.A, 24, 367-373 (1991).

99   Firstov S. A., Kulikovsky V. Yu., Rogul' T. G., Dub S. N., Ponomarev S. S., Timofeeva I. I., Shut O. A. Mechanical properties of nanocrystal chromium films alloyed with small amount of oxygen. — Nanostrukturnoye materialovedeniye. — № 4, 2011. — P.31–41 (in Russian).